8-1-2010

Toward a damage-based finite element fracture theory and application to ductile metals

Thomas Neil Williams

TOWARD A DAMAGE-BASED FINITE ELEMENT FRACTURE THEORY AND APPLICATION TO DUCTILE METALS

By

Thomas Neil Williams

A Dissertation
Submitted to the Faculty of
Mississippi State University
in Partial Fulfillment of the Requirements
for the Degree of Doctor of Philosophy
in Computational Engineering
in the Department of Computational Engineering

Mississippi State, Mississippi

August 2010

TOWARD A DAMAGE-BASED FINITE ELEMENT FRACTURE THEORY AND APPLICATION TO DUCTILE METALS

By

Thomas Neil Williams

Approved:

_____ Philip M. Gullett Assistant Professor of Civil and Environmental Engineering (Director of Dissertation)	_____ Douglas J. Bammann Professor of Mechanical Engineering (Committee Member)
_____ Ioana Banicescu Professor of Computer Science and Engineering (Committee Member)	_____ James C. Newman, Jr. Professor of Aerospace Engineering (Committee Member)
_____ Seth F. Oppenheimer Professor of Mathematics (Minor Committee Member)	_____ Mark M. Rashid Adjunct Professor of Civil and Environmental Engineering (Committee Member)
_____ J. Mark Janus Professor of Aerospace Engineering Director of Graduate Studies in Computational Engineering	_____ Sarah A. Rajala Dean of the Bagley College of Engineering

Name: Thomas Neil Williams

Date of Degree: August 07, 2010

Institution: Mississippi State University

Major Field: Computational Engineering

Major Professor: Dr. Philip M. Gullett

Minor Field: Mathematics

Minor Professor: Dr. Seth F. Oppenheimer

Title of Study: TOWARD A DAMAGE-BASED FINITE ELEMENT FRACTURE THEORY AND APPLICATION TO DUCTILE METALS

Pages in Study: 174

Candidate for Degree of Doctor of Philosophy

In this work, the simulation of monotonic fracture in ductile metals was studied and a method of predicting damage-based fracture propagation was introduced. Traditional methodologies for predicting stable crack growth were investigated, and an error analysis was performed to show the suitability of the fracture simulation method chosen for this study. J_2 plasticity was investigated for its applicability in predicting crack advance direction for mode-I and mixed-mode simulations. A two parameter crack advance criterion was introduced, and crack propagation simulations were performed to show the suitability of the new fracture criterion that is dependent on damage. J_2 plasticity was modified in an attempt to capture the damage mechanisms occurring in front of the crack tip. The end result of this research is a computational tool that is capable of predicting the crack propagation path based on physical and measurable

material parameters without knowledge of the crack trajectory a priori while also allowing the constitutive model for the material response to be readily changed.

An error analysis was also performed on the existing equations of crack surface displacements for symmetric cracks emanating from a circular hole in an infinite plate subjected to remote stress and stress applied to a segment of the crack surface. New equations were developed for crack surface displacements for symmetric cracks emanating from the circular hole in an infinite plate subjected to a remote stress.

DEDICATION

I would like to dedicate this research to my late grandfathers, Marvin Williams and Truman Williams, who encouraged me to continually learn and better myself and showed me what unending love truly means.

ACKNOWLEDGEMENTS

I would like to thank all of the people who without them this work would not have come to fruition. I would like to thank Dr. Philip M. Gullett for being my advisor, financially supporting this work, and giving me the freedom to explore the areas of research that I found interesting. Expressed appreciation is due to CAVS and NASA for supplemental financial support. Special thanks must go to Dr. Ioana Banicescu and Dr. Seth Oppenheimer for serving on my committee and for their input on the work presented here. I would like to thank Dr. Douglas Bammann, who provided a solid foundation in continuum mechanics, for always being there to provide help, and for supporting this research by being on my committee. I would like to thank Dr. Mark Rashid on whose work I have based this research and for being an endless resource of valuable knowledge and encouragement. I would like to thank Dr. J.C. Newman, Jr. for his advice and guidance with my dissertation and allowing me to work with him in other research areas. I would like to thank Dr. Mark Horstemeyer for encouraging me years ago to work towards a Ph.D. Thank you to my friends Justin, Matthew, Brian, Wes, Paul, Don, Jean-Luc, Clemence, Youssef, Kiran, Bohumir, Jeff, Florina, Haley, David Oglesby, David Francis, Jesse, Sebastien, Andy, Mohammad, and Ali, to name a few whose conversations helped my research, kept everything in perspective, and managed to keep me smiling. I also need to thank the office staff, Rosemary and Kendra, who have been a big help over the years. I could not have done any of this without the support and

encouragement from my beautiful wife, Leigh, who patiently endured this process in the best way. I also want to thank the rest of our family who stood by us during these years. E Pluribus Unum. Dei gratia.

TABLE OF CONTENTS

LIST OF TABLES

TABLE

LIST OF FIGURES

FIGURE

CHAPTER I

INTRODUCTION

Ductile metals are used in various industrial applications where failure would be considered catastrophic. Attempts to model failure in terms of stable crack growth accurately have been made, and currently the efforts exhibit either mesh independence or a realistic material dependent fracture criteria but not both. The purpose of this work is to work toward a fracture prediction tool encompassing both previously mentioned properties that relies on physical, measurable material parameters, which can capture crack trajectories in various materials.

Chapter II presents a review of the field of fracture mechanics. Linear elastic fracture mechanics as well as elastic-plastic fracture mechanics methods are briefly discussed. The mechanisms that cause fracture to occur at the micron-level are discussed along with methods to approximate them. Numerical methods that are used to represent fracture and the propagation of cracks are also presented.

Chapter III presents an error analysis for the theory used throughout this work to represent fracture in a simulation. It is shown that the theory is suitable for linear elastic and elastic-plastic material behavior. Methods for visualization used in this research are also presented.

Chapter IV presents an error analysis performed on the crack surface displacements for symmetric cracks emanating from a hole in an infinite plate subjected

to a remote stress and loaded crack face. The formulas accepted in the literature for the displacements were compared with boundary element simulation results and a numerical integration of a closed form expression for crack surface displacements. The error analysis was used to develop new, more accurate equations of crack surface displacements for the geometry subjected to a remote stress.

Chapter V investigates J_2 plasticity's capability to capture damage evolution preceding a crack tip in monotonic fracture. A damage based crack advance criterion is introduced that incorporates damage evolution into crack propagation. Results show the effect of damage and the new separation criterion on crack propagation. Two variants of J_2 plasticity are then introduced in an attempt to capture the damage evolution occurring in front of the crack tip and to tie the damage to the direction of crack advance.

Lastly, Chapter VI summarizes the work completed in this research and suggests the direction for future research.

CHAPTER II

FRACTURE MECHANICS

Introduction

Fracture mechanics pertains to the study of bodies with a pre-existing crack or the likelihood of body to develop a crack. The field of fracture mechanics has been very active since the mid-1900's. The purpose of this chapter is to review the important concepts in the field as they relate to monotonic fracture and the modeling of stable crack growth. The motivation of the fracture mechanics field and consequently for these concepts was to find a single parameter that could describe not only when a crack should grow but also in which direction it would grow. The stress intensity factor and the energy release rate were introduced as single parameters for crack growth in linear elastic materials. The J-integral and CTOD/CTOA parameters were developed to provide a single parameter for crack growth with nonlinear elastic and plastic materials, respectively. A review of damage mechanics and several micromechanical models are also presented because much work has been performed to make damage accumulation the single parameter to drive crack growth. The current methods for the numerical representation of fracture and crack propagation will also be reviewed in this chapter.

Linear Elastic Fracture Mechanics

Loading ductile materials that have a pre-existing crack produces an inelastic response in the region surrounding the crack tip. There are circumstances where the inelastic response can be ignored and one can assume that the body responds the same regardless of proximity to the crack. One such condition is when the amount of inelastic response is small compared to the length of the crack. If this condition is satisfied, then one can safely assume that the material acts as a linear elastic body which means the stresses are infinite at the crack tip and stresses can be described by the strength of the singularity (linear elastic fracture mechanics). The fundamental assumptions of linear elastic fracture mechanics are:

1. The crack is assumed to have zero radius tip.
2. The material near the crack tip is assumed to behave just as the material far away from the crack tip.
3. The area of yielding is small compared to the dimensions of the cracked body.

Stress Intensity Factor

Stress intensity factors are defined with respect to the loading of the crack where the loading can be broken into three components as shown in Figure 2.1. The loading applied to a crack can be decomposed into a linear combination of these three modes. A crack is subjected to Mode I loading when the loading is normal to the crack surface, i.e. tension. Mode II loading is when the crack surface is subjected to a shear that causes one

crack surface to slide over the other surface. A crack loaded by a shear in such a way that faces are bending out of the page is denoted as Mode III loading.

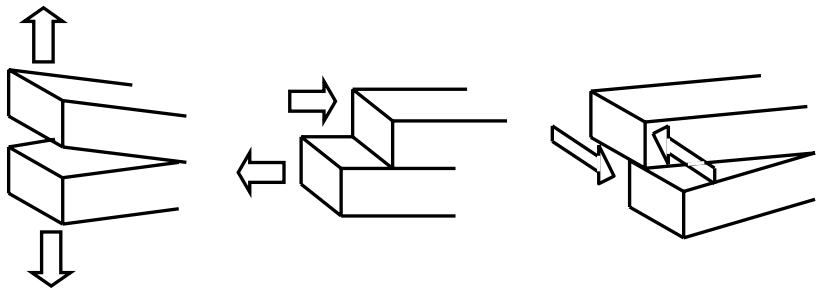

Figure 2.1 Three types of loading that can be applied to a crack. (a) Mode I; (b) Mode II; (c) Mode III.

Closed-form solutions of the stress field have been derived for a multitude of cracked body problems. Inglis (1913), Westergaard (1939), Irwin (1957), Sneddon (1946), and Williams (1957) are some of the earliest examples. The solutions are usually given in terms of polar coordinates (r,θ) with the coordinate system's origin located at the crack tip. Using the polar coordinate system along with linear elastic material behavior, the stress field takes the form

$$\sigma_{ij} = \frac{k}{\sqrt{r}} f_{ij}(\theta) + \sum_{n=0}^{\infty} \alpha_n r^{\frac{n}{2}} g_{ij}^{(n)}(\theta) \tag{2.1}$$

where k is a material constant, α_n are constant, and f and g are functions of θ. The displacements can be represented in a similar manner and are a function of $\sqrt{r}$ which implies they are bounded as one approaches the crack tip. Also, the leading term in the equations of stress is unique for any crack geometry and loading. This property allows the use of the strength of the singularity, k, as a fracture mechanics parameter to

characterize crack growth under linear elastic conditions. The stress intensity factor appears in the leading term of the equation above by defining it to be $K = k\sqrt{2\pi}$.

The stress field of an object using linear elastic fracture mechanics can be decomposed into the stress contributions for each of the modes present in the loading:

$$\sigma_{ij}^{I} = \frac{K_I}{\sqrt{2\pi r}} f_{ij}^{I}(\theta) + H.O.T. \tag{2.2}$$

$$\sigma_{ij}^{II} = \frac{K_{II}}{\sqrt{2\pi r}} f_{ij}^{II}(\theta) + H.O.T. \tag{2.3}$$

$$\sigma_{ij}^{III} = \frac{K_{III}}{\sqrt{2\pi r}} f_{ij}^{III}(\theta) + H.O.T. \tag{2.4}$$

where the subscript of the K's denotes the loading mode. The total stress is obtained by adding the individual contributions for each type of loading if there are multiple modes present and is written in equation form as

$$\sigma_{ij}^{tot} = \sigma_{ij}^{I} + \sigma_{ij}^{II} + \sigma_{ij}^{III} + H.O.T. = \frac{K_I}{\sqrt{2\pi r}} f_{ij}^{I}(\theta) + \frac{K_{II}}{\sqrt{2\pi r}} f_{ij}^{II}(\theta) + \frac{K_{III}}{\sqrt{2\pi r}} f_{ij}^{III}(\theta) + H.O.T. \tag{2.5}$$

From equation (2.1), it can be seen that as one gets close to the crack tip all the terms of the series approach zero except for the leading term. Thus, the leading term indicates the nature of the stress field as one approaches the crack tip.

Small scale yielding is defined to be when the size of the area that is yielding in the stress field is small compared to a characteristic length of the cracked body, in this case the length of the crack. Small scale yielding must be occurring in order to use a stress intensity factor to determine the onset of fracture. If small scale yielding is occurring then the leading term of equation (2.2) can describe the stress of the material ahead of the crack. Thus, the stress intensity factor is assumed to completely characterize

the loading conditions and the behavior near the crack tip. The stress intensity factor can then be used to determine a failure criterion related to the material's fracture toughness, denoted by K_{Ic}. The fracture toughness parameter is not a material constant, but rather it has a strong dependence on the strain-rate and temperature (Dowling, 1983). The crack is grown by comparing the stress intensity factor to K_{Ic} , and it should grow if the stress intensity factor is larger than the K_{Ic} for the material, assuming the small-scale yielding assumption is valid.

The next section presents the energy balance approach to fracture and the relationship that exists between it and the stress intensity factor method.

Griffith and Irwin Energy Balance Methods

Energy balance concepts applied to fracture predate the stress intensity factor approach by thirty years, but have not had the same amount of acceptance. Griffith (1920) originally formulated an energy balanced approach for the special case of brittle fracture. It has also been successfully applied to highly nonlinear and elastoplastic fracture mechanics. Griffith used Inglis' (1913) solution of a through crack (length of 2a) in an infinite plate subjected to an applied stress, σ, that results in mode-I loading to calculate the strain energy that could cause a crack to advance. Assuming the material is in a plane stress condition, Griffith calculated the decrease in strain energy as

$$\Omega = \frac{-\pi a^2 \sigma^2}{E} \tag{2.6}$$

and that the surface energy required to form the crack (length 2*a*) is

$$W_s = 4a\gamma_s \tag{2.7}$$

where γ_s is the surface energy per unit area for the material. One of Griffith's primary assumptions was that crack growth would continue provided that the rate of released strain energy is larger than the energy required to advance the crack. In equation form this becomes

$$\frac{d}{da}\left(\Omega + W_s\right) \geq 0 \tag{2.8}$$

where *da* is the increment in crack length. The onset of fracture would be the minimum of equation (2.8), i.e.

$$\frac{d}{da}\left(\Omega + W_s\right) = 0\,. \tag{2.9}$$

The stress σ_f that exists at the minimum of equation (2.9) is termed the fracture or critical stress and is found to be

$$\sigma_f = \sqrt{\frac{2E\gamma_s}{\pi a}}\,. \tag{2.10}$$

This formulation is restricted to brittle material because plasticity is another form of energy dissipation, and this method consequently cannot be applied to materials that exhibit large plastic deformation.

Irwin (1948) and Orowan (1955) observed that even brittle fracture events had significant inelastic deformation on the fracture surface. The magnitude of energy dissipated by the plastic deformation was several orders of magnitude larger than that of the surface energy used to calculate σ_f by Griffith. The modified Griffith equation independently derived by Irwin and Orowan that incorporates the effect of plastic deformation is

$$\sigma_f = \sqrt{\frac{2E(\gamma_s + \gamma_p)}{\pi a}} \tag{2.11}$$

with γ_p representing the plastic work.

Irwin (1957) later coined the phrase "strain energy release rate," denoted by G to represent all forms of resistance to fracture in a material. The equation for the critical stress with respect to G_c is

$$\sigma_f = \sqrt{\frac{EG_c}{\pi a}} \tag{2.12}$$

where G_c is the critical value of G when crack advance occurs.

Relation between G and K

The formulation of the Griffith energy balance above was based on the analytical solution of a through crack with length 2a in an infinite plate subject to a remote tensile stress. The stress intensity factor for this configuration is known to be

$$K = \sigma\sqrt{\pi a} \tag{2.13}$$

while the energy relate rate G is

$$G = \frac{\sigma^2 \pi a}{E} \tag{2.14}$$

Thus when crack advance occurs, i.e. $\sigma = \sigma_c$, the relation between G_c and K_c becomes

$$G_c = \frac{K_c^2}{E} \tag{2.15}$$

It is now shown that this relation holds for any geometry and crack configuration. Consider a crack of length a+ Δa as shown in Figure 2.2.a and the new crack profile due to stresses applied in Figure 2.2.b. As long as Δa is sufficiently small such that the stress

field can be accurately modeled by the leading term, i.e. the stress intensity factor, one can show that the relation holds between G and K.

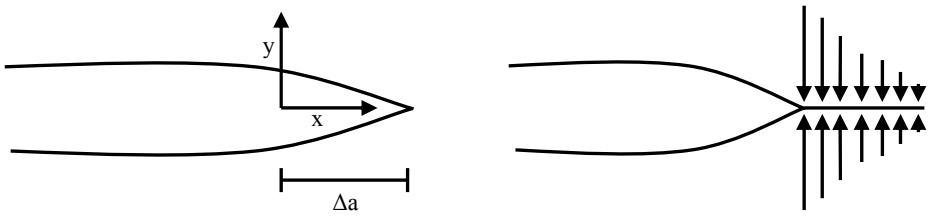

(a) (b)

Figure 2.2 (a) Original crack configuration and (b) crack closure due to stresses applied to a width Δa from the crack tip (Anderson, 2005).

The amount of work required to close the crack using the stress σ is

$$\Delta U = \int_{x=0}^{x=\Delta a} dU(x) \tag{2.16}$$

where U(x) is the increment of work done at the point x and can be calculated by

$$dU(x) = 2 \times \frac{1}{2} F_y(x) u_y(x) = \sigma_{yy}(x) u_y(x) dx \tag{2.17}$$

which is the integration of the force-displacement curve where u_y represents the displacement in the y-direction. The equation of displacement for the crack, u_y, is

$$u_y = \frac{(\kappa+1) K_I(a+\Delta a)}{2\mu} \sqrt{\frac{\Delta a - x}{2\pi}} \tag{2.18}$$

where $K_I(\bullet)$ is the stress intensity factor at a point, μ is the shear modulus, and

$$\kappa = \begin{cases} \dfrac{3-\nu}{1+\nu} & \text{plane stress} \\ 3-4\nu & \text{plane strain} \end{cases} \tag{2.19}$$

The stress needed to close the crack of length a as a function of the stress intensity factor at a is

$$\sigma_{yy} = \frac{K_I(a)}{\sqrt{2\pi x}} \tag{2.20}$$

Utilizing the fact that energy release rate can be written in terms of work required to close the crack under a fixed load, we have

$$G = \lim_{\Delta a \to 0}\left(\frac{\Delta U}{\Delta a}\right) \tag{2.21}$$

Now the relation between G and K for any type of geometry and crack configuration can be readily obtained by substitution and gives

$$G = \lim_{\Delta a \to 0} \frac{(\kappa+1)K_I(a)K_I(a+\Delta a)}{4\pi\mu\Delta a}\int_0^{\Delta a}\sqrt{\frac{\Delta a - x}{x}}dx = \frac{K_I^2}{E} \tag{2.22}$$

under a plane stress assumption. For other modes of loading one can get a similar relationship. This derivation assumes that as the crack advances it will remain in the same plane as the original crack. While this is a reasonable assumption for mode I loading, it is not realistic when applying a mixed-mode loading condition.

The stress intensity factor and energy balance approaches both require the small scale yielding condition. For materials with significant levels of plastic deformation in the fracture process zone (e.g. metallic alloys), it is necessary to consider the plastic deformation or nonlinear elastic response that occurs in the neighborhood of the crack tip. The next section presents several elastic-plastic methods of fracture mechanics.

Elastic-Plastic Fracture Mechanics

The inelastic response cannot be ignored when the small scale yielding assumption is violated due to a large plastic zone, and this is the case for highly ductile materials such as metallic alloys. The predominant methods of modeling fracture when the small scale yielding hypothesis is violated are presented in this section.

J-Integral

Previously mentioned fracture criteria, K and G, are both based on the assumption that the material has a linear consitutive behavior. Rice (1968) introduced an integral, later denoted the J-integral,

$$J = \int_{\Gamma} \left(w dy - T_i \frac{\partial u_i}{\partial x} ds \right) \tag{2.23}$$

where w is the strain energy density, u_i are the components of displacement, T_i are the traction components along the boundary Γ, that can be used for a fracture criterion for a nonlinear elastic material. The integral is path-independent and represents a type of energy release rate for a nonlinear elastic material containing a crack. This section presents the derivation of the equivalence of J to the energy release rate for nonlinear materials, the path independence of the integral, and its application to fracture simulations. The relationship between J and G, the energy release rate for elastic materials will also be shown.

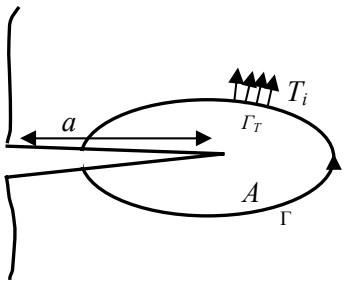

Figue 2.3 A two-dimensional body with a crack that is bounded by a curve Γ.

To show that J is a measure of energy release rate, suppose there is a two-dimensional body with a crack that is bounded by a curve Γ as in Figure 2.3 and that the stresses only depend on two coordinates in a Cartesian system. Assuming no body forces exist, the potential energy can be expressed as

$$\Pi = \int_A w dA - \int_{\Gamma_T} T_i u_i ds \tag{2.24}$$

where w is the strain energy density, A is the area of the body, Γ_T is the part of the boundary where the tractions T_i are applied, and u_i is the displacement. If one assumes that there is a virtual extension of the crack, then the change in potential energy in with a representing the area of the crack is

$$\frac{d\Pi}{da} = \int_A \frac{dw}{da} dA - \int_\Gamma T_i \frac{du_i}{da} ds \tag{2.25}$$

Fixing the coordinate system's origin on the crack tip, the coordinate axis moves as the crack advances. Thus, the differentiation with respect to a becomes

$$\frac{d}{da} = \frac{\partial}{\partial a} + \frac{\partial x}{\partial a}\frac{\partial}{\partial x} = \frac{\partial}{\partial a} - \frac{\partial}{\partial x} \tag{2.26}$$

Differentiating the strain energy density with respect to the coordinate, x, gives

$$\frac{\partial w}{\partial x} = \frac{\partial w}{\partial \varepsilon_{ij}} \frac{\partial \varepsilon_{ij}}{\partial x} = \sigma_{ij} \frac{\partial \varepsilon_{ij}}{\partial x} \tag{2.27}$$

which is only applicable in dealing with elastic materials. Applying small strain assumptions

$$\frac{\partial w}{\partial x} = \frac{1}{2} \sigma_{ij} \left[\frac{\partial}{\partial x} \left(\frac{\partial u_i}{\partial x_j} \right) + \frac{\partial}{\partial x} \left(\frac{\partial u_j}{\partial x_i} \right) \right] = \sigma_{ij} \frac{\partial}{\partial x_j} \left(\frac{\partial u_i}{\partial x} \right) \tag{2.28}$$

Applying equations (2.26-2.28) and the principle of virtual work to equation (2.25) one obtains

$$\frac{d\Pi}{da} = \int_{\Gamma} T_i \frac{\partial u_i}{\partial x} ds - \int_{A} \frac{\partial w}{\partial x} dA \tag{2.29}$$

Using the divergence theorem, the fact that $n_x ds = dy$ where n_x is the unit vector in the x-direction, and reorganizing terms, yields

$$-\frac{d\Pi}{da} = \int_{\Gamma} \left(w dy - T_i \frac{\partial u_i}{\partial x} ds \right) = J \tag{2.30}$$

and shows that the J contour integral is equivalent to the energy release rate for elastic materials.

The path independence of the J-integral is now shown. Let Γ be a close curve as in Figure 2.3. Applying Green's Theorem to the J-integral, equation (2.30), gives

$$J = \int_{\Gamma} \left(w dy - T_i \frac{\partial u_i}{\partial x} ds \right) = \int \left[\frac{\partial w}{\partial x} - \frac{\partial}{\partial x_j} \left(\sigma_{ij} \frac{\partial u_i}{\partial x} \right) \right] dx dy \tag{2.31}$$

Observe that equation (2.28) can be written as

$$\frac{\partial w}{\partial x} = \sigma_{ij} \frac{\partial}{\partial x_j} \left(\frac{\partial u_i}{\partial x} \right) = \frac{\partial}{\partial x_j} \left(\sigma_{ij} \frac{\partial u_i}{\partial x} \right). \tag{2.32}$$

Thus the integrand in equation (2.31) vanishes and proves that the J-integral is zero for any close curve Γ.

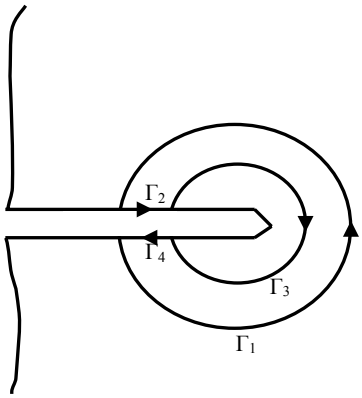

Figure 2.4 A closed curve around a crack tip consisting of four segments.

Consider the path shown in Figure 2.4 to prove that the J-integral is path independent. Because the J-integral is equal to zero for a closed curve, we know that

$$J = J_1 + J_2 + J_3 + J_4 = 0. \tag{2.33}$$

The portions of the path along the horizontal crack surface are traction free and dy=0 which means that the J-integral for curves Γ_2 and Γ_4 is 0.0. This implies that J_1=-J_2. which allows us to conclude that any counterclockwise path around the crack will give the same value. Thus the path independence of J has been shown.

It is important to write out the assumptions made in developing the J-integral as a calculation of energy release rate in nonlinear elastic materials, and they are:

1.) No body forces are applied.

2.) The material behaves elastically.

3.) Crack faces are traction free.

4.) The traction applied on the boundary of the curve, Γ, is independent of the crack length *a*.

Provided that these hold true and in addition the elastic behavior is linear then $J=G$.

The next section presents the requirements where *J* can be used in similar manner to *K* in linear elasticity to define the conditions near the crack tip.

HRR Theory

Hutchinson (1968) and Rice and Rosengren (1968) independently showed that the J-integral characterizes the conditions near the crack tip for a nonlinear elastic material just as the stress intensity factor does for a linear elastic material and their work was denoted as HRR theory. The HRR fields are based on small strain relationships and assume the material behavior follows a Ramberg-Osgood relationship which for uniaxial deformation can be expressed as

$$\frac{\varepsilon}{\varepsilon_o} = \frac{\sigma}{\sigma_o} + \alpha\left(\frac{\sigma}{\sigma_o}\right)^n \tag{2.34}$$

where σ_o is the yield stress, $\varepsilon_o = \sigma_o / E$, n is the strain hardening exponent, and α is a dimensionless material specific constant.

They were able to show that the stress and strain relationships must follow a *1/r* behavior near the crack tip for the strength of the singularity to be characterized by *J* and to ensure path independence of the J-integral. They also showed that if *r* is assumed to be so small that the elastic contribution to strain becomes negligible, i.e. within the plastic zone, then the fields take on a power-law behavior and can be represented by

$$\sigma_{ij} = \sigma_o \left(\frac{EJ}{\alpha \sigma_o^2 I_n r} \right)^{\frac{1}{n+1}} \tilde{\sigma}_{ij}(n,\theta) \tag{2.35}$$

$$\varepsilon_{ij} = \frac{\alpha \sigma_o}{E} \left(\frac{EJ}{\alpha \sigma_o^2 I_n r} \right)^{\frac{n}{n+1}} \tilde{\varepsilon}_{ij}(n,\theta) \tag{2.36}$$

where I_n is an integration constant, and $\tilde{\sigma}_{ij}$ and $\tilde{\varepsilon}_{ij}$ are dimensionless functions dependent on n, θ, and the stress-state. From the equations above it is clear that J controls the strength of the singularity as K did for linear elastic fracture mechanics.

The HRR theory has some limitations. If r is chosen to be too small then the HRR equations become invalid because they do not account for the blunting effect of the crack tip. However, r must still be chosen small enough so that the equations are evaluated within the plastic zone. Thus, there are circumstances when the value J is capable of characterizing the conditions of the crack tip, J-dominance, and are briefly presented next.

J-controlled fracture

To characterize a material's behavior in a region surrounding the crack tip using the J-integral several conditions must be satisfied. The J-integral can be used to describe the behavior assuming there is small-scale yielding, the material behavior includes hardening, and the loading is quasi-static and monotonic. J cannot accurately capture the material response when the increment of crack advance, Δa, is large compared to in-plane dimensions. The size of Δa must be small compared to the region of J-dominance which is contained in the plastic zone. J-dominance refers to the region near the crack tip where J completely characterizes the behavior of the material. Even though the unloading

behind the crack tip and the nonproportional loading violate assumptions made for HRR fields, *J* can still describe the crack growth if the elastic unloading and nonproportional loading are contained in the *J*-dominant region as indicated in Figure 2.5.

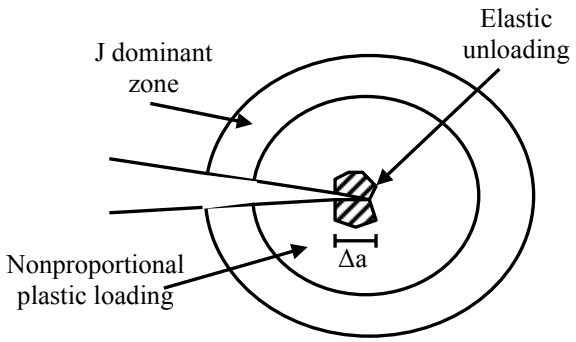

Figure 2.5 Regions of *J*-controlled crack growth. (Anderson, 2005)

CTOD/CTOA

Crack tip opening displacement (CTOD) is another common method of determining crack growth. Crack growth is said to occur once the displacement at a point on the crack reaches a critical value. The method was developed independently by Wells (1961) and Irwin (1961). Wells found as a specimen was loaded, the crack faces separated, and plastic deformation caused the crack to blunt. The magnitude of the blunting increased proportionally to the material's toughness. Thus, Wells suggested that the blunting or opening at the crack tip could be used as a measure of toughness or resistance to fracture.

Irwin assumed that the plasticity surrounding the crack tip caused the crack to act as though it was longer. By assuming that the crack is virtually longer by some length *r* (e.g. *r* represents the plastic zone radius) one can now calculate the amount of separation

at the original, undeformed crack tip location. The displacement at a point on a crack surface a distance *r* behind the virtual tip is given by

$$u_y = \frac{4}{E'} K_I \sqrt{\frac{r}{2\pi}} \tag{2.37}$$

where

$$r = \frac{1}{2\pi}\left(\frac{K_I}{\sigma_{YS}}\right)^2 \tag{2.38}$$

which is Irwin's plastic zone size. Thus, the separation would be

$$\delta = 2u_y = \frac{4K_I^2}{\pi\sigma_{YS}E'}. \tag{2.39}$$

Restricting the material to small scale yielding, δ or CTOD can be related to *G*, the Griffith's energy release rate by

$$\delta = 2u_y = \frac{4G}{\pi\sigma_{YS}}. \tag{2.40}$$

There are two conventions as to where the displacement are measured as shown in Figure 2.6. Figure 2.6.a shows the convention used in the above derivation. The other method, shown in Figure 2.6.b, is to measure at the intersection of a 90° vertex with the crack surfaces. If the crack tip is assumed to blunt in a semicircular shape, then the two conventions are the same. An alternative crack-advance criterion, crack tip opening angle, is discussed next and can be determined from crack tip opening displacement calculations.

The CTOD method is often preferred because it can be determined quickly by inspection and has been used extensively in the prediction of fracture and crack growth for thin sheets of metals (Newman, Jr., et. al., 1984, and James and Newman, Jr., 2002).

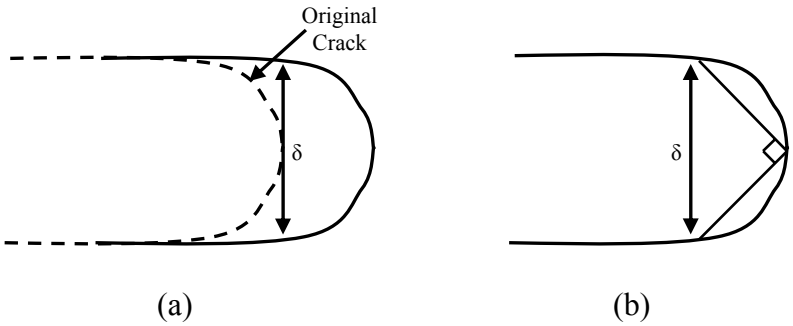

Figure 2.6 Methods of calculating crack opening displacements.

Crack tip opening angle (CTOA) was proposed by Shih et al. (1979) and derived by Rice et. al (1980) using Prandtl slip-line theory as a method of determining crack advance based on one parameter for thin metal sheets. One of the requirements for the specimen is that the crack-length-to-thickness ratio and the ligament-to-thickness ratio are greater than or equal to 4.0 (Newman et. al., 2003). This guarantees low constraint near the crack tip. As indicated in the standard ASTM E2472-06, the angle is measured 1.0 mm behind the crack tip. To calculate a more accurate value of the angle, the angle is calculated at several distances- 0.5 mm, 1.0 mm, and 1.5 mm as shown in Figure 2.7 , and averaged to obtain a final crack-tip opening angle. CTOA can be related to the crack tip opening displacement measured 1.0mm behind the crack tip by

$$\psi = 2\tan^{-1}\left(\frac{CTOD}{2}\right). \tag{2.41}$$

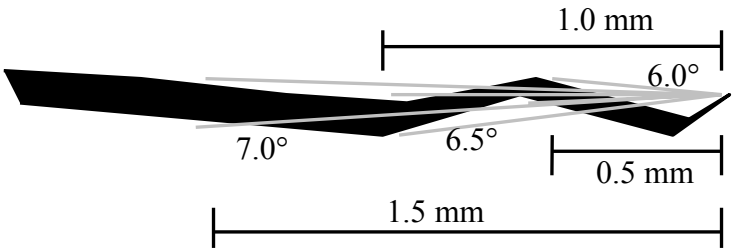

Figure 2.7 A typical crack path showing how the angle is measured to calculate the CTOA value. (Newman et. al., 2003)

Exclusion Region Theory

This section summarizes the motivation for and development of the exclusion region theory (ER) as given in detail in Rashid (1997a). In linear elastic fracture mechanics, the stress values have a singularity as one approaches the separation front which is not physically realistic. The exclusion region theory takes a small region surrounding the separation front and prescribes a generalized constitutive model derived from the local constitutive relation. By modeling the separation front in this way, the unbounded stress field is removed and no asymptotic analysis is applied. Removing this region from the local response allows the user to introduce a criterion to determine fracture and results in a representation that allows us to predict when surface separation will occur (Rashid, 1997a; 1997b).

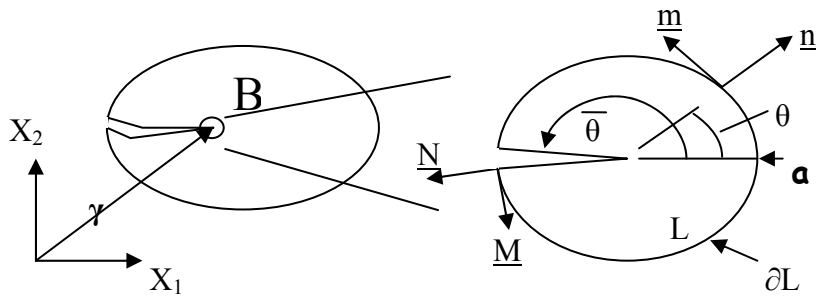

Figure 2.8 Body containing a crack with an exploded view of the tip contained in the proposed new exclusion region along with the normal (n, N) and tangent (m, M) vectors defined. (Rashid, 1997a)

The formulation of the generalized continuum model for the exclusion region from the bulk constitutive response is summarized below, and Figure 2.8 is used for reference. Figure 2.8 shows an example of the exclusion region, **L**, centered on the crack tip or separation front within a body **B**. The exclusion region's shape is a circle for simplicity of implementation but can be any shape. The deformation occurring on the boundary of the exclusion region can be arbitrary and should suffer a discontinuity at some point on the boundary due to the crack opening. Because the generalized constitutive model applied within the exclusion region is to be derived from the local constitutive model that applies to **B/L**, one can conclude that the material points on the boundary of the exclusion region, ∂**L**, obey the local material model. To calculate the tractions on ∂**L**, a displacement on ∂**L** must also be accessible. The displacement on ∂**L** can only be available if a displacement exists everywhere within the exclusion region. Consequently, the primary factor of the generalized continuum model is the displacement field. The displacement field must contain a jump across the new free surface, match the arbitrary displacements along ∂**L**, and have a single value at the crack tip. The

displacement field formulation must allow the exclusion region to be in force and moment equilibrium as a result of the traction distribution along $\partial\mathbf{L}$.

The prescribed displacement field in equation (2.42) is not assumed to accurately capture the material response near the tip, but instead is a field that satisfies the conditions previously mentioned. Utilizing polar coordinates (r, θ) centered at the crack tip, one example used by Rashid (1997a), the form of the displacement field, $\underline{u}$, in **L** is taken to be

$$\begin{aligned} \underline{u}(r,\theta) &= \frac{r}{a}\left[\underline{\hat{u}}(\theta) + \underline{w}P(r,\theta)\right] + \left(1-\frac{r}{a}\right)\underline{g} - \frac{r}{a}\left(1-\frac{r}{a}\right)v\underline{m}(\theta), \\ P(r,\theta) &= H\left(\theta - \bar{\theta}(a)\right) - 1 + \frac{\bar{\theta}(r) - \bar{\theta}(a)}{2\pi}, \quad 0 \le r < a, \quad \bar{\theta}(r) \le \theta < \bar{\theta}(r) + 2\pi, \\ w &= \underline{\hat{u}}\left(\bar{\theta}(a)\right) - \underline{\hat{u}}\left(\bar{\theta}(a) + 2\pi\right) \end{aligned} \tag{2.42}$$

where $\underline{\hat{u}}$ is the displacement on the exclusion region's boundary, $\underline{g}$ is the crack tip displacement, v controls the twisting contribution of the displacement at the tip, a is the exclusion region radius, $\underline{m}(\theta)$ is the tangent vector, H is the Heaviside function, and $\bar{\theta}$ describes the new free surface. The parameters $\underline{g}$ and v are free parameters and must be calculated so that the exclusion region is in moment and force equilibrium. Scale invariance cannot be guaranteed for the generalized constitutive model used in the exclusion region. The radius of the region controls the behavior in the region because the displacements in the region are tied to the displacements on the boundary. The radius is also directly related to the amount of crack advance, and this is why the exclusion region radius is an independent parameter that also has the property of a characteristic length scale.

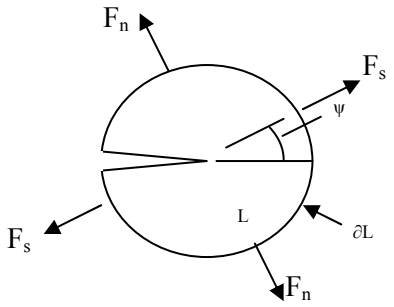

Figure 2.9 The exclusion region with an angle of advance, ψ, and the forces acting on the region. (Rashid, 1997a)

Introducing the exclusion region allows the criterion which indicates crack advance to be independent of the solution of the boundary-value problem. Crack advance in the exclusion region theory occurs by using a separation criterion. The separation criterion is the condition that determines when the material in the exclusion region has reached a critical state, and the separation point (crack tip) advances through the material. The common fracture criteria possibilities for the separation criterion such as K, $\mathcal{G}$, J, and CTOD/CTOA, were discussed in previous sections of this chapter. A fracture criteria related to $\mathcal{G}$ is the maximum energy release theory introduced by Cotterell and Rice (1980) which stated that the direction of crack advance was such that the direction caused the strain energy release rate $\mathcal{G}$ to be a maximum and this maximum has to be larger than a prescribed critical value, $\mathcal{G}_c$. A fracture criterion related to the stress field is the maximum circumferential stress theory (Erdogan and Sih, 1963) that suggested crack extension/advance would occur in the direction that yields the maximum value of the circumferential stress and would grow once the maximum value surpasses a prescribed critical value related to the Mode-I critical stress intensity factor. Both criteria can be correlated to experimental mixed mode fracture results within the realm of linear elastic

fracture mechanics. Or, because the tractions are known on the boundary of the exclusion region, it could be assumed that there is a relation between the tractions and free surface formation. Figure 2.9 shows the exclusion region with ψ representing the angle of advance, and F_n and F_s are the normal and shear forces on the boundary defined with respect to the angle of advance by

$$F_n = \int_{\bar{\theta}(a)}^{\bar{\theta}(a)+\psi} \underline{t}(\theta) \cdot \underline{\hat{m}} a d\theta \tag{2.43}$$

$$F_s = \int_{\bar{\theta}(a)}^{\bar{\theta}(a)+\psi} \underline{t}(\theta) \cdot \underline{\hat{n}} a d\theta \tag{2.44}$$

where $\underline{t}$ is the traction on the boundary, $\underline{\hat{n}} \equiv (\cos\psi, \sin\psi)$, and $\underline{\hat{m}} \equiv (-\sin\psi, \cos\psi)$. One possible separation criterion is a force-based fracture criterion,

$$\Phi = \frac{1}{a}\left[\langle F_n \rangle^2 + \beta F_s^{\,2}\right]^{\frac{1}{2}} \tag{2.45}$$

with $\beta \in [0,1]$, and the crack advances once Φ reaches a critical value, Φ_c. This particular fracture criterion has been shown to be equivalent to K_{Ic} (Rashid, 1997a) for isotropic linear elastic materials and is confirmed again later in the next chapter.

Parameters in the constitutive model needed for the separation function in equation (2.45), namely a , β, and Φ_c, are introduced. Within the context of a linear elastic response, the product $\sqrt{a}\Phi_c$ can be determined and β can be determined with mixed-mode tests. As plasticity is introduced into the material response, a and Φ_c can be measured independently. It should be noted that the exclusion region radius is not dependent on the amount of inelastic deformation near the crack tip, and can be thought of as a true material parameter. But, if a is taken to be too large the exclusion region could engulf the region of plasticity, causing the model to assume the material around the

tip behaves elastically. Also, if β is assigned zero, then the fracture criterion defined by equation (2.45) reduces to the maximum circumferential stress criterion.

This section presented an overview of the prevalent methods used to model fracture in elastic-plastic materials where significant plasticity occurred. The next section presents an overview of the microstructural-based approaches to model fracture and the mechanisms that cause fracture to occur.

Microstructural-based Modeling

Microstructural-based modeling is a way to link measurable material characteristics such as voids and second phase particles at various length scales to a macroscopic material response. By linking the material properties to a material's response, it is possible for a model to be used in predicting the response for different scenarios such as loading conditions and temperatures. It has been seen experimentally, as in Figure 2.10, that defects and particles affect the onset of fracture and the path of crack growth. In a virgin material, the specimen in Figure 2.10 would fracture along the centerline of the gauge section. Instead, the flow lines and gas pores caused from casting process significantly alter the crack path. One could never match simulation and experimental results for this case without including the microstructure effect, so it would be prudent to include as many of these into the material's response (Garrison and Moody, 1987).

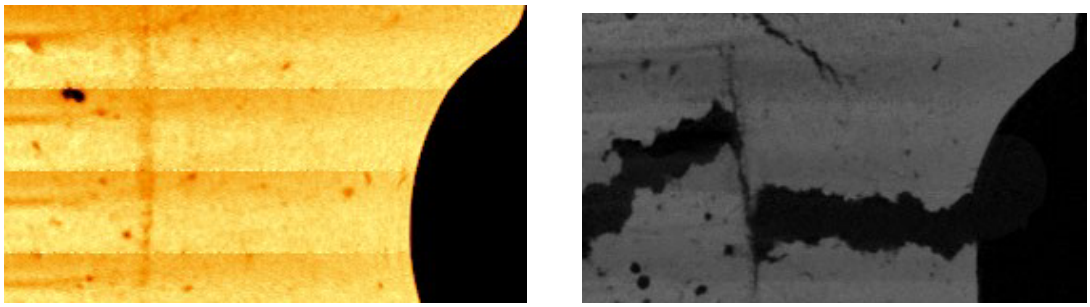

(a) (b)

Figure 2.10 (a) Image of a computed tomography scan of a magnesium specimen. Dark areas represent initial porosity. (b) Image showing that the crack path was heavily influenced by the initial distribution of porosity (Gullett, 2005).

Damage Mechanisms

Nucleation, growth, and coalescence of voids are commonly referred to as damage mechanisms. The nucleation of voids is defined as the introduction of voids in a material. This is typically occurs at the particle-matrix interface, when particles in the material fracture, or along a grain boundary when grains separate. The growth of voids occurs when a void in the material increases in volume. The coalescence of voids occurs when multiple voids become one. Coalescence is considered to occur in one of two ways: two voids growing until they join, or when a void sheet mechanism occurs between the voids.

Void growth is the most extensively studied damage mechanism and as a result many equations exist to predict void growth. The void growth equations determine the growth by calculating the change in radii of the void. Two of the most commonly used void growth equations are due to work done by McClintock (1968) and Rice and Tracey (1969). The McClintock equation specifies the rate of change in the radii using the formula

$$\dot{r} = \frac{R_0\sqrt{3}}{2(1-n)}\left[\sinh\left((1-n)\alpha\frac{tr(\underline{\sigma})}{J_2(\underline{\sigma})}\right)\right]\dot{\varepsilon}^p \tag{2.46}$$

where n is dependent on the strain hardening exponent assuming the material behavior is described by power-law hardening, R_0 is the initial void radius, α is a constant, and ε^p is the plastic strain. The form of the equation assumes the voids grow spherically. The Rice and Tracey equation was developed assuming the initial void is a sphere in an infinite body but grows into an ellipsoid as it is subjected to a remote stress. They concluded that rate of increase for the average radii was

$$\dot{r} = R_0 e^{\alpha\varepsilon^p} \tag{2.47}$$

where

$$\alpha = 0.283 \cdot e^{1.5*\frac{\sigma_H}{\sigma_{vm}}} \tag{2.48}$$

and R_0 is the initial void radius, σ_H is the hydrostatic pressure, and σ_{vm} is the von Mises stress.

Both equations allow for void growth in tension but not in compression or torsion. Neither model incorporates void interaction which is related to coalescence. Also, both equations are dependent on plastic strain for any radii' evolution to occur.

Related to void growth equations are equations which measure a void volume fraction. The void volume fraction is the percentage of material in a region that consists of voids. Two examples are the Cocks-Ashby equation (Cocks and Ashby, 1981) and the Gurson model (Gurson, 1977).

Cocks and Ashby developed their model to calculate the growth of voids located on grain boundaries at a constant stress under creep conditions and extended to multiaxial

stress states. They assume that the voids in the material are spherical until the material fractures. Their equation for the rate of change of void volume fraction is

$$\dot{\phi} = \left[\frac{1}{(1-\phi)^m} - (1-\phi) \right] \sinh\left[\frac{2(2m-1)}{(2m+1)} \frac{\sigma_H}{\sigma_{vm}} \right] \dot{\varepsilon}^p \quad . \tag{2.49}$$

The volume fraction rate equation was related to macroscopic rate of plastic strain. Note that in a state of hydrostatic tension, equation (2.49) will not give accurate results. Cocks (1989) altered equation (2.49) to account for a hydrostatic loading effect on damage accumulation. The next section reviews a continuum damage approach developed by Gurson (1977) that uses a void volume fraction parameter.

Gurson Model

Continuum damage mechanics have been applied to fracture mechanics and the most prevalent example is the Gurson model (Gurson, 1977). Other models assume that damage is only a function of the deviatoric plastic deformation and disregard the fact that damage can accumulate in the presence of hydrostatic loads. The yield criterion and flow rule for the Gurson model approximate the behavior of porous ductile materials and are derived from a rigid plastic limit analysis where a void is approximated by a cylindrical body containing a cylindrical void. The effect of the voids is averaged over an element using a representative volume element. The model has been modified several times (Tvergaard, 1982; 1990) and the model's yield surface now captures the effect of a periodic array of voids and void growth in a hydrostatic load (equations (2.52-2.54)).

The flow potential, Φ, that only incorporates void growth is represented by

$$\Phi = \frac{\sigma_e^2}{\bar{\sigma}^2} + 2q_1 f \cosh\left(\frac{3q_2\sigma_m}{2\bar{\sigma}} \right) - \left(1 + q_3 f^2\right) = 0 \tag{2.50}$$

with q_1, q_2, and q_3 used to fit the potential for a periodic array of voids and $\boldsymbol{\sigma_e}$, $\boldsymbol{\sigma_m}$, $\bar{\sigma}$, and f representing von Mises stress, mean stress, flow stress (yield), and current void fraction respectively. To add void coalescence and nucleation, Tvergaard and Needleman (2001) replaced f with

$$f^* = \begin{cases} f & \text{for } f \le f_c \\ f_c - \dfrac{f_u^* - f_c}{f_F - f_c}(f - f_c) & \text{for } f > f_c \end{cases} \tag{2.51}$$

where f_c, f_u^*, and f_F are fitting constants.

The rate equation for the void volume fraction is

$$\dot{f} = \dot{f}_{growth} + \dot{f}_{nucleation} \tag{2.52}$$

with

$$\dot{f}_{nucleation} = A\dot{\bar{\sigma}} + \frac{B}{3}\dot{\sigma}_{kk} \tag{2.53}$$

and

$$\dot{f}_{growth} = (1 - f)\,tr\underline{D}^p \tag{2.54}$$

where A and B are scalars. Equation (2.57) assumes that nucleation can be driven by plastic-strain as well as being stress-controlled. Chu and Needleman (1980) suggest that the constant A follow a normal distribution and that B should be equal to zero to capture strain-controlled nucleation. Because equation (2.54) is a compatibility condition that imposes the criterion that volumetric growth is proportional to

$$\frac{1}{1 - f} \tag{2.55}$$

and this proportionality is a result of an assumption of volumetric growth of a spherical void, any modification of this simple assumption requires a complete restructuring of the flow potential.

Xia and Shih (1995) showed how one could model crack growth using the Gurson model for damage. They simulated a specimen that was symmetric about the initial crack and inserted cells in front of the crack tip. The cells had an initial damage value and behaved according to the Gurson-Tvergaard constitutive model while the rest of the specimen behavior was characterized by J_2 flow theory. The cells are represented by elements and along the symmetry line, and the nodes of the elements (similar to a cohesive model) are released simulating crack growth once the critical value of damage is attained.

Another continuum model used to capture the evolution of damage and model its effect on the stress-state is the Bammann-Chiesa-Johnson internal state variable plasticity model and is presented next.

Internal State Variable plasticity-damage model

The internal state variable (ISV) plasticity and damage model created by Bammann (1984, 1987) and Bammann and Aifantis (1989) and modified later by Horstemeyer and Gokhale (1999) has been used to model plastic deformation of several metallic alloys (Horstemeyer, 2000, 2001). The model is based on the assumption that the inelastic flow is dependent on the values of stress and the internal variables introduced. The internal variables are used to describe the state of the material at a continuum point. There are two internal variables related to the plasticity portion of the

model, isotropic (scalar) and kinematic (tensor) hardening. The internal variables evolution is derived from a physically based mechanism, dislocation mechanics, and is implemented in a hardening-minus-recovery format (Bammann and Aifantis, 1989). The evolution equations for the internal state variables include temperature and strain rate history effects. Void nucleation and coalescence were added to the model by Horstemeyer and Gokhale (1999).

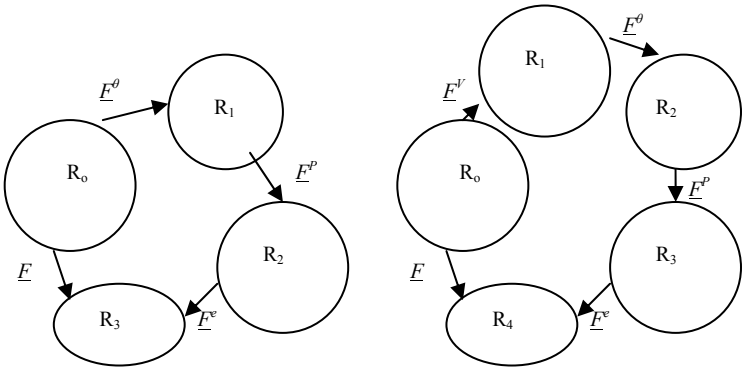

Figure 2.11 Graph showing the multiplicative decomposition of the deformation gradient with and without an intermediate damaged state.

The kinematics of the ISV plasticity model are described using a multiplicative decomposition of the deformation gradient into its elastic, plastic, and thermal parts, $\underline{F}^{e}$, $\underline{F}^{p}$, and $\underline{F}^{T}$ respectively, as shown in Figure 2.11. The total deformation gradient can then be represented as

$$\underline{F} = \underline{F}^{e}\,\underline{F}^{p}\,\underline{F}^{T} \tag{2.56}$$

with the additional assumption of isotropic thermal conditions; i.e.

$$\underline{F}^{T} = F_{T}\,\underline{I} \tag{2.57}$$

where F_T is a scalar value. This decomposition creates two local intermediate configurations between the reference and current configuration, B_0 and B. The intermediate configuration, $\overline{B}$, defined by $\underline{F}^p \underline{F}^T$ is useful due to the additive decomposition of the velocity gradient and strain tensors. The velocity gradient, $\underline{l}$, can be calculated as

$$\underline{l} = \dot{\underline{F}}\underline{F}^{-1} = \dot{\underline{F}}^e \underline{F}^{e^{-1}} + \underline{F}^e \dot{\underline{F}}^p \underline{F}^{p^{-1}} \underline{F}^{e^{-1}} + \underline{F}^e \underline{F}^p \underline{F}^T \underline{F}^{T^{-1}} \underline{F}^{p^{-1}} \underline{F}^{e^{-1}} = \underline{l}^e + \underline{l}^p + \underline{l}^T. \quad (2.58)$$

The symmetric part and skew-symmetric parts of the velocity gradient are denoted by $\underline{D} = sym(\underline{l})$ and $\underline{W} = skew(\underline{l})$.

For the current configuration, *B*, the symmetric and skew-symmetric parts of the velocity gradient are

$$\underline{D}^e = \underline{D} - \underline{D}^p - \underline{D}^T \quad (2.59)$$

and

$$\underline{W}^e = \underline{W} - \overline{\underline{W}}^p \quad (2.60)$$

where

$$\underline{D}^T = \alpha \dot{T} \underline{I} \quad (2.61)$$

and

$$\underline{D}^p = \sqrt{\frac{3}{2}} f(T) \sinh\left[\frac{\left|\underline{\sigma'} - \frac{2}{3}\underline{\alpha}\right| - \{\kappa + Y(T)\}}{V(T)}\right] \frac{\underline{\sigma'} - \underline{\alpha}}{\left\|\underline{\sigma'} - \underline{\alpha}\right\|} \quad (2.62)$$

and

$$\underline{W}^p = 0. \quad (2.63)$$

Following the convention of a Prandtl-Reuss flow rule the plastic flow, $\underline{D}^p$, is assumed to occur in the direction $\underline{|\sigma - \alpha|}$. The hyperbolic sine function controlling the magnitude of $\underline{D}^p$ was chosen to follow the theory of thermally activated dislocation motion and the Garafalo (1963) formulation which describes a power law breakdown. The internal variable $\underline{\alpha}$ represents kinematic hardening which describes the center of the yield surface at the macroscopic scale.

ϕ is the internal variable used to represent the scalar damage variable, and its purpose in the deviatoric flow rule is to concentrate the stress, which increases the flow and can cause softening. In addition, damage degrades the elastic moduli of the material as seen in the equation (2.76). The evolution equation for ϕ was motivated by the Cocks-Ashby model (Cocks-Ashby, 1980) and is given by equation (2.49). When ϕ is introduced into the system of equations, an additional kinematic degree of freedom associated with both volumetric and shape change from the presence of the voids must be introduced. The resulting decomposition of the velocity gradient becomes

$$\underline{D}^e = \underline{D} - \underline{D}^p - \underline{D}^V - \underline{D}^T \tag{2.64}$$

where

$$\underline{D}^p = \sqrt{\frac{3}{2}} f(T) \sinh \left[\frac{\left| \underline{\sigma'} - \frac{2}{3}\underline{\alpha} \right| - (\kappa + Y(T))(1-\phi)}{V(T)(1-\phi)} \right] \frac{\underline{\sigma' - \alpha}}{\underline{\|\sigma' - \alpha\|}} \tag{2.65}$$

and

$$\underline{D}^V = \frac{\dot{\phi}}{1-\phi}\underline{I} \tag{2.66}$$

The functions *f(T), Y(T),* and *V(T)* incorporate the yield of the material's temperature dependence with an Arrhenius-type temperature dependence. The function *f(T)* determines when the yield of the material becomes dependent on the strain rate. *Y(T)* is the rate independent yield. *V(T)* is responsible for capturing the magnitude of the yield's dependence on strain rate. The functions are represented by

$$V(T) = C_1 e^{\left(-C_2/T\right)}, \quad Y(T) = C_3 e^{\left(-C_4/T\right)}, \quad f(T) = C_5 e^{\left(-C_6/T\right)} \tag{2.67}$$

where C_1-C_6 are fitting parameters. The ISV model's hardening parameters and damage equations are physically driven and are affected by a material's loading history, loading rate, and temperature and are consistent with continuum kinematics and thermodynamics. The internal state variables which represent the isotropic and kinematic hardening in a macroscopic sense, κ and $\underline{\alpha}$, respectively, evolve in a hardening-minus-recovery format, and their evolution equations are written as

$$\dot{\kappa} = H(T)\left\|\underline{D}_d^p\right\| - \left[R_d(T)\left\|\underline{D}_d^p\right\| + R_s(T)\right]\kappa^2 \tag{2.68}$$

$$\underline{\alpha} = h(T)\underline{D}_d^p - \left[r_d(T)\left\|\underline{D}_d^p\right\| + r_s(T)\right]\|\underline{\alpha}\|\underline{\alpha} \tag{2.69}$$

The functions $r_s(T)$ and $R_s(T)$ are scalar functions for static recovery, $r_d(T)$ and $R_d(T)$ are scalar functions for dynamic recovery, and *h(T)* and *H(T)* are hardening moduli. The equations of the scalar static and dynamic recovery functions are

$$r_d(T) = C_7 e^{\left(\frac{-C_8}{T}\right)} \tag{2.70}$$

$$r_s(T) = C_{11} e^{\left(\frac{-C_{12}}{T}\right)} \tag{2.71}$$

$$R_d(T) = C_{13} e^{\left(\frac{-C_{14}}{T}\right)} \tag{2.72}$$

$$R_s(T) = C_{17} e^{\left(\frac{-C_{18}}{T}\right)} \tag{2.73}$$

The slopes of the hardening are determined using the form

$$h(T) = C_9 - C_{10} T \tag{2.74}$$

$$H(T) = C_{15} - C_{16} T \tag{2.75}$$

Using the multiplicative decomposition of the deformation gradient above and assuming an isotropic linear elastic response holds for the intermediate configuration (see Figure 2.11), $\overline{B}$, and when the Cauchy stress, $\underline{\sigma}$, is convected with elastic spin, $\underline{W}^e$, the following relationship is obtained in the current configuration

$$\overset{\circ}{\underline{\sigma}} = \dot{\underline{\sigma}} - \underline{W}^e \underline{\sigma} - \underline{\sigma} \underline{W}^e = \lambda(1-\phi) tr(\underline{D}^e) I + 2\mu(1-\phi)\underline{D}^e - \frac{\dot{\phi}}{1-\phi}\underline{\sigma} \tag{2.76}$$

where λ and μ as seen in equation (2.76) are the material's Lame constants and $\underline{D}^e$ is given by equations (2.59-2.66).

The internal state variable plasticity damage model is capable of accurately predicting the first occurrence of failure in complicated geometry and loading scenarios (Bammann et. al. 1996 and Horstemeyer, 2001) because it incorporates the material's microstructure-property relationships (voids, temperature dependence, rate dependence, etc…). The damage model's success in predicting first element failure in a finite element simulation is why it is considered in this fracture propagation research.

This section presented an overview of the damage mechanisms that occur in ductile materials which lead to fracture initiation and propagation. It also summarized the

modeling efforts to incorporate microstructure-property relationships into material models.

Numerical Implementation of Fracture

Predicting fracture initiation and propagation in an arbitrary geometry is a very difficult process, but the computational resources available at present make the investigation of crack growth a realizable goal. The predominant methods used to model monotonic fracture are presented in this section.

The Finite Element Method

The finite element method (FEM) is currently the most prevalent tool used to perform fracture simulations. FEM methodology can be broken into three parts: divide the domain into parts, calculate an approximate solution for each part, and accumulate the approximate solutions to obtain the solution to the whole problem.

Consider the body in Figure 2.12.a. To obtain an accurate discretization as shown in Figure 2.12.b into small parts or elements, the discretization needs to follow three rules. First, the elements must be nonempty and have a piecewise-continuous boundary. Secondly, the union all the elements must sum exactly to the whole body. Thirdly all of the elements should have a null intersection. The elements are described by points called nodes that are introduced where the elements are in contact with each other and the boundary of the domain as seen in Figure 2.12.b. A shape function for each node is now introduced as a means of approximating a solution for the whole element in terms of the values known at its nodes. Shape functions associated with the nodes of an element must

form a basis for that element. A shape function must also be equal to one for the node it is defined and zero at every other node.

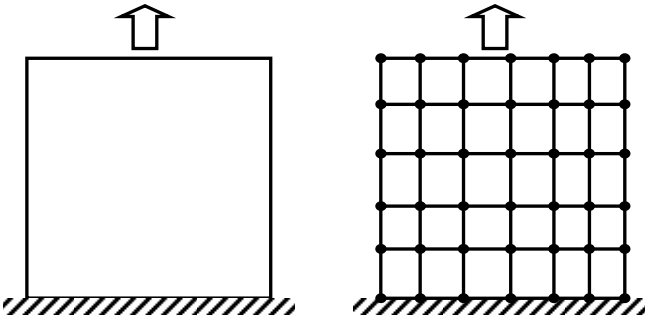

(a) (b)

Figure 2.12 (a) The body that is to be analyzed. (b) The discretization of the body into elements by inserting and connecting nodes (dots).

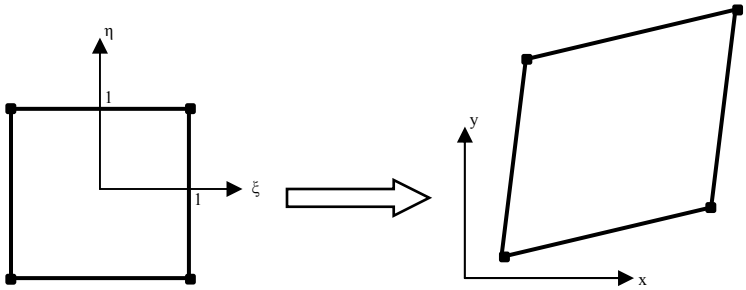

Figure 2.13 Mapping of a parent element to arbitrary finite element.

The finite element methodology is made computationally efficient by determining the shape functions for standard element geometries, called parent elements, including a various numbers of nodes. The shape functions are automatically assured to satisfy the previously mentioned conditions. A remapping procedure (Figure 2.13) is introduced to map the element onto the parent element geometry.

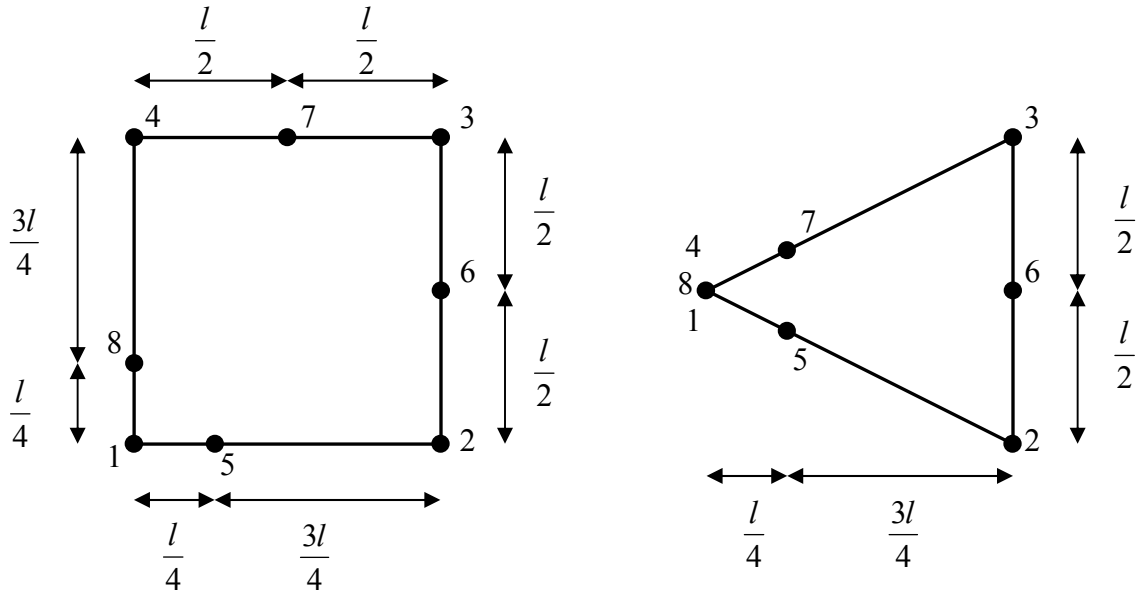

Figure 2.14 Quarter-point element and the resulting element after collapsing nodes.

Linear elastic fracture mechanics exhibits a singularity in the stress field at the crack tip and polynomial basis functions cannot capture the singularity behavior. Sharp gradients in the stress are present as one approaches the crack tip, which requires a very fine mesh in the vicinity of the tip if one wants to capture this behavior. As the element size is decreased, the solution for a cracked body cannot accurately represent the stress field using conventional continuum elements and the solution will ultimately diverge as the element size continually decreases (Chan et. al., 1970). The development of quarter-point elements by both Barsoum (1976) and Henshell and Shaw (1975) was a large step toward modeling linear elastic fracture near the crack tip accurately using the finite element method. The quarter-point element worked by starting with an eight node serendipity element and collapsing nodes 4 and 8 onto node 1 as shown in Figure 2.14. This introduces a singularity with a square-root behavior emanating from the three coinciding nodes to a surrounding small neighborhood.

Crack growth is dependent on K, $\mathcal{G}$, or J within the realm of linear elastic fracture mechanics simulations. The stress intensity factor, K, can be found by either a direct computation or backed out from the energy value $\mathcal{G}$.

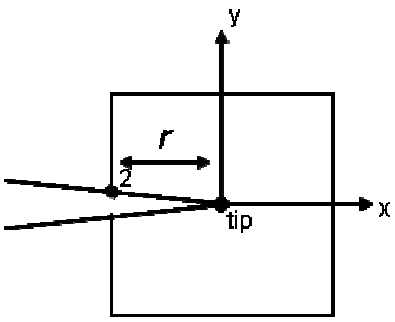

Figure 2.15 Node locations with respect to crack tip for displacement correlation.

One of the earliest approaches to calculate K directly is the displacement correlation approach credited to Chan et. al. (1970). It required the use of displacements at nodes along the crack face. The nodes must be close enough to the crack tip so they are in the area where K dominates the stress field. Requiring a node to be in the K-dominated region, forces the mesh to be highly refined in the area surrounding the crack tip. K is found with the displacement, y_2, at the node shown in Figure 2.15 on the crack face from the asymptotic relationship

$$K_I = \frac{\mu(y_2 - y_{tip})\sqrt{2\pi}}{(2-2\nu)\sqrt{r}} \tag{2.77}$$

where μ is the shear modulus, ν is Poisson's ratio, r is the distance between the node and the crack tip, under plane strain conditions.

An approach based on energy methods is the virtual crack extension method introduced by Parks (1974) and Hellen (1975). The energy release rate G can be

expressed in terms of the total potential energy, assuming the absence of body forces and external forces are constant during crack growth,

$$G = \frac{1}{2} u^T \frac{\partial K}{\partial a} u = J \tag{2.78}$$

with u being the nodal displacement, K is the stiffness matrix, and a is the crack length. If the other assumptions listed in the J-integral section are satisfied, then one can say that $G=J$. The change of the stiffness matrix is calculated by using a finite difference approximation while perturbing the crack length a small amount. The stress intensity factor can then be calculated using

$$G = \frac{\alpha K_I^2}{E} \tag{2.79}$$

where

$$\alpha = \begin{cases} \left(1-\upsilon^2\right) & \text{plane strain} \\ 1 & \text{plane stress} \end{cases} \tag{2.80}$$

Haber and Koh (1985) used an analytical expression for the derivative of the stiffness matrix which was later shown to be equivalent to the domain version of the J-integral (Li et al., 1985) by Bank-Sills and Sherman (1992). The analytical expression was more accurate than the finite difference scheme, and converting the contour integral to a domain integral allowed for a more direct implementation into finite element codes.

Accommodating crack advance in conventional finite element codes requires that the mesh must be altered to allow for the new crack surface. A common method to accommodate crack growth is based on node-release. This method is most often utilized when the geometry and loading being studied are symmetric about the crack plane. The crack plane is chosen as the plane of symmetry which allows for simply releasing nodes

along the "boundary" once it is determined that the crack grows. This restricts the crack growth to the symmetry plane, and node-release is most often used when the crack path is known a priori to be along this plane.

Another method of adjusting the mesh once the crack tip has advanced is adaptive remeshing. Once a crack is advanced, the region containing the new crack surface must be remeshed. H-type refinement consists of subdividing the original elements into smaller versions of the original element where the error is deemed too large. These refinement methods are driven by reducing an error value. Error norms are crucial for an efficient and accurate refinement procedure, and are covered extensively in Babuska and Reinbuoldt (1978), Zeinkiewicz and Zhu (1987), Oden et al. (1989), and Bathe and Lee (1994).

Another type of adaptive remeshing that is most closely related to the arbitrary mesh replacement method (Rashid, 1997a) utilized in this piece of research is the s-type developed by Fish (1992). The s-type finite element method consists of overlaying the finite element mesh with a patch of finite elements in an area that is known to have large gradients. The large gradients could not be detected with the large element size in the original mesh. The displacements in the patch and the elements the patch covers are summed to find the final displacements.

The next subsection presents an alternative to the finite element method, the meshless method, and its approach to fracture.

Meshless Methods

Meshless methods have been extensively researched in the solid mechanics community for the last twenty years by Belytschko et. al. (1996) and Babuska et. al. (2003). Meshless methods provide a means to model objects that have large local deformation, and this provides a distinct advantage over the FEM for problems involving large local deformation and changing topologies. Element distortion associated with large local deformation can significantly degrade approximation accuracy. Avoidance of large element distortions requires remeshing- a difficult and time consuming task for arbitrary geometries in three dimensions. Similarly, topology changes associated with crack growth requires remeshing. Meshless methods alleviate this problem by discretizing in terms of nodes only. To accurately model crack growth in fracture applications, a meshless implementation must insert additional nodes in front of the crack tip as seen in Figure 2.16.

(a) (b)

Figure 2.16 Crack propagating using meshless methods where dots represent nodes. (a) The initial configuration; (b) After the crack has grown.

Within the context of damage based fracture prediction, there only seem to be two options when dealing with meshless methods. One involves a smeared damage approach accounting for void growth while the other is based on linear elastic fracture mechanics.

The first method discussed is the damage representation. Meshless simulations using a void growth model to represent damage have been extensively studied (Liu, 2000 and 1999). In this type of simulation, a crack can be present in the initial configuration just as in the finite element method. With the void growth model, for nodes that have damage, the stiffness begins to deteriorate as the damage increases. Once the damage reaches a critical value, the stiffness becomes zero and the node no longer contributes to the resistance of the material. The final result of the simulation is a damage field displayed on the initial configuration.

The explicit representation of a crack is based on the linear elastic fracture mechanics' concept of a stress intensity factor (Rao and Rahman, 2000; Hildebrand, 2009). As the specimen is loaded and the stresses increase at the tip, the crack extends some pre-defined increment. With the extension of the crack a node is introduced at the new crack tip. This method allows for the crack to be explicitly lengthened and will give a more realistic representation of the effect of the crack on the stress field in the material, but the crack extension not tied to any physical property of the material or its microstructure.

Meshless methods have their drawbacks. In the meshless method technique, one must still evaluate area and boundary integral, which leads to a major problem. A node's contribution to the stiffness matrix is dependent on being able to integrate the shape functions around the boundary as well as be able to integrate the derivative of the shape

functions over the area. The integration of the derivatives can be cumbersome because their order of continuity is larger than C^0. Also meshless methods' stiffness matrix is not sparse which is contributed to the lack of explicitly defined connectivity between nodes. The computational requirement to determine node connectivity, especially for irregular node distributions, can be on the order of n^ρ with $\rho>>1$ and can result in an unbounded cycle of iterations to obtain convergence (Idelsohn *et al.* 2002). Because of these characteristics most of the meshless methods are a hybrid of meshless with a mesh background. The mesh background allows the user to define integration using common quadrature techniques which are a strength of the finite element method (Dolbow and Belytschko, 1998; Li and Liu, 2004; Liu , 2002).

The next subsection presents the first method used to predict fracture which incorporated some of the processes that occur in front of the crack tip.

Cohesive Zone Method

A cohesive zone is a region inserted between elements and provides the connectivity among the elements. The behavior of the zone is defined by a stress-displacement relationship which will control when the cohesive zone fails. A cohesive zone model simulates fracture by inserting small cohesive zones ahead of the crack tip seen in Figure 2.17.a. The cohesive approach introduces the physics of the material-specific failure process. The two driving parameters for crack advance with this approach are: the tensile strength value and the fracture energy (Borst, 2004; Elices, 2002). One relationship for ductile materials, shown in Figure 2.17.b, linearly increases until reaching a critical pre-defined value of stress or tensile strength , f, as shown in

Figure 2.17.b. Upon maintaining *f* for a determined time the material behavior begins to soften. The fracture energy is defined as

$$\Gamma_c = \int \sigma du \tag{2.81}$$

where σ is stress, *u* is displacement, and Γ_c represents the work per unit area necessary to open the cohesive surface.

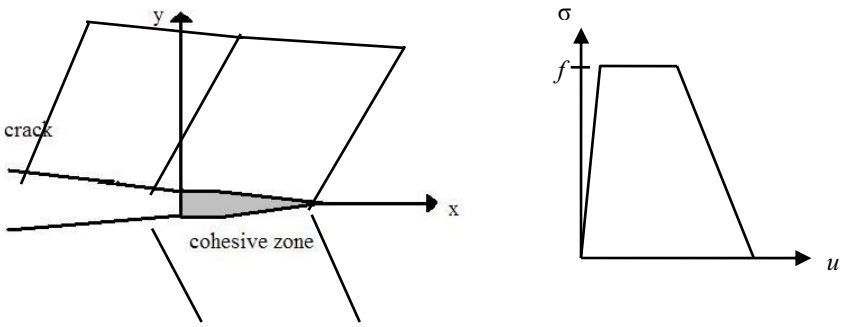

Figure 2.17 (a) Cohesive zone placement with respect to the crack. (b) Stress-displacement relationship for the ductile material in the cohesive zone.

The cohesive zone approach was created to predict elastic-plastic fracture in ductile metals as well as in quasi-brittle materials (Dugdale, 1960; Barenblatt, 1962). The concept was created as an alternative to the linear elastic fracture mechanics approach which causes a singularity to exist in the stress field at the crack tip. By placing the zone in front of the crack, the stress singularities incurred with the classical approach are alleviated. Cohesive zone model are very accurate in modeling of layers of material sandwiched together where a crack can only grow on boundaries of layer interfaces (Schellekens, 1992). Cohesive zone modeling has also successfully modeled ductile material experiments. The modeling success many times arises from performing the

experiment first and then inserting cohesive zone elements within the simulation where the crack should grow (Rots, 1991). In this case, the cohesive zone internal variables must be obtained from a real fracture experiment as explained in Sun and Jin (2006). Xu and Needleman (1994) accounted for arbitrary crack propagation by inserting cohesive elements between all continuum elements in a simulation. The crack could still only propagate along element boundaries, and an insertion of cohesive zones between all elements caused artificial softening to occur. It is clear that while cohesive zones can predict crack growth accurately in layered materials and can verify physical results (crack path a priori), a drawback is the results will exhibit mesh dependence and as a result are not suitable for arbitrary crack growth. The next subsection presents a brief summary of the extended finite element method.

Extended Finite Element Method

The extended finite element method (XFEM) was originally conceived by Belytschko and Black (1999) as a means of solving problems involving cracks without remeshing and providing mesh independence. The method entails adding enrichment functions, which are obtained from the near tip displacement fields for Modes I and II loading in a linear elastic isotropic material, to selected nodes near the crack tip. The near tip displacement fields for mode-I loading are

$$u = \frac{K_I}{2\mu}\sqrt{\frac{r}{2\pi}}\cos\left(\frac{\theta}{2}\right)\left[\kappa - 1 + 2\sin^2\left(\frac{\theta}{2}\right)\right] \tag{2.82}$$

$$v = \frac{K_I}{2\mu}\sqrt{\frac{r}{2\pi}}\sin\left(\frac{\theta}{2}\right)\left[\kappa + 1 - 2\cos^2\left(\frac{\theta}{2}\right)\right] \tag{2.83}$$

and mode-II are

$$u = \frac{K_{II}}{2\mu}\sqrt{\frac{r}{2\pi}}\sin\left(\frac{\theta}{2}\right)\left[\kappa + 1 + 2\cos^2\left(\frac{\theta}{2}\right)\right] \tag{2.84}$$

$$v = \frac{K_{II}}{2\mu}\sqrt{\frac{r}{2\pi}}\cos\left(\frac{\theta}{2}\right)\left[\kappa - 1 - 2\sin^2\left(\frac{\theta}{2}\right)\right] \tag{2.85}$$

The enrichment functions are the functions that span equations (2.82 – 2.85)

$$\{\gamma_i(r,\theta)\}_{i=1}^{4} = \left\{\sqrt{r}\cos\left(\frac{\theta}{2}\right), \sqrt{r}\sin\left(\frac{\theta}{2}\right), \sqrt{r}\sin\left(\frac{\theta}{2}\right)\sin(\theta), \sqrt{r}\cos\left(\frac{\theta}{2}\right)\sin(\theta)\right\} \tag{2.86}$$

and are added to the displacement formulation at nodes surrounding the crack surface and tip as seen in equations (2.87) and (2.88). XFEM uses the partition of unity property of finite elements that the shape functions must sum to unity to introduce the discontinuity, i.e. a crack, into the displacement field. The new displacement field equations for two dimensions become

$$u^h(x) = \sum_{i=1}^{n}\psi_i(x)\left(u_i + \sum_{j=1}^{n_E(i)}a_{ji}\gamma_j(r,\theta)\right) \tag{2.87}$$

$$v^h(x) = \sum_{i=1}^{n}\psi_i(x)\left(v_i + \sum_{j=1}^{n_E(i)}b_{ji}\gamma_j(r,\theta)\right) \tag{2.88}$$

where the polar coordinate system (r,θ) is centered on the crack tip, $\psi_i(x)$ are the finite element shape functions, a_{ji} and b_{ji} are the enrichment coefficients for node i, and $n_E(i)$ is the number of coefficients for node i. For an element containing the crack tip $n_E(i)$ is equal to four and zero for all the remaining elements. A jump function is inserted to introduce a discontinuity into the displacements of elements containing the remainder of the crack. XFEM can model a crack and its growth in two ways as shown in Figure 2.18. The crack can be modeled by enriching the nodes of the finite elements that contain the

crack, Figure 2.18.a. The alternative is for the crack to be part of the initial geometry and model subsequent growth using the XFEM method, Figure 2.18.b.

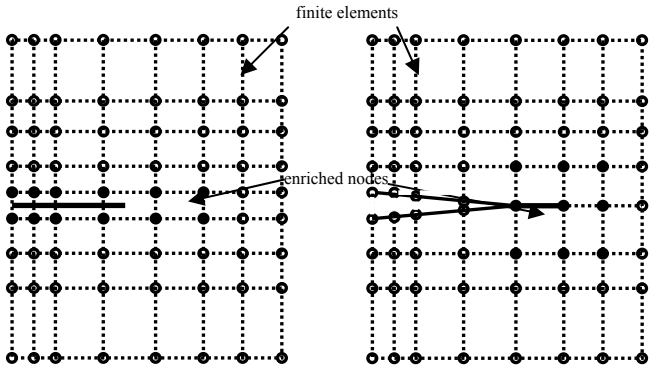

(a) (b)

Figure 2.18 Ways to model a crack with the extended finite element method. (a) The crack is modeled completely by enriching the nodes of the elements that it inhabits and that lie ahead. (b) Part of the crack is explicitly defined in the geometry while the crack tip is represented by enriching the nodes near the crack tip. (Belytschko and Black, 1999)

XFEM has features that are not realizable with conventional FEM. XFEM can accommodate curving cracks by mapping the enriched displacement field of straight crack onto the curved crack. XFEM also allows cracks to intersect incorporating a Haar function , *H(x,y)*, where

$$H(x,y)=\begin{cases} 1 \text{ for } y>0 \\ -1 \text{ for } y<0 \end{cases} \tag{2.89}$$

into the displacement field of elements the crack intersected with the exception of the element containing the tip (Moes et al., 1999). Daux et al. (2000) added the capability for cracks to intersect and branch without dependence on the discretization. Because of these capabilities and the lack of remeshing, XFEM has received wide acceptance in recent

years. Giner et al. (2009) introduced an Abaqus user element implementation of XFEM, and Abaqus v6.9 incorporates the XFEM for modeling discontinuities.

There are some weaknesses to the method. The XFEM lacks continuity and accuracy near a singularity. The error near the crack tip is due to the enrichment functions being derived for linear elastic, isotropic material. The nature of the enrichment functions restricts XFEM's applicability to small strain simulations. Because the XFEM is based on the FEM, sensitivities to mesh distortion still exist in the solution. Also there is not a clear way to provide contact forces if the fictitious opening closes. Thus, XFEM is a capable tool to use when considering small strain linear elastic, isotropic material, but in the presence of finite deformation and significant plasticity, the mesh dependence and error problems of the FEM still exist. The final method presented here is the numerical representation of the exclusion region theory.

Arbitrary Local Mesh Replacement Method

Rashid (1998) developed the arbitrary local mesh replacement (ALMR) method for implementing the exclusion region theory in a finite element program. The ALMR method is a finite element approach that utilizes two meshes: one that surrounds and remains centered on the exclusion region as the crack advances, and one for the remainder of the geometry.

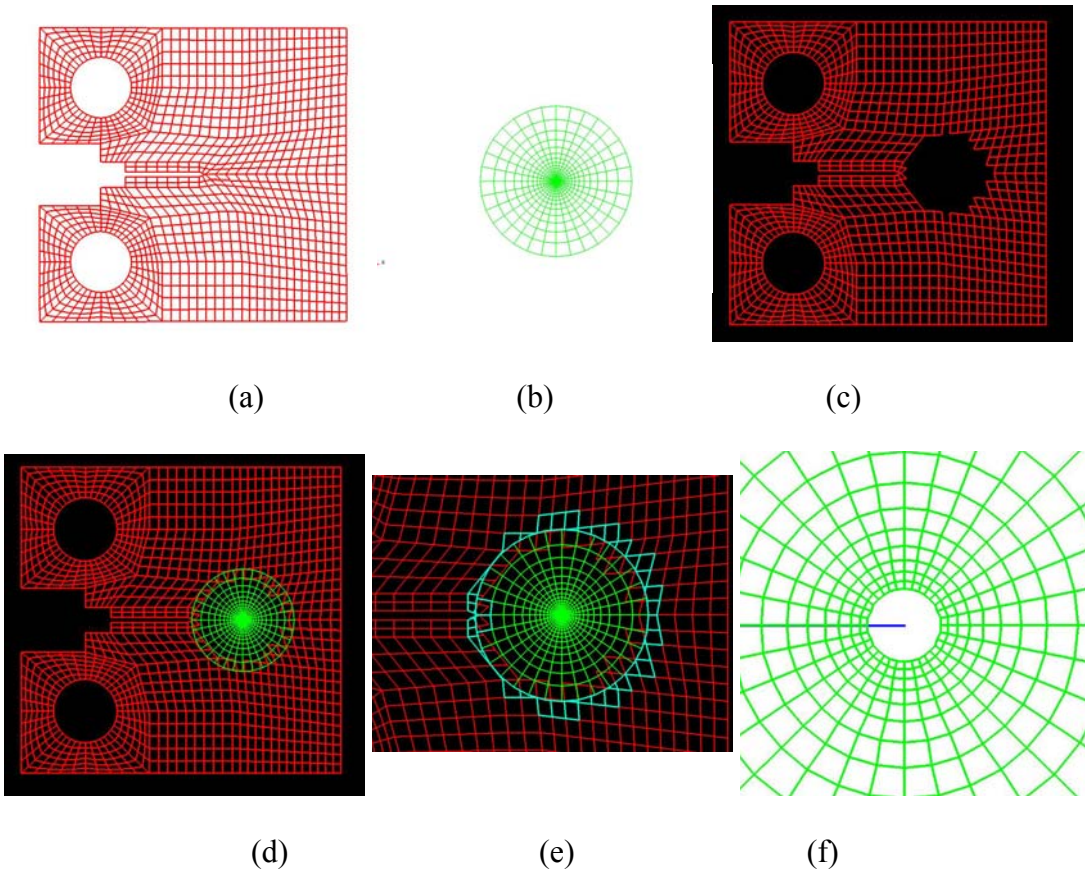

Figure 2.19 Step-by-step schematic of the arbitrary local mesh replacement theory; (a)background mesh, (b) patch mesh, (c) participating background elements, (d) overlaying of the two meshes, (e) the partial elements created when joining the meshes, (f) and the exclusion region at the center of the patch.

Consider the body in Figure 2.19.a. The ALMR method takes the body without a crack and discretizes it using quadrilateral finite elements. This finite element mesh will be denoted as the background mesh. A crack is introduced to the body as a series of line segments. The crack is not required to lie on element boundaries implying that the crack position is independent of the background mesh. The exclusion region is centered on the crack tip as seen in Figure 2.19.f and remains centered throughout the simulation as the crack propagates. The second mesh of the ALMR method that surrounds and is centered on the exclusion region is now created, shown in Figure 2.19.b. The second mesh,

denoted patch mesh, is characterized by the radius and number of wedges in the patch which are user-defined parameters. Like the background mesh, the patch is composed of bilinear quadrilateral elements. Once the patch mesh is created and superimposed onto the background mesh, the two meshes connectivity must be established. Any background elements completely covered by the patch do not participate in the solution, and these are the elements absent in Figure 2.19.c. Background elements still exist along the perimeter of the patch that participate in the solution but are partially covered as seen in Figure 2.19.d. These pieces of elements are used to create partial elements and are shown in blue in Figure 2.18.e. The crack is then used to create a free surface within the finite elements. If the crack cuts through an element, the element is duplicated and the crack is used to segment and resolve the connectivity of the elements. A new patch mesh is created centered on the exclusion region as the crack advances through the geometry. Crack propagation in traditional finite element programs requires continual adaptive remeshing and is one of the predominant problems due to computational cost and solution dependency on the mesh. While in the ALMR method, the only required remeshing is the task of generating the patch and resolving the intersection of the patch with the background mesh each time the crack propagates. With each crack advance, material properties must be remapped from the old mesh to the new mesh just as in conventional finite element methods. The remapping procedure used in the ALMR implementation is detailed in Rashid (2002).

Simulating a fracture problem with conventional FEM or cohesive zone methods can lead to a mesh dependent crack propagation path as discussed in previous sections. It can be seen that the nature of the ALMR method which does not include the crack tip in

the discretization obviates this situation, and its only requirement for crack advance is that the crack advance increment be at least the radius of the exclusion region.

There are two additional computational tasks with the ALMR method that do not exist in conventional FEM. They are enforcing displacement compatibility along the patch-background intersection and an integration rule for the resulting partial elements. Nodal displacements for nodes solely in the patch or the background can be determined by the shape functions from the occupying mesh. The nodal displacements for the nodes along the boundary of the patch and background have contributions from both meshes. A weak compatibility is enforced along this interface so that the difference between the displacement calculated by the patch and that of the background along the boundary is zero in an averaged sense. A typical partial element can be seen highlighted in blue in Figure 2.19.e. Due to the complex and arbitrary shape of the partial elements, integration points are located at the vertices and midpoints of the partial element. The weights are chosen in an optimal manner using a least-squares fit. The compatibility enforcement along the patch-background boundary and the integration routine for the partial elements are discussed in detail in Rashid (1998).

In summary, advantages to using the exclusion region theory are that it provides a mesh independent crack path, requires minimal remeshing and remapping, and it allows for the application of any separation function for crack advance. The ALMR capabilities will be improved by incorporating a material model which accounts for microstructure effects and developing a separation function dependent on measurable material parameters that are known to affect crack growth seen experimentally in materials.

Concluding Remarks

This chapter provided an overview of the major concepts in fracture mechanics. The concepts of both linear elastic and elastic-plastic fracture mechanics were touched upon. The microstructure mechanisms that lead to fracture were also reviewed along with efforts to relate these mechanisms to a material's macroscopic response. The predominant methods used to model fracture and predict crack propagation were briefly reviewed, and drawbacks for each of these methods were noted along with reasons why the method for this study was chosen. Chapter III presents the computational tasks taken in this study and an investigation proving the appropriateness of the ALMR method for our research efforts.

CHAPTER III

COMPUTATIONAL PROCEDURES AND SUITABILITY OF METHODS

Introduction

To simulate crack growth in this research, two computational tasks were undertaken. The first task was to change the method of visualizing results. The results were originally analyzed using a gnuplot based executable capable of producing monochrome plots. The visualization was changed so constitutive models with large numbers of state variables could be easily analyzed. The computational platform was also changed so material models could be readily changed. The next task was to show the suitability of the method used to model stable crack growth in this research. The far-field stress values and crack-surface displacements were analyzed to see what affect if any the two additional approximations taken in the ALMR method would have on these values.

Visualization

As computers have become more sophisticated they have allowed materials to be modeled in a more detailed manor. When using a material behavior that has multiple parameters that describe the material properties such as stress-state and damage and where the evolution of these variables is one of the desired outputs, it is important to have robust visualization capabilities. Previous implementations of the finite element code package, FEFRAC, provided a visualization package FRPOST, which utilized the

freeware visualization package gnuplot. This visualization package was changed to a commercial product, EnSight (2008), that provided a current visualization baseline to start from. Adjustments consisted of tracking all necessary values for the finite element simulations namely nodes, element connectivity, participating elements, magnification factor, stress values, and state variable values, and write them in a format of an EnSight input file.

FRPOST was capable of providing monochrome contour plots for the state variables in the existing material models along with the displacements and stresses at the nodes as shown in Figure 3.1(a). EnSight can represent field variables as color contour plots, and one can easily switch between variables in the visual field. It was decided to switch all the visualization from gnuplot to EnSight because of the increased detail that can be achieved in the analysis as seen in Figure 3.1(b). This decision was made due to the fact that this research effort utilized a material model with twenty plus variables that needed to be tracked.

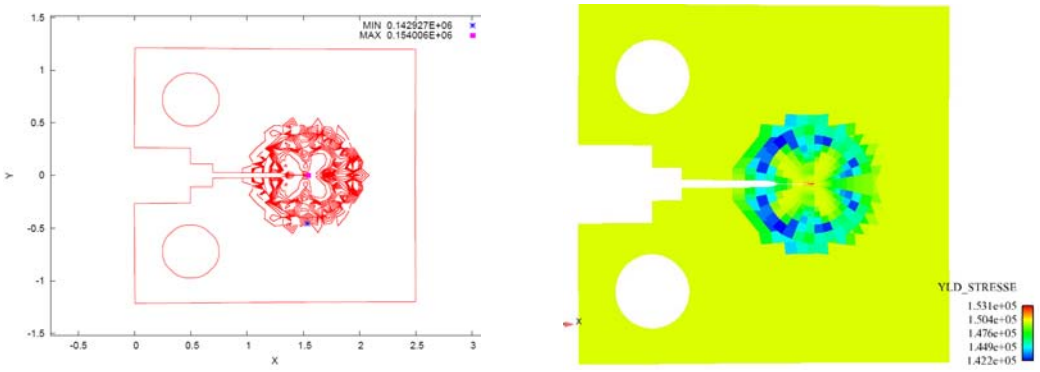

(a) (b)

Figure 3.1 Contour plots from (a) the original post-processor FRPOST and from (b) the new post-processor using EnSight.

EnSight has the capability to visualize multiple objects at once. The capability to temporarily remove the patch and/or the background mesh from the viewing window has been added. The values within the exclusion region can now be visualized as well.

Finally, notice that the patch elements increase in size as they radiate outward from the crack tip. Because the patch remains centered on the crack tip as the crack grows, it is possible to lose data from the neighborhood of the crack tip since the elements surrounding the original exclusion region area are a fraction of the size of those that will eventually cover the same area. The option has been added so state variables can be written to a file for visualization at the end of each time step and retained for subsequent time steps so that the sharp gradients will not be lost. These values are not being currently used, but were saved in the event future research warranted them.

Values visualized from a finite element program are either represented at integration points or nodes. The finite element program used bi-linear quadrilateral elements which have four integration points, and each integration point has a separate set of values that represent the stress and any other state variables used to describe the material behavior in the material model. The geometry of a simulation is defined by nodes and elements and as a result any values that are to be visualized must be for either the nodes or the elements in EnSight. To minimize writing and storage space, values were visualized on a per element basis for the new post-processor.

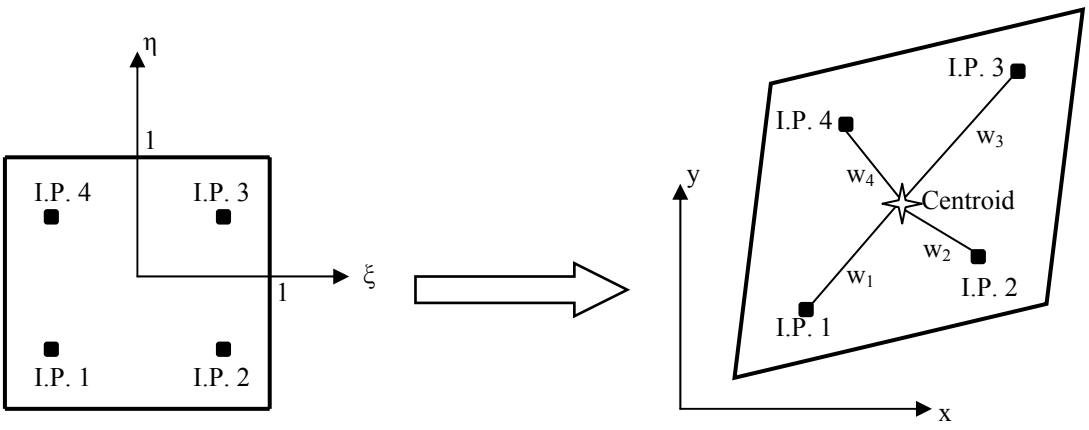

Figure 3.2 Master element and deformed element with integration points, distances, and centroid marked.

The method adopted to determine the values for an element from its integration points is described here. Consider the element in Figure 3.2. The first step is to calculate the centroid of the element and assume that this point faithfully represents the element. The centroid, c_e, is calculated by first determining the area of the element. The area can be found by using Green's Theorem which can be stated as:

Assume there is a piecewise smooth simple closed curve, C, enclosing a region R. If M and N are continuous functions with continuous first partial derivatives in R then

$$\oint_C M dx + N dy = \iint_R \left(\frac{\partial N}{\partial x} - \frac{\partial M}{\partial y} \right) dA . \tag{3.1}$$

The formula for the area enclosed by C is

$$A = \oint_C x dy = -\oint_C y dx = \frac{1}{2} \oint_C x dy - y dx = \frac{1}{2} \sum_{i=0}^{n-1} x_i y_{i+1} - x_{i+1} y_i \tag{3.2}$$

where n is the number of nodes in the element and the n+1 node is the first node. The centroid or center of mass was found by

$$\bar{x} = \frac{\iint_R x dx dy}{A} = \frac{\mu_x}{A} \quad \text{and} \quad \bar{y} = \frac{\iint_R y dx dy}{A} = \frac{\mu_y}{A} \tag{3.3}$$

Green's theorem can be used to calculate the value of the numerator which results in

$$\mu_x = \frac{1}{2}\int_C x^2 dy = \frac{1}{6}\sum_{i=1}^{n+1}(x_{i+1} + x_i)(x_i y_{i+1} - x_{i+1} y_i) \tag{3.4}$$

and similarly for μ_y.

The integration points' locations were determined in the deformed element, and the distance between the centroid and each integration point's location is calculated and denoted w_i. This distance was used as a weight for that integration point's value, v_i, and the final value for the element was a weighted average and was calculated by

$$\text{average value} = \frac{\sum_i w_i v_i}{\sum_i w_i} \tag{3.5}$$

for every value at the integration points in the element.

The subroutine that called the material model update was changed so that any Abaqus (2009) user material update (umat) can be incorporated into our finite element program. A driver subroutine was written that accommodated the difference in the required data formats for our program and the Abaqus umat. The driver is capable of adjusting the size of storage arrays that are dependent on the material model. Once the umat returned with the updated material response, the driver then rearranged the values to the order required for the finite element program.

This section presented a brief overview of the computational efforts taken in this research. An alternate method of visualizing the finite element results was introduced. We also added the capability to use Abaqus user material updates in our finite element

program. The next section presents a study that investigates the effect of the two approximations made in the ALMR method that are not made in conventional FEM.

Error Analysis

Chapter II introduced a prescribed displacement field in the region of the crack tip and a weak form of compatibility between the patch and background mesh. In this section we qualitatively analyze the error incurred by using these approximations within a computational framework.

Qualitative Remote Stress Field Error Analysis

It is prudent to investigate the effect of the displacement field prescribed in the exclusion region and the patch-background compatibility on the finite element results. One such endeavor was to determine if these approximations had any effect on the far-field stress values, or that St. Venant's principle holds. St. Venant's principle (Saint-Venant, 1855) can be written as:

> the strains that can be produced in a body by the application, to a small part of its surface, of a system of forces statically equivalent to zero force and zero couple are of negligible magnitude at distances which are large compared with the linear dimensions of the part.(Love, 1927)

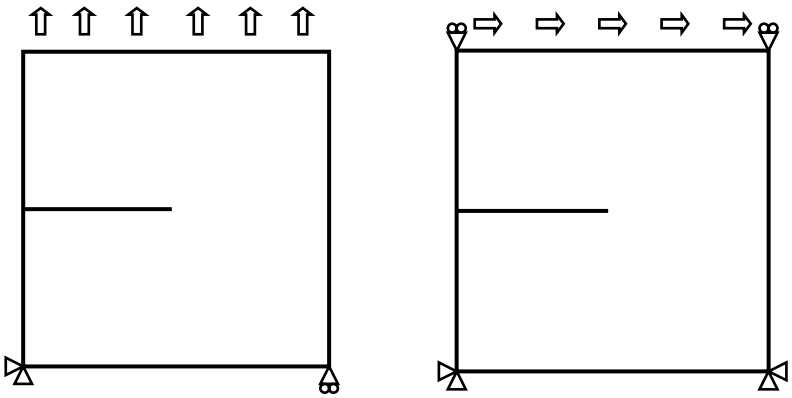

Figure 3.3 (a) Specimen and boundary conditions for tensile loading. (b) Specimen and boundary conditions for simple shear loading.

A rectangular block of dimension *b x b* where *b* equals 100 mm with an edge crack was used for this exercise as seen in Figure 3.3. There were also two types of loading. The first was a tensile loading that was applied by prescribing a displacement along the top surface shown in Figure 3.3(a). The second was a simple shear loading condition shown in Figure 3.3(b). The simulations were run until the onset of crack advance.

Two types of material behavior were chosen for this analysis. The first material response was linear elasticity. Young's modulus and Poisson's ratio were assigned 45 GPa and 0.35, respectively. The second material response was isotropic hardening. Young's modulus was the same as in the linear elastic behavior, but the yield stress was defined to be 123 MPa. The slope of the hardening portion of the response was 1500 MPa.

There must be a baseline simulation whose stress results can be used as a reference for comparison purposes. The reference simulation was the rectangular block with a crack explicitly defined in the geometry; i.e. no exclusion region present in the

simulation. Simulations including the exclusion region were run varying the radius from 0.05 mm to 0.30 mm.

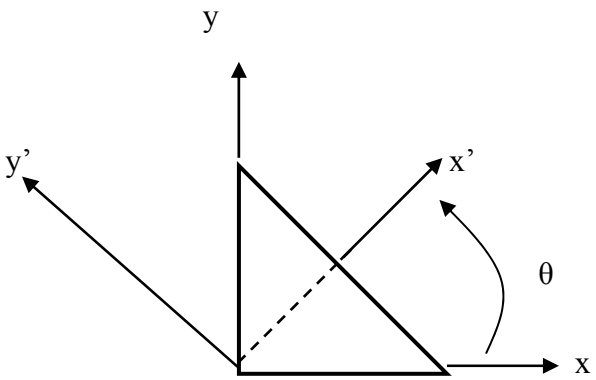

Figure 3.4 Body with a rotated coordinate system by angle θ.

The tangential stress values far away from the crack tip were chosen along a circular path centered on the crack tip. The first radius of the path, 25 mm, was chosen such that the there were no sharp gradients along the path. The second radius, 5 mm, was chosen to see if there were any effects closer to the crack tip. The tangential stress, σ'_{yy} in Figure 3.4, can be calculated using the stress tensor

$$\underline{\sigma} = \begin{bmatrix} \sigma_{xx} & \sigma_{xy} & \sigma_{xz} \\ \sigma_{xy} & \sigma_{yy} & \sigma_{yz} \\ \sigma_{zx} & \sigma_{zy} & \sigma_{zz} \end{bmatrix} \tag{3.6}$$

for the reference coordinate system and the angle θ for the new coordinate system. Defining the rotation matrix using the rotation in Figure 3.4, R, as

$$\underline{R} = \begin{bmatrix} \cos(\theta) & \sin(\theta) & 0 \\ -\sin(\theta) & \cos(\theta) & 0 \\ 0 & 0 & 1 \end{bmatrix}, \tag{3.7}$$

the stress tensor for the rotated coordinates can be found by

$$\underline{\sigma}' = R\sigma R^T . \tag{3.8}$$

The tangential stress in indicial notation is then

$$\sigma'_{yy} = R_{2j}\sigma_{jk}R_{2k} \tag{3.9}$$

or

$$\sigma'_{yy} = \sigma_{xx}\sin^2(\theta) + \sigma_{yy}\cos^2(\theta) - \sigma_{xy}[2\cos(\theta)\sin(\theta)]. \tag{3.10}$$

Thirty-six points evenly spaced along the circular path were chosen as places to calculate the tangential stress. This translated to one point for every ten degrees. For the simulations with an explicit crack in the geometry, the point on the path will most likely not coincide with an integration point in an element. A methodology needed to be chosen as a means of determining what stress value from the finite element mesh to use to calculate the tangential stress.

It is important to note that the described methodology is for specimens where the crack tip is located at the origin of the coordinate system. The first step was to determine which element contained the point on the path. After identifying the element containing the point, an averaged stress tensor for the element was calculated. The stress tensor was then used to calculate the tangential stress. Each step is described below.

The element corresponding to each point must be identified. The tangential stress values for the simulations including the exclusion region theory were easily calculated from the elements in the patch mesh. The number of wedges that make up each ring of the patch was chosen to be the same as the number of points where the tangential stress was to be calculated. Equal number of wedges and points allows the tangential stress to

be readily calculated from the stress values of the ring that coincides with the radius chosen.

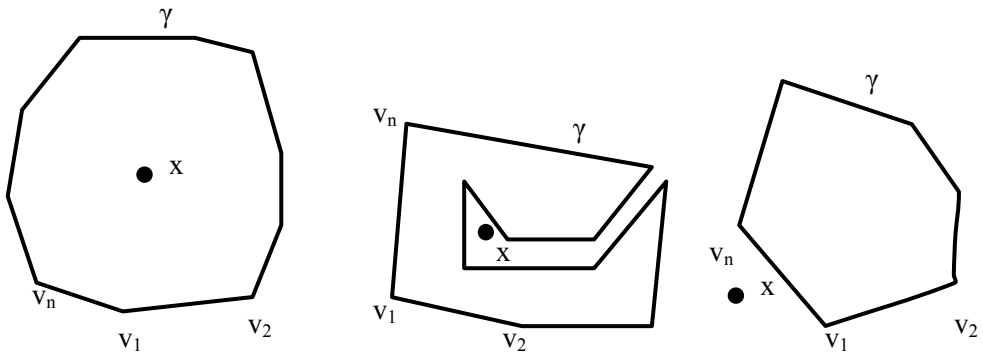

Figure 3.5 Possible paths around a point for winding number calculations.

The simulations without the exclusion region theory determined the element corresponding to the points of interest by using a winding number algorithm introduced by Alciatore and Miranda (1995). A winding number is a mathematical measure of the number of times a path or line winds around a point of interest and can be represented as

$$n(\gamma;x)=\begin{cases}0 & \text{if } x \notin \gamma \\ n>0 & \text{if } \gamma \text{ winds around } x \text{ counter - clockwise } n \text{ times} \\ n<0 & \text{if } \gamma \text{ winds around } x \text{ clockwise } n \text{ times}\end{cases} \tag{3.11}$$

where γ is a closed rectifiable path. It is frequently used in complex analysis evaluating integrals using Cauchy's Theorem and Integral Formula (Conway, 1978). Figure 3.5 shows several examples of how a path could surround a point. The magnitude of the winding number for the path about the point in the first scenario is 1 since the path wraps around the point once. For the second example the path goes around the point once in the counter-clockwise direction and once in the clockwise direction resulting in a winding

number of 0.0. The third example shows a point completely outside the area enclosed by the closed path resulting in a winding number of 0.0.

The winding number algorithm uses what is commonly referred to as an axis crossing method. An axis crossing method for a polygon determines if an edge of a polygon crosses the x-axis and in what direction, clockwise and counter-clockwise. If the system coordinates are translated such that the point of interest becomes the origin, then the axis crossing method result is the winding number. Special consideration needs to be taken in the event a vertex or an edge is on the x-axis of the translated coordinate system. In the case of the former, each edge would add 0.5 to the winding number resulting in increasing the winding number by one. The winding number should not be affected by the latter since the edge does not cross the x-axis. This particular algorithm does not take into account the point lying on the lines. Representing a polygon or element as a series of vertices $v_1, v_2, \ldots, v_p$, the pseudocode for the algorithm is as follows:

1. Translate the coordinate system so that the point of interest is the origin and the coordinates of the vertices of the element reflects this translation.

2. Initialize the winding number to zero.

3. Checking each edge, $v_i v_{i+1}$, for crossing the x-axis by working with the coordinates of the vertices.

    if the edge crosses the x-axis then calculate the coordinate where the edge crosses the x-axis, r.

        if the coordinate is positive then check the y-coordinate of vertex v_i.

the y-coordinate being negative indicates a counter-clockwise motion and positive indicates clockwise motion: increment the winding number for the particular motion

else if the edge lies on top of the positive x-axis then the winding number should not change

else if the vertex v_i lies on the positive x-axis then check to see if vertex v_{i+1} is above or below the x-axis and adjust the winding number by plus or minus one-half

else if the vertex v_{i+1} lies on the positive x-axis then check to see if vertex v_i is above or below the x-axis and adjust the winding number by plus or minus one-half

Consider that there are N points that we are trying to associate with an element and that there are P elements with L vertices each. Best case scenario is that for each point the first element searched is the one that actually contains the point. Worst case is that the element containing the point is the last element checked every time. It is improbable that the best case scenario would ever be realized so it would be fruitful to reduce the sample space of elements as much as possible to reduce the number of operations. The strategy adopted reduces the amount of elements checked for containing the point. Element centroids were calculated, and a search was done to determine if the centroid lies in an annular region of radius (r-ε, r+ε) where ε is appropriately defined with respect to the radius and the overall dimensions of the specimen. Once these elements are marked, the axis-crossing method is used to pair an element with the point in question.

The comparison of the tangential stress values at a distance of 25 mm are shown in Figures 3.6-3.9. The linear elastic material under tensile and simple shear loading is shown in Figure 3.6 and Figure 3.7. The linear isotropic hardening response under the two loading conditions is shown in Figure 3.8 and Figure 3.9, respectively. The tangential stress values show excellent agreement between the simulations with and without the exclusion region. The tangential stress values at a distance of 5 mm away from the crack tip behaved in the same way as the previously mentioned results with the exception that the stress values were higher due to being closer to the crack tip. It is evident that neither the approximate displacement field nor the weak form compatability along the patch-background intersection affect the far field stress values.

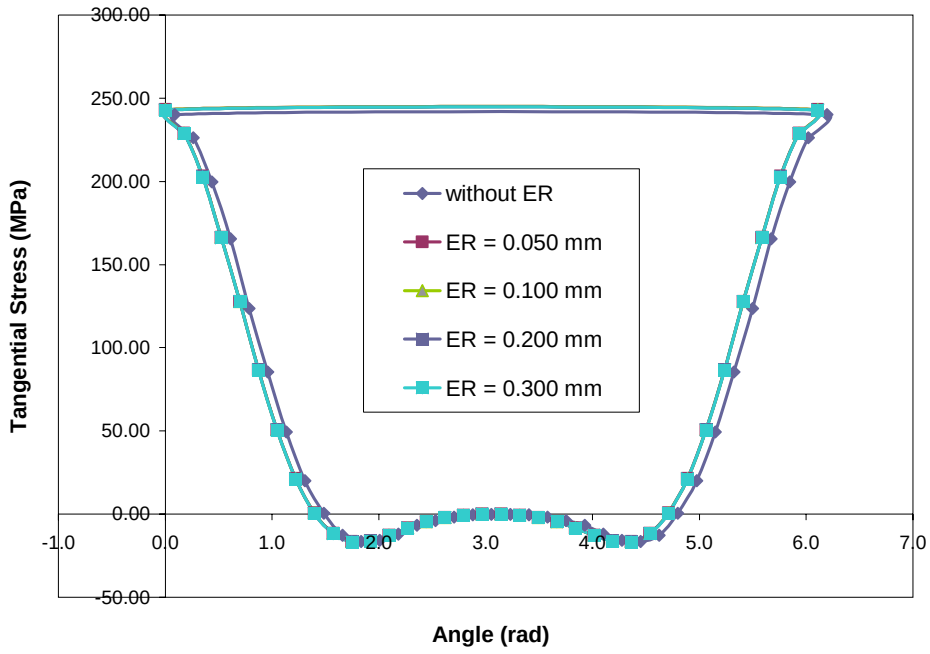

Figure 3.6 Tangential stress values along a circular path of radius 25 mm centered at the crack tip of tensile loading using a linear elastic material response.

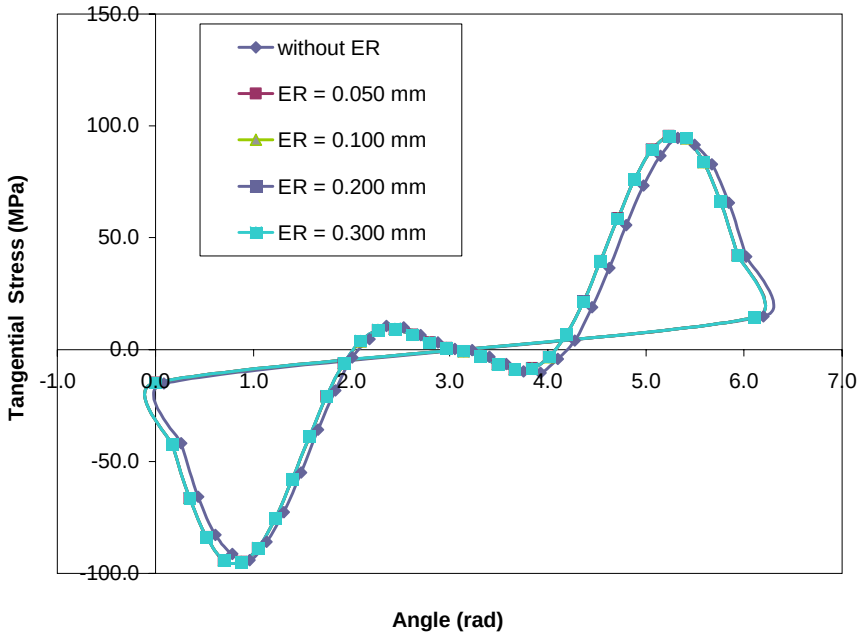

Figure 3.7 Tangential stress values along a circular path of radius 25 mm centered at the crack tip of simple shear loading using a linear elastic material response.

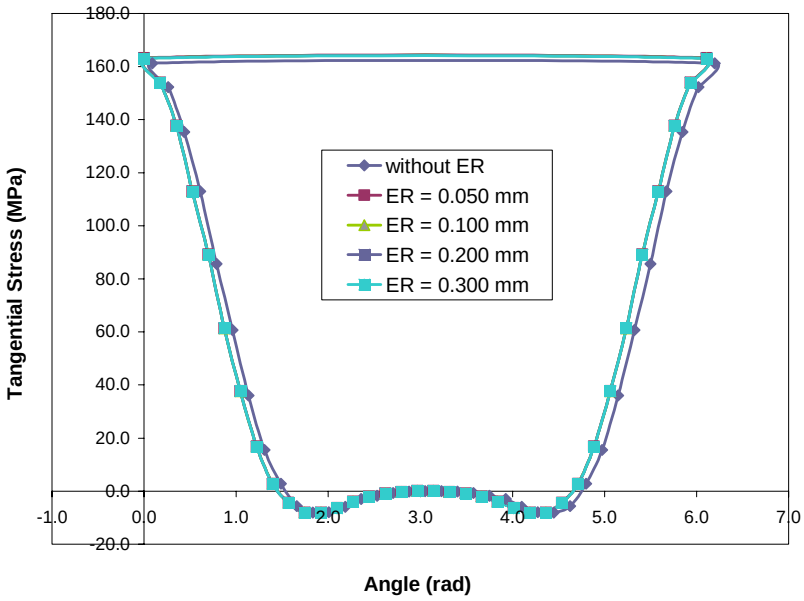

Figure 3.8 Tangential stress values along a circular path of radius 25 mm centered at the crack tip of tensile loading using a linear isotropic hardening material response.

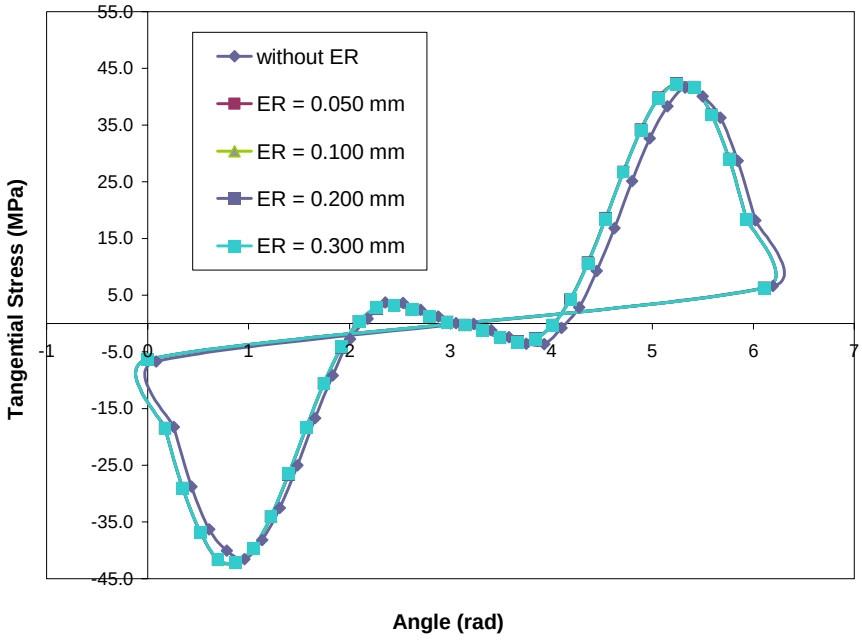

Figure 3.9 Tangential stress values along a circular path of radius 25 mm centered at the crack tip of simple shear loading using a linear isotropic hardening material response.

Displacement Field Error Analysis

It was shown that for various loading scenarios with different material behaviors that the exclusion region theory does not alter the stress field results. It has been previously shown that a relationship exists between the force-based separation criterion introduced in the exclusion region theory section from Chapter II and K_{Ic} for a linear elastic material (Rashid, 1997). It would be beneficial to see what effect the prescribed displacement field has on the displacements along the remainder of the crack surface. This section is aimed at determining this effect as well as again confirming the relationship between the K solution and the critical separation criterion value for a linear elastic material.

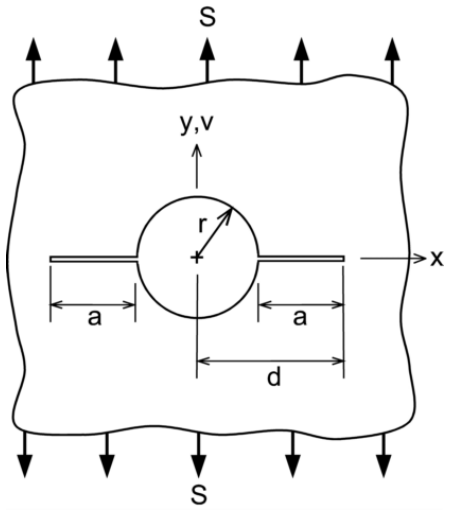

Figure 3.10 Infinite plate with two symmetric cracks emanating from a hole subjected to a remote stress.

The specimen used in this study is an infinite plate that has symmetric cracks emanating from a hole subjected to a remote uniform stress as shown in Figure 3.10. For two-symmetric cracks at a hole in a plate subjected to remote applied stress, the stress-intensity factor equation (Tada et. al, 2000) was obtained by fitting results from Newman (1971) as

$$K_h^S = K_\infty^S F_h^S = S\sqrt{\pi d}\ \ F_h^S \tag{3.12}$$

where K_∞^S is for a crack in an infinite plate without a hole and F_h^S is the boundary-correction factor for the circular hole. The equation for F_h^S is

$$F_h^S = \sqrt{1-\frac{r}{d}}\ \ f_2 \tag{3.13}$$

where

$$f_2 = 1.0 + 0.358\lambda + 1.425\lambda^2 - 1.578\lambda^3 + 2.156\lambda^4 \tag{3.14}$$

with λ = r/d for $0 \le \lambda \le 1$.

Exact crack-surface displacements for a crack in an infinite plate were obtained using Westergaard stress functions (Tada et. al, 2000). The displacement equation was then modified to approximately account for the hole (Newman, 1983). The displacement equation for a point x on the crack surface is

$$v_h^S = \frac{2(1-\eta^2)S}{E}\sqrt{d^2 - x^2}\ F_h^S. \tag{3.15}$$

It is not possible to simulate an infinite plate, but one can obtain a good approximation by increasing the dimensions with respect to the part of interest. For these simulations, the geometry is cut in half and the appropriate symmetry boundary conditions are applied to represent the infinite plate (Figure 3.11). The dimensions of the plate modeled, shown in Figure 3.11, were chosen such that they were at least twenty-five times larger than the radius of the circle. Both the length of crack emanating from the hole and the radius of the circle were chosen to be 1 mm. The width of the plate, W, was chosen to 25 mm; large enough such that the boundary would not affect the solution.

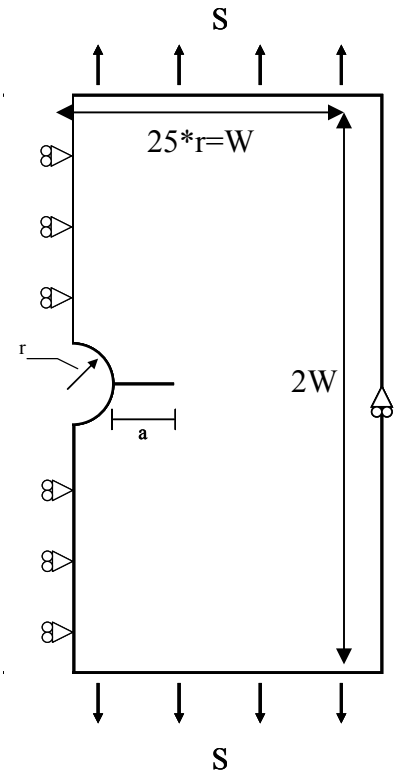

Figure 3.11 The geometry modeled in the finite element simulation in FEFRAC with a remote stress S, hole of radius r, and crack of length a.

This study assumes that the material behaves linear elastically. The material constants used were a Young's modulus of 45 GPa and a Poisson's ratio of 0.35 which are representative of a magnesium alloy. K_{Ic} was chosen to be 17.3 MPa√m or 547.07 MPa√mm also indicative of a magnesium alloy.

It has been noted that

$$K_I \approx \Phi\sqrt{b} \tag{3.16}$$

where b is the exclusion region radius and Φ is the force-based separation function value for linear elasticity (Rashid, 1997a). The equivalence between SIF and separation function value, equation (3.16), indicates that the critical separation function value, Φ_c, should take the values in Table 3.1 for the different exclusion region radius.

Table 3.1 Critical separation values for the different radii of the exclusion region.

Exclusion Region Radius	Φ_c
0.0125 mm	4893.2
0.0250 mm	3460.0
0.0500 mm	2446.6
0.1000 mm	1780.0

Gathering from the stress intensity factor equation for the geometry in Figure 3.10

$$K_h^S = K_\infty^S F_h^S = S\sqrt{\pi d}\ \ F_h^S \tag{3.17}$$

the critical applied stress, S_c, is of the form

$$S_c = \frac{K_{h\,c}^S}{\sqrt{\pi d}\ \ F_h^S}, \tag{3.18}$$

and the critical value of the stress intensity factor or fracture toughness, K_{Ic}, as it is more commonly called is

$$K_{h\,c}^S = S_c\sqrt{\pi d}\cdot F_h^S = K_{Ic}\,. \tag{3.19}$$

The critical applied stress is defined as the stress that causes K_I=K_{Ic}, which causes failure. Given the K_{Ic} value above, the remote stress that should cause failure can be calculated from equation (3.18) and is 209.6 MPa.

Nondimensional values of the critical applied stress were determined using

$$\bar{S}_c = \frac{S_c\sqrt{r}}{K_{h\,c}^S} = \frac{1}{F_h^S}\sqrt{\frac{\lambda}{\pi}}\,. \tag{3.20}$$

The final expression of equation (3.20) was used for the non-dimensional analytical critical applied stress. The middle expression in equation (3.20)

$$\bar{S}_c = \frac{S_c\sqrt{r}}{K_{Ic}} \tag{3.21}$$

was used in conjunction with the finite element solution where S_c is the remote stress applied that caused the crack to advance. Nondimemsional values for both the semi-analytical displacements and the finite element results were obtained by the expression

$$\frac{E'v}{S\,a} \tag{3.22}$$

where a is the length of the crack measured from the edge of the hole to the crack tip, v is the displacement of a point in the vertical direction, S is the applied remote stress, and E' is

$$E' = \frac{E}{1-\eta^2} \tag{3.23}$$

where η is Poisson's ratio.

The comparison of the normalized critical applied stress for various exclusion radii and the analytical solution (Eqn. 3.18) are shown in Figure 3.12. The figure showed that most of the computations were within $\pm$ 2 percent and at worst under 10 percent for this particular geometry. The normalized crack surface displacements from the finite element simulations and the displacements from the semi-analytical solution in Newman (1971), equation (3.15), are shown in Figure 3.13. The displacements overall have an excellent agreement with the semi-analytical solution. Several conclusions can be made from Figure 3.13. The first is that all of the results coincide with each other except those of the 0.1 radii. Secondly, the displacement results diverge from the published displacement field where the crack meets the hole. The divergence needs to be further investigated and the investigation is presented in the next chapter.

The normalized critical applied stresses (Eqn. 3.21) that caused fracture are within a few percent of the accepted K-solutions for the geometry. The displacements from the

finite element simulations deviate from existing semi-analytical solution as one moves away from the crack tip. The next chapter of this dissertation addresses the deviation shown in the crack surface displacements for the geometry above as well as the scenario where part of the crack surface is loaded. The two loading conditions were chosen because accurate displacements for these loading situations are a necessity for fatigue modeling. The next chapter will in fact show that the difference between the finite element displacement results and the semi-analytical displacement is not an artifact of the finite element simulation. The next subsection's goal is to find an appropriate exclusion region radius when plasticity is introduced.

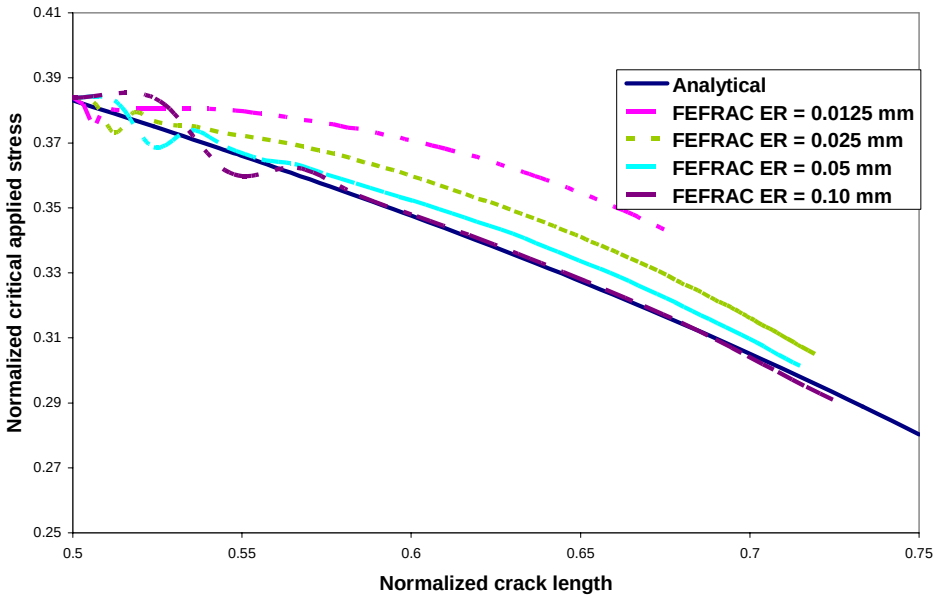

Figure 3.12 Comparison of the normalized critical applied stress versus normalized crack length results from the analytical and finite element solutions varying the radii of the exclusion region.

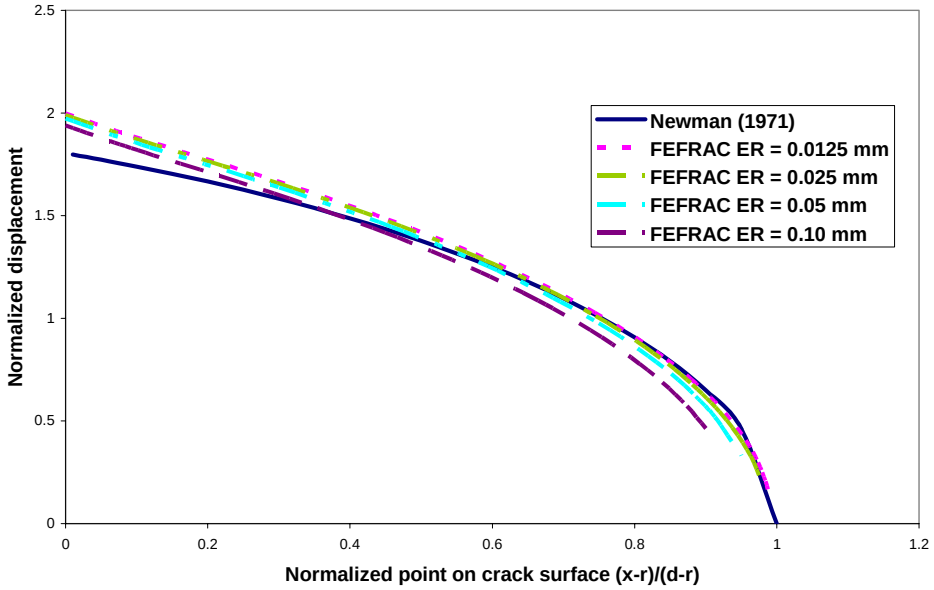

Figure 3.13 Comparison of the semi-analytical displacement equation (eqn.3.2) with the normalized crack surface displacements from the finite element simulations varying the radii of the exclusion region.

Determination of suitable Exclusion Region radius with plasticity

It has been shown in the previous sections that the exclusion region theory yields the same results as conventional finite element solutions for linear elastic material. Rashid (1997a) showed and it was repeated in the previous section that there is a direction relationship between the exclusion region theory using a force-based separation criterion and the stress intensity factor approach, assuming the radius of the exclusion region is less that three percent of the crack length. This section's purpose is to investigate the effect of the radius on simulation results when plasticity is introduced into the material behavior.

The specimen used in this investigation is an infinite plate containing cracks emanating from a circular hole subjected to remote loading as shown in the last section.

The analytical solution used in this section for crack surface displacements is determined in the next chapter.

The outline of this investigation is as follows. First, a benchmark solution/method must be found. The benchmark for this study will be simulating the specimen above using the commercial code, Abaqus. Once it is shown that Abaqus produces the exact solution for the linear elastic case, it will be assumed that Abaqus continues to give accurate results once plasticity is introduced. Using a plasticity model in Abaqus, results for stress and crack-surface displacements will be used to judge the accuracy of the results of the exclusion region theory, will indicate the effect the radius of the exclusion region has on the simulation results, and should offer guidelines as to the suggested size of the exclusion region with plasticity.

The geometry for all the simulations using the exclusion region theory, Figure 3.11, is a half-model of the specimen in Figure 3.10. The material constants were Young's modulus of 45 GPa and a Poisson's ratio of 0.35. For the isotropic hardening model, the additional constants that need to be prescribed are the yield stress which is 123 MPa and the slope of the hardening curve which is 1500 MPa. These constants are representative of a magnesium alloy. For linear elasticity, the remote stress was ramped to a value of 210.0 MPa, while for the isotropic hardening case the loading was ramped to a value of 126.0 MPa. The simulations were run assuming plane strain conditions and using quadrilateral elements with four integration points.

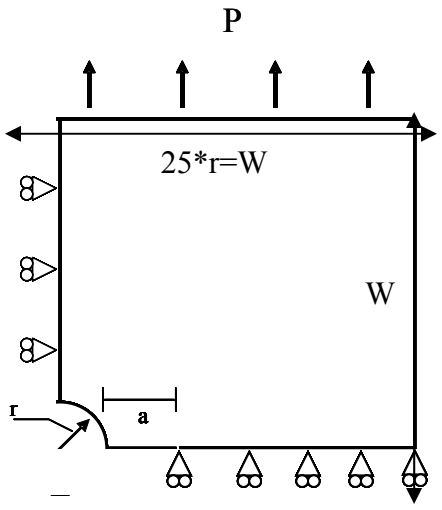

Figure 3.14 Quarter geometry used to simulate specimen with Abaqus where the radius of the circle is *r* and the length of the crack is a.

The geometry for the simulations using Abaqus required the used of a quarter geometry shown in Figure 3.14. The top row of elements where the load was to be applied was used to create a surface. A pressure equivalent to the stress in the half geometry was applied to that surface. The bottom boundary in the quarter geometry is on rollers except for the part that acts as the crack surface. The Abaqus simulations used plane strain elements with four integration points per element.

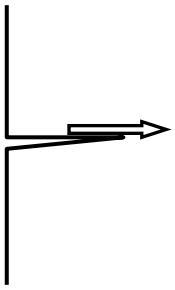

Figure 3.15 Cracked geometry showing the ray that was used as a path for comparison of stresses from elements for the plots in Figures 3.17, 3.18, 3.26, and 3.27.

The values for crack surface displacement were taken from the nodes on the crack surface. The stress components were taken from the elements along a ray emanating from the crack tip as shown in Figure 3.15. The analytical axial stress shown in Figure 3.17 is calculated by using the first term in the Taylor series expansion and is

$$\sigma_{yy} = \frac{K_I}{\sqrt{2\pi r_e}} \cos\left(\frac{\theta}{2}\right)\left[1 + \sin\left(\frac{\theta}{2}\right)\sin\left(\frac{3\theta}{2}\right)\right] \tag{3.24}$$

where

$$K_I = K_\infty^S F_h^S = S\sqrt{\pi d}\ F_h^S \tag{3.25}$$

, r_e is the distance from the element's centroid to the crack tip, and K_∞^S is for a crack in an infinite plate without a hole and F_h^S is the boundary-correction factor for the circular hole. The equation for F_h^S is

$$F_h^S = \sqrt{1 - \frac{r}{d}}\ f_2 \tag{3.26}$$

where

$$f_2 = 1.0 + 0.358\lambda + 1.425\lambda^2 - 1.578\lambda^3 + 2.156\lambda^4 \tag{3.27}$$

with $\lambda = r/d$ for $0 \le \lambda \le 1$.

The linear elastic simulations served to verify first that Abaqus gives the correct results, and secondly that the exclusion region results were also in agreement assuming the conditions on the exclusion region radius proposed by Rashid (1997) were maintained. Figure 3.16 shows the crack surface displacements for the linear elastic simulations in FEFRAC and Abaqus. The comparison shows that as the exclusion region radius decreased the displacements converged to the new analytical solution proposed in

the next chapter of this work. The effect of the radius on displacements for radii less than five percent of the crack length extends about two radii beyond the boundary of the region. Displacement results from points about two radii away from the exclusion region show good agreement with the new displacement solution. Figure 3.17 shows the axial stress component of the stress tensor for the ray in Figure 3.15. The axial stress component was chosen due to it being the largest component of the stress tensor. The results show that the radius of one percent of the crack length is the only one where the maximum stress agrees with the Abaqus results. The maximum for the .01 radius simulation actually occurred behind the crack tip and this was a result of taking the locations on the crack surface from the deformed configuration. The plateaus for each exclusion region are the result of the prescribed displacement field within the exclusion region. The Abaqus and FEFRAC results also have the same general behavior as the first term of the Taylor series approximation.

The deviatoric stress component value was also investigated. The first term of the Taylor series expansion of the deviatoric stress is

$$\tau_{xy} = \frac{K_I}{\sqrt{2\pi r_e}} \cos\left(\frac{\theta}{2}\right) \sin\left(\frac{\theta}{2}\right) \cos\left(\frac{3\theta}{2}\right) \tag{3.28}$$

and is plotted as the analytical solution. It can be concluded from the previously two mentioned plots that the smallest and largest exclusion region simulations serve as the upper and lower bound of the results. Thus for the deviatoric component, only these two were shown for viewing ease in Figure 3.18 since there was little variation in the values. One can see that the trends are the same, but the maximum and minimum values differ. This is believed to be a result of the prescribed displacement in the exclusion region.

To get a general feel of the agreement between FEFRAC and Abaqus, contour plots for all the simulations run are presented. All values were calculated based on the centroid of the element. The von Mises stress is shown in Figures 3.19-3.24. The scale is the same for the plots allowing a qualitative comparison to take place. The maximum value for the scale bar was chosen by selecting a value a small distance away from the exclusion region boundary in the largest radius simulation. This was done in an attempt to show the global behavior since the maximum values of the output values are going to occur on the boundary of the exclusion region. The stress fields are further evidence verifying that Abaqus and FEFRAC simulations show excellent agreement. Also, it has been shown for the linear elastic case that the exclusion region theory's implementation can match accepted crack surface displacements that will be shown in the next chapter.

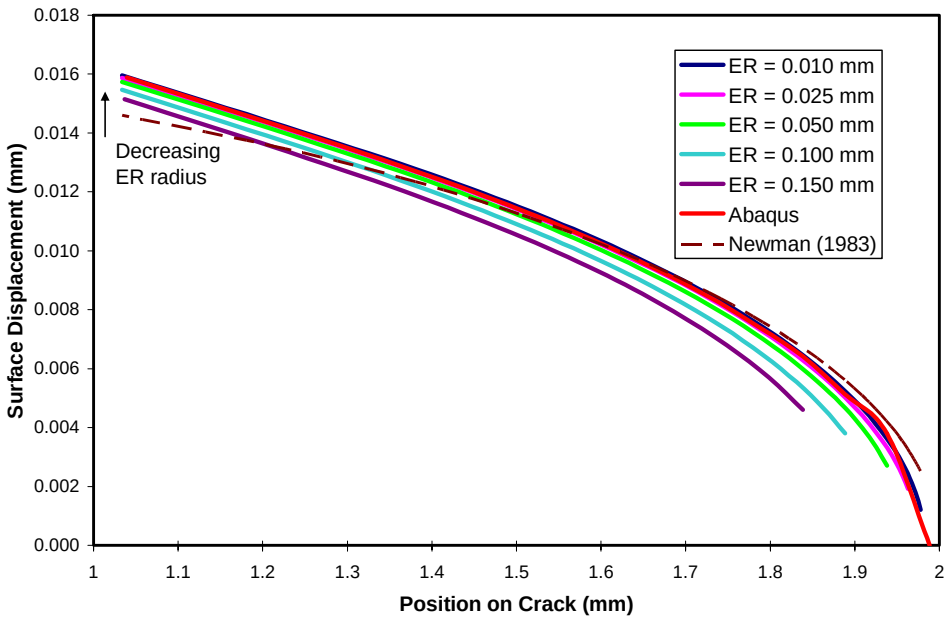

Figure 3.16 Crack surface displacement comparison between Abaqus, analytical solutions, and exclusion region finite element simulations.

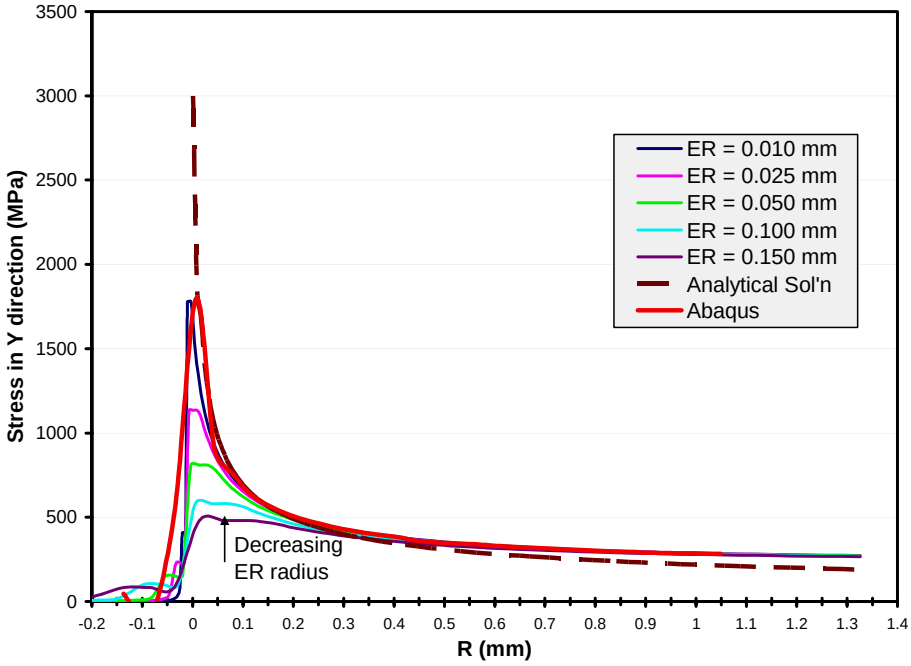

Figure 3.17 Axial stress comparison between Abaqus, analytical solutions, and exclusion region finite element simulations.

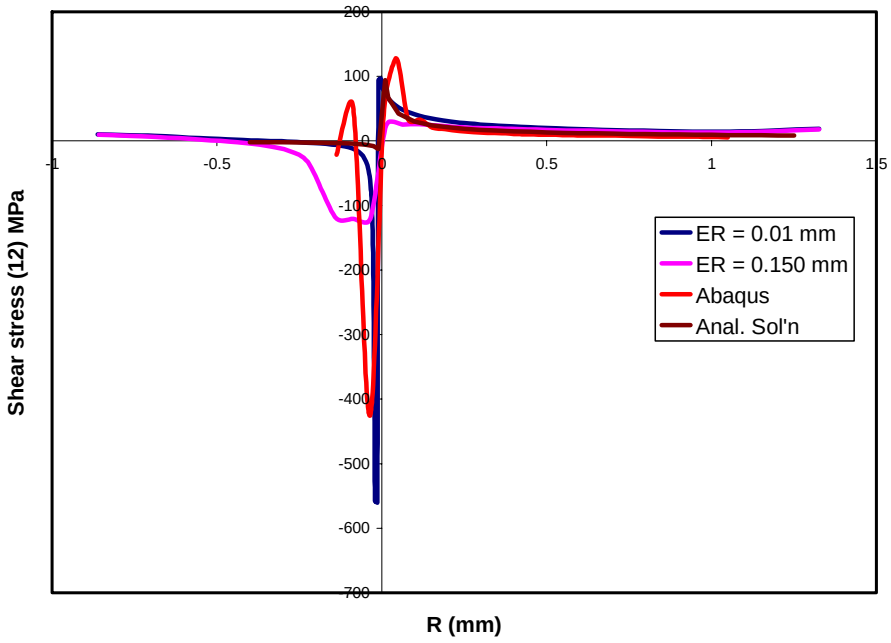

Figure 3.18 Shear stress comparison between Abaqus, analytical solutions, and exclusion region finite element simulations.

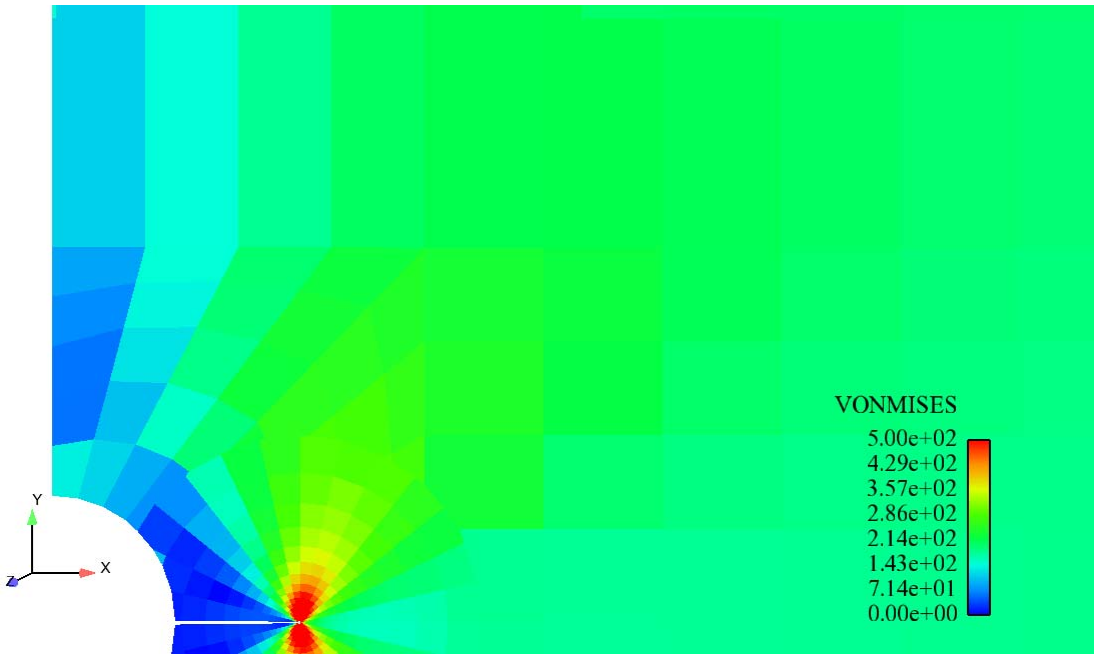

Figure 3.19 Von Mises stress field of a linear elastic material simulation in FEFRAC with ER = 0.01 mm where the radius and crack have length of 1.0 mm.

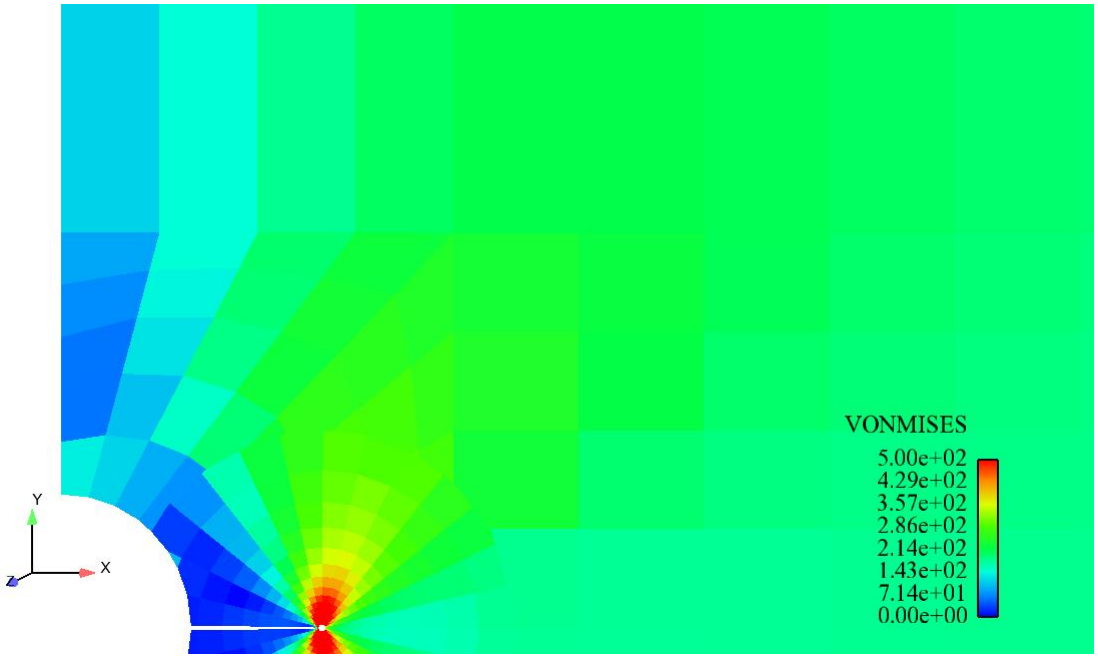

Figure 3.20 Von Mises stress field of a linear elastic material simulation in FEFRAC with ER = 0.025 mm where the radius and crack have length of 1.0 mm.

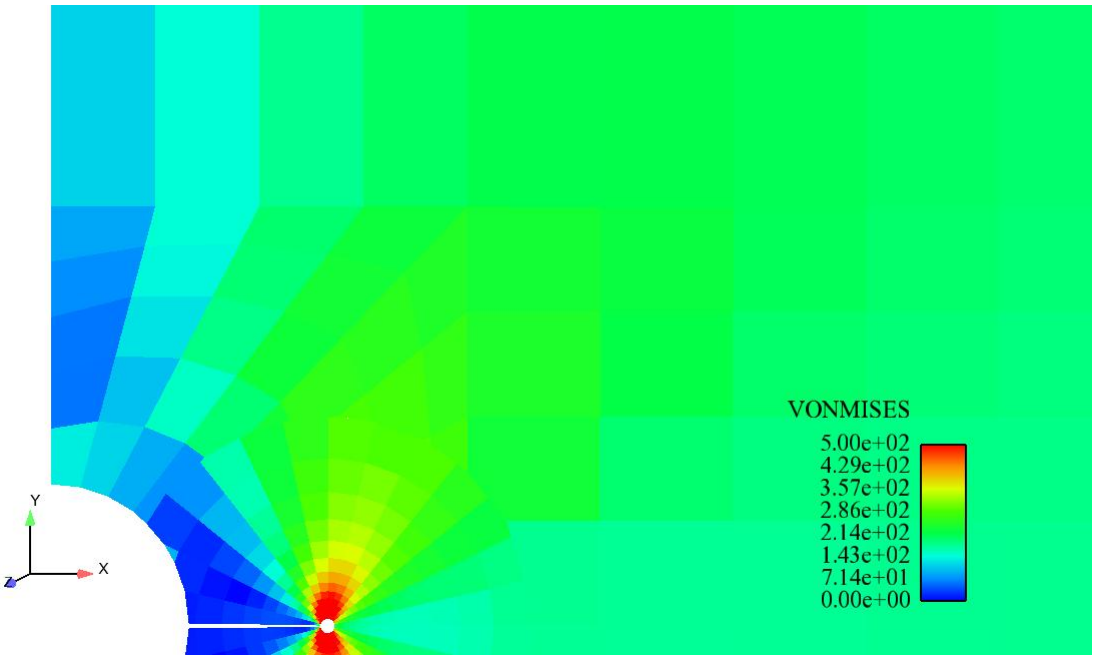

Figure 3.21 Von Mises stress field of a linear elastic material simulation in FEFRAC with ER = 0.05 mm where the radius and crack have length of 1.0 mm.

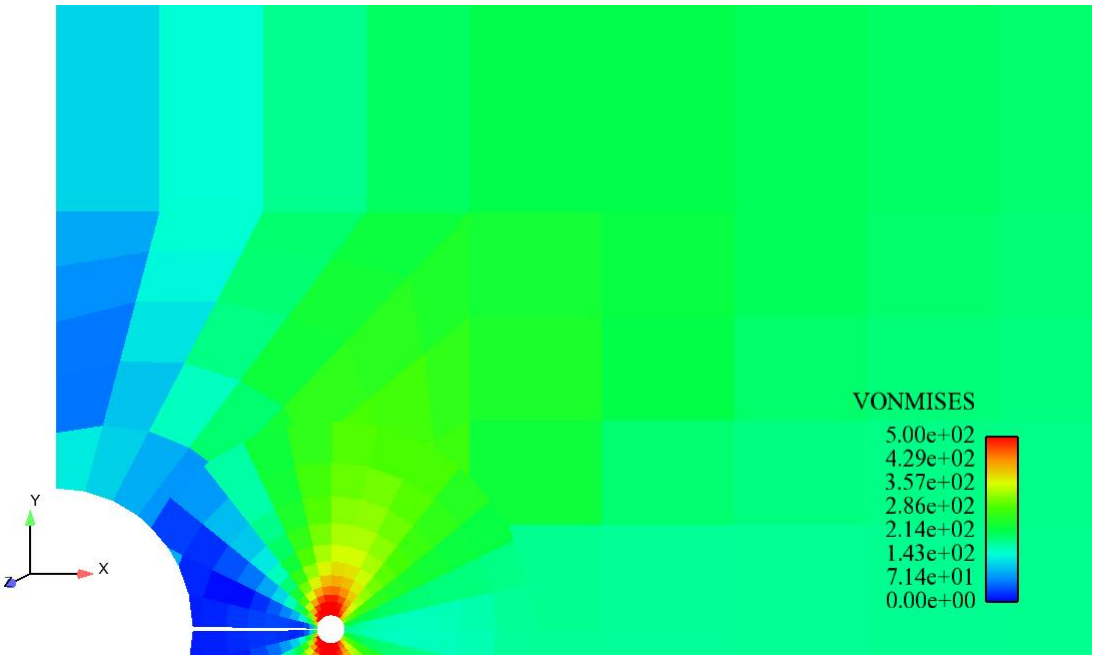

Figure 3.22 Von Mises stress field of a linear elastic material simulation in FEFRAC with ER = 0.10 mm where the radius and crack have length of 1.0 mm.

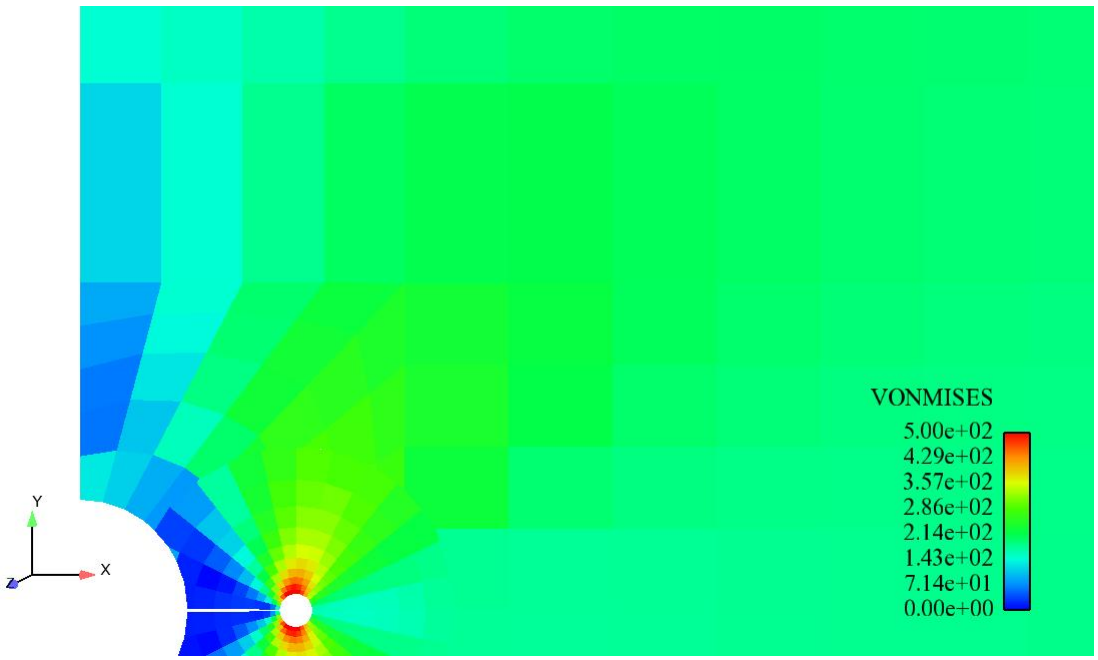

Figure 3.23 Von Mises stress field of a linear elastic material simulation in FEFRAC with ER = 0.15 mm where the radius and crack have length of 1.0 mm.

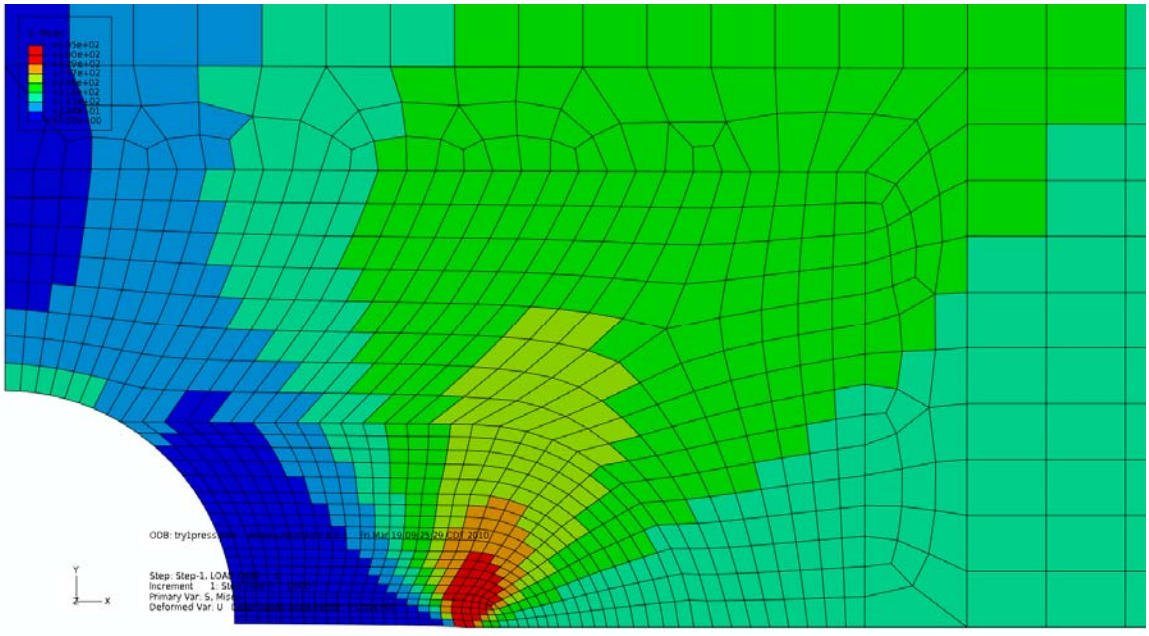

Figure 3.24 Von Mises stress field of a linear elastic material simulation in Abaqus where the radius and crack have length of 1.0 mm.

Now that it has been shown that Abaqus gives what are believed to be accurate results in the linear elastic case, we assumed that when plasticity is introduced that Abaqus will continue to give reliable results and acts as a measure to compare our results from FEFRAC. For the plasticity portion, only linear isotropic hardening was considered.

The crack surface displacements in Figure 3.25 show relatively good agreement with the Abaqus solution. The trend where the exclusion region solution converged to the Abaqus solution from the linear elastic case was present as would be expected. The axial stress results in Figure 3.26 for the exclusion region of 0.01 agree with the Abaqus axial stress values. The behavior of the shear stress component shown in Figure 3.27 is consistent with the Abaqus solution with the exception that Abaqus has more oscillations near the crack tip.

Since these results are only for one particular ray originating at the crack tip and that it is not realistic to plot results for multiple rays originating from the crack tip, it must suffice to look at the contour plots of several output variables. The variables shown are the von Mises stress, the axial stress component, and the effective plastic strain. All plots are showing the value at the centroid of the elements. The scale bar was set in the same fashion as described in the linear elastic section. The von Mises stress plots, Figures 3.28-3.32, from the exclusion region simulations show that the overall trends of the shape agree with the contour plot from Abaqus, Figure 3.33. Similarly for the effective plastic strain plots, Figures 3.34-3.38, and for the axial stress plots, Figures

3.40-3.44, the exclusion region results have the same behavior as the Abaqus simulations in Figures 3.39 and 3.45, respectively.

From Figures 3.25-3.27, it can be concluded then that the exclusion region theory does give reliable results for crack-surface displacements and stress field values in the presence of plasticity provided that the exclusion region is less than five percent of the crack length.

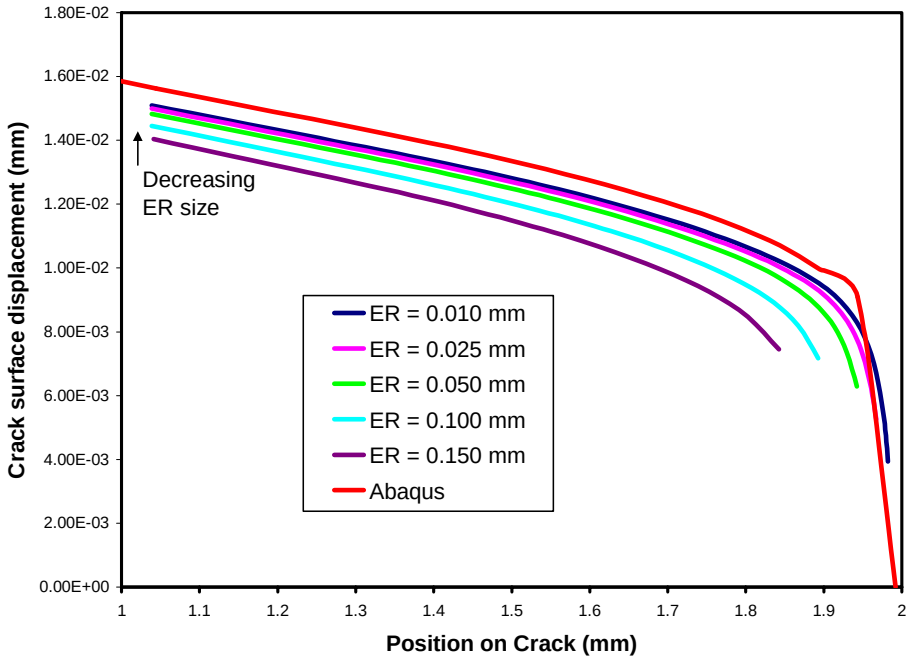

Figure 3.25 Crack surface displacement comparison between Abaqus, analytical solutions, and exclusion region finite element simulations for an isotropic hardening material.

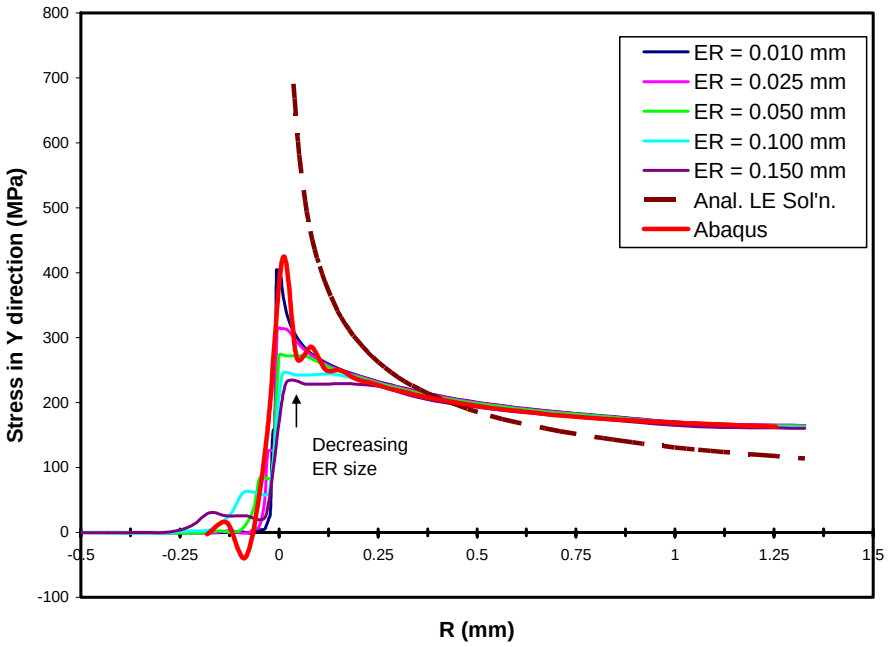

Figure 3.26 Axial stress comparison between Abaqus, analytical solutions, and exclusion region finite element simulations for an isotropic hardening material.

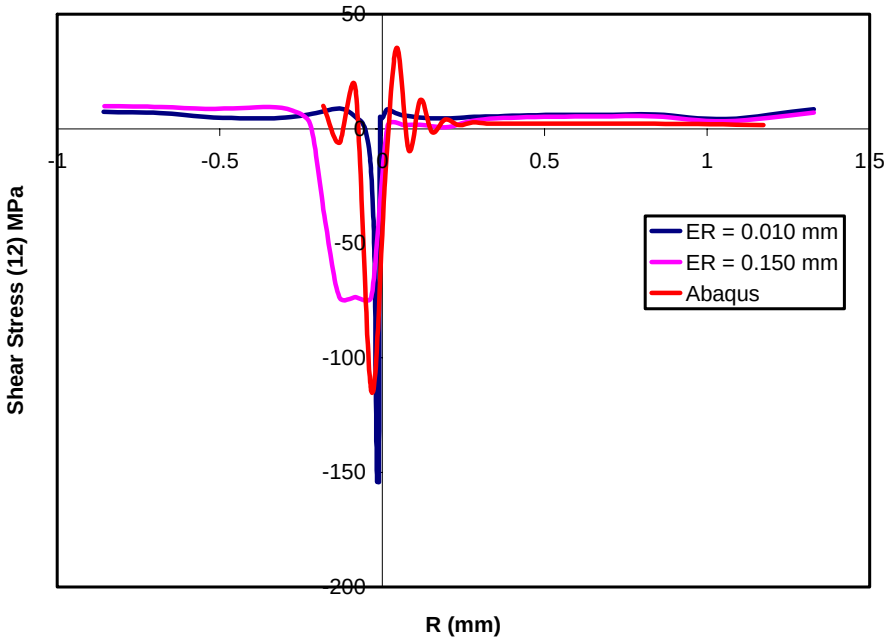

Figure 3.27 Shear stress comparison between Abaqus, analytical solutions, and exclusion region finite element simulations for an isotropic hardening material.

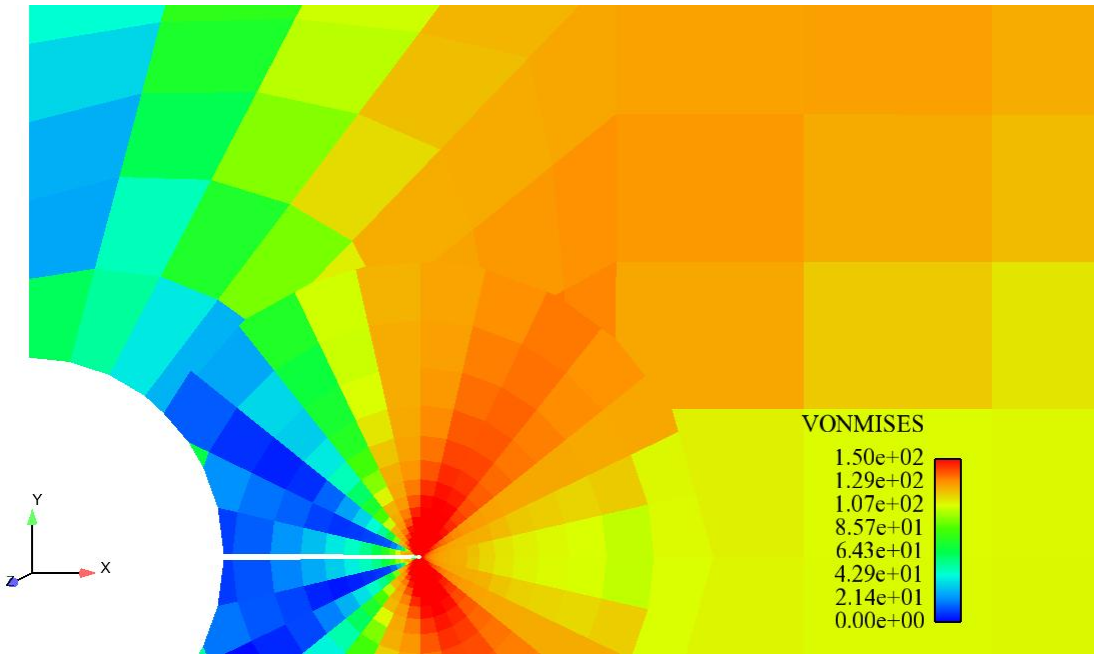

Figure 3.28 Von Mises stress field of an isotropic material simulation in FEFRAC with ER = 0.01 mm where the radius and crack have length of 1.0 mm.

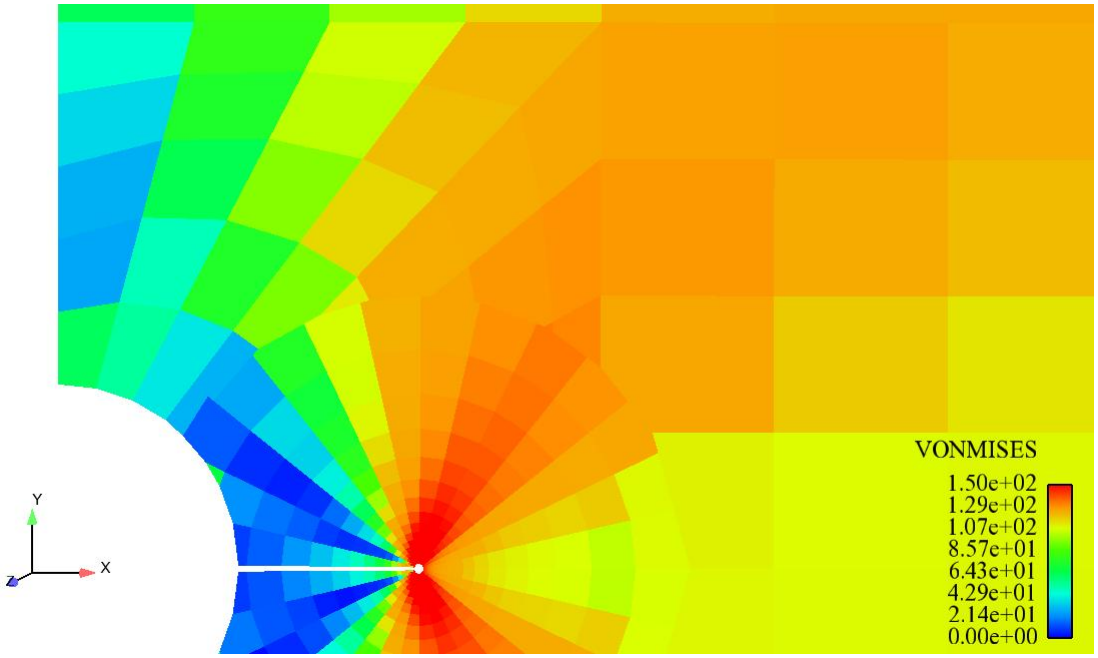

Figure 3.29 Von Mises stress field of an isotropic material simulation in FEFRAC with ER = 0.025 mm where the radius and crack have length of 1.0 mm.

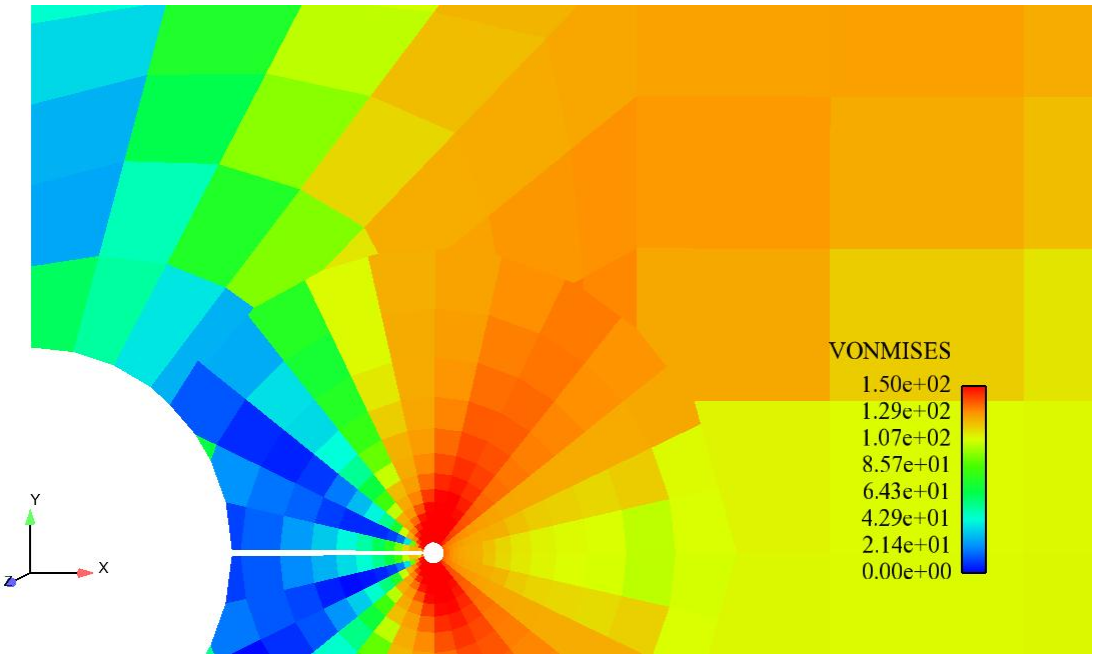

Figure 3.30 Von Mises stress field of an isotropic material simulation in FEFRAC with ER = 0.05 mm where the radius and crack have length of 1.0 mm.

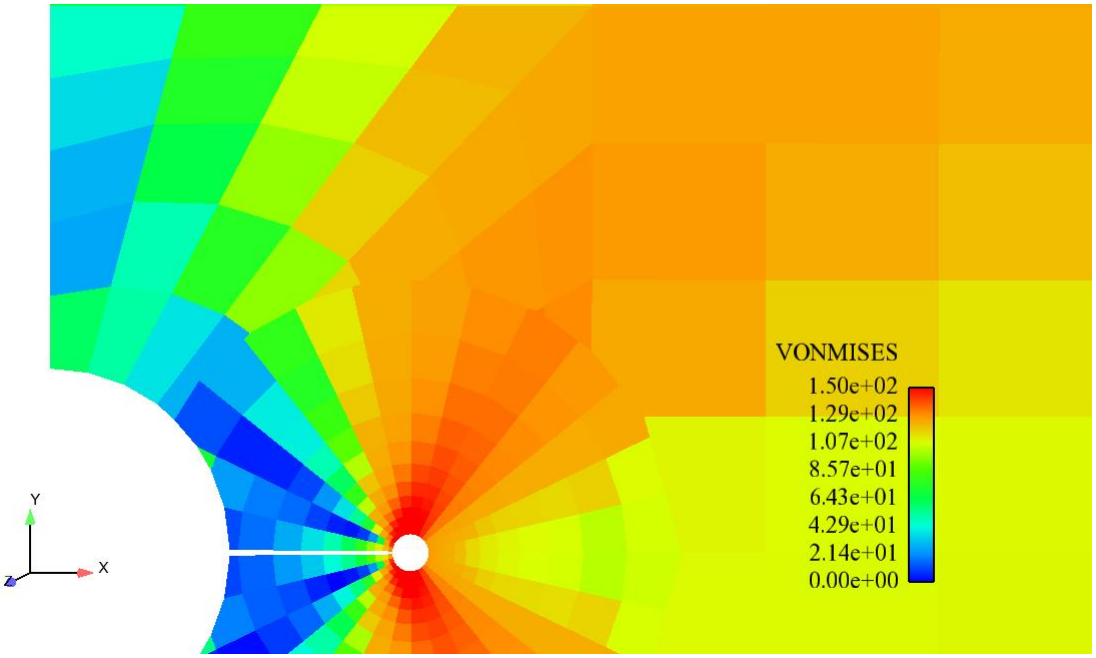

Figure 3.31 Von Mises stress field of an isotropic material simulation in FEFRAC with ER = 0.1 mm where the radius and crack have length of 1.0 mm.

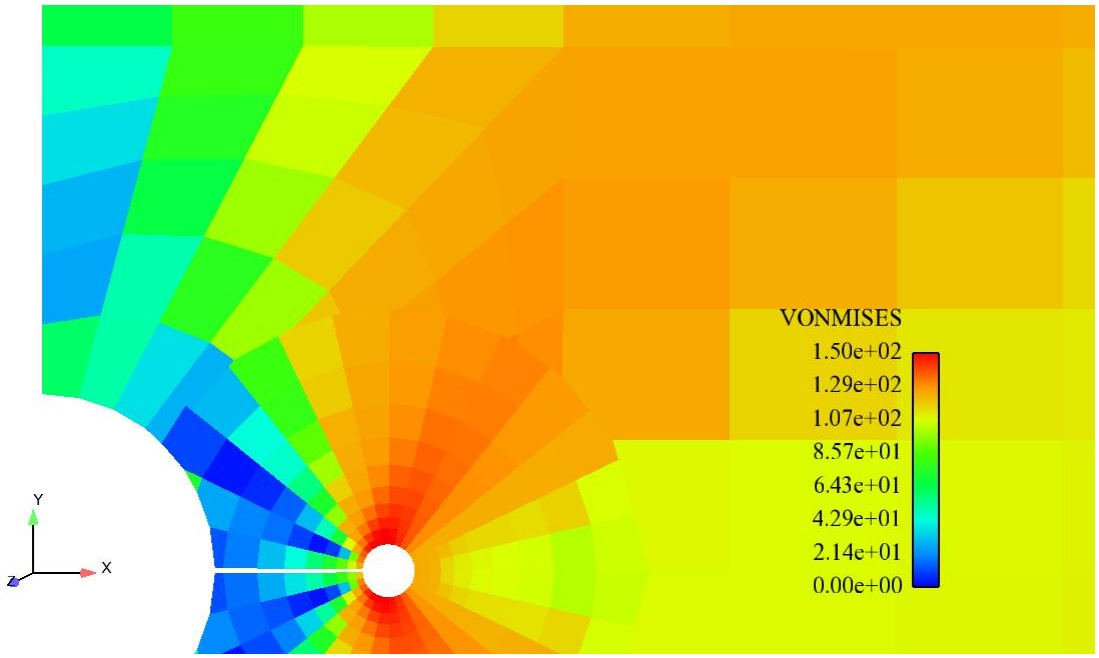

Figure 3.32 Von Mises stress field of an isotropic material simulation in FEFRAC with ER = 0.15 mm where the radius and crack have length of 1.0 mm.

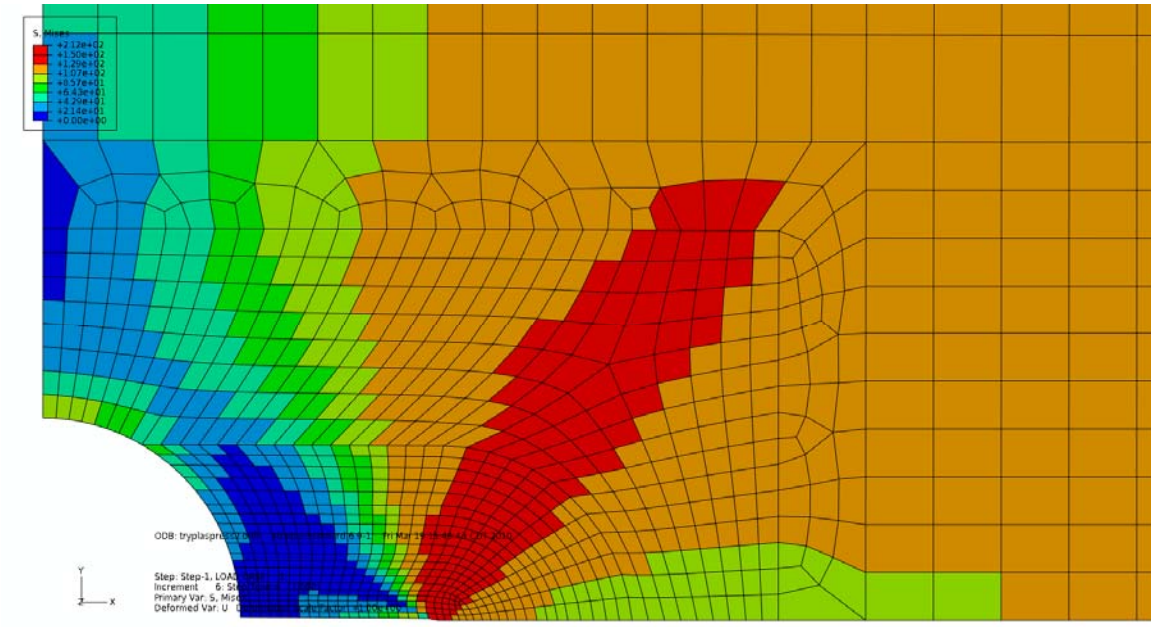

Figure 3.33 Von Mises stress field of an isotropic material simulation in Abaqus where the radius and crack have length of 1.0 mm.

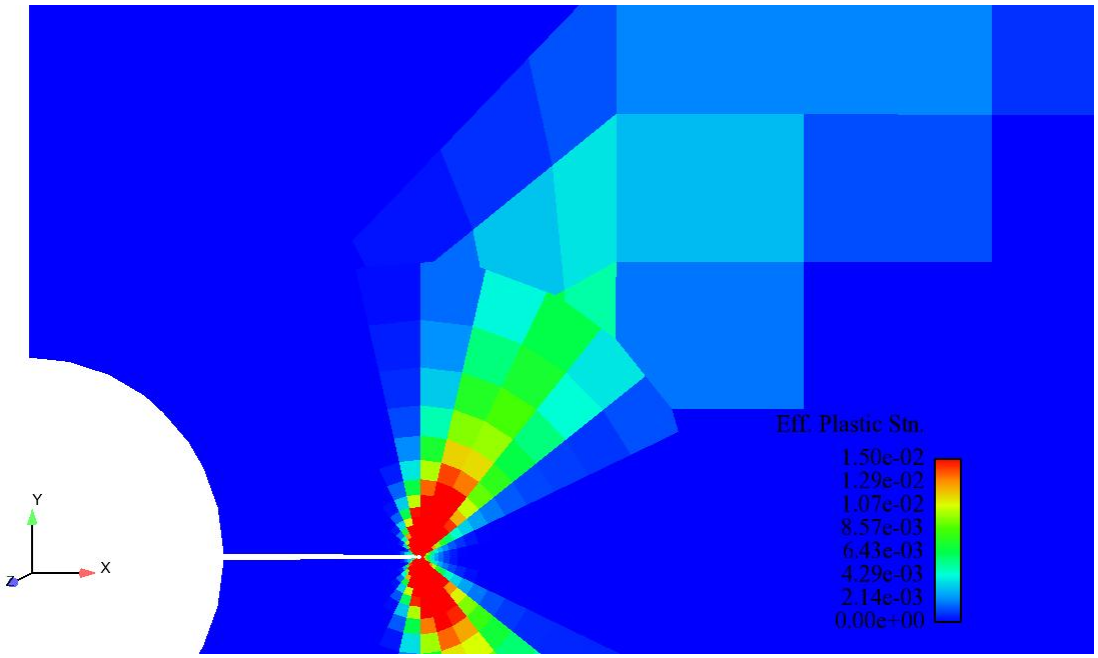

Figure 3.34 Effective plastic strain of an isotropic material simulation in FEFRAC with ER = 0.01 mm where the radius and crack have length of 1.0 mm.

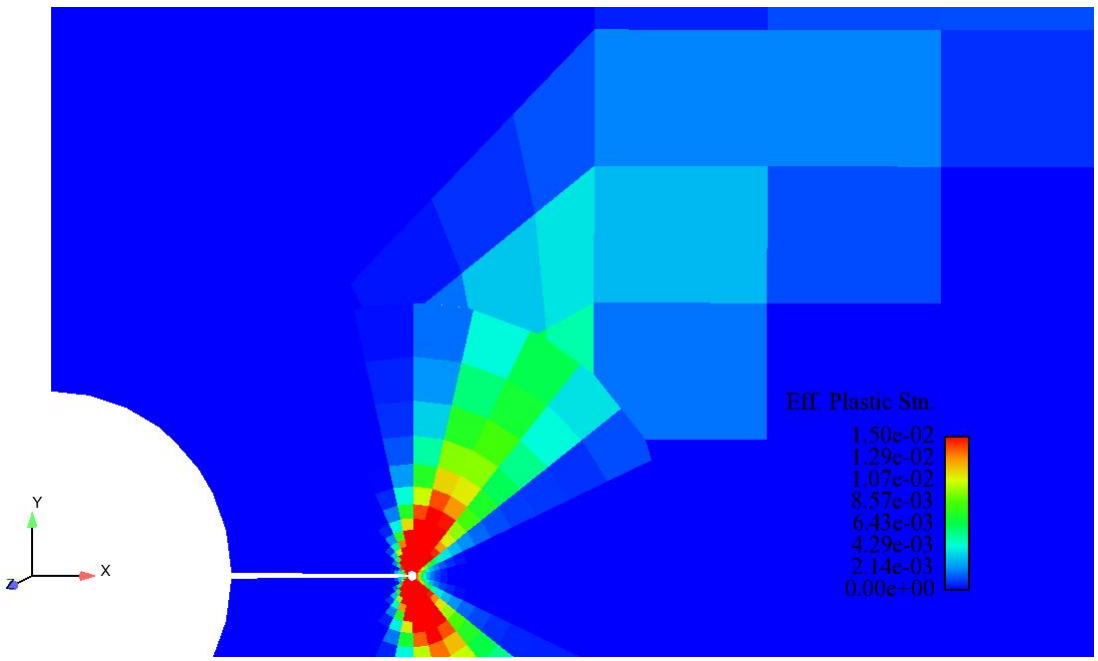

Figure 3.35 Effective plastic strain of an isotropic material simulation in FEFRAC with ER = 0.025 mm where the radius and crack have length of 1.0 mm.

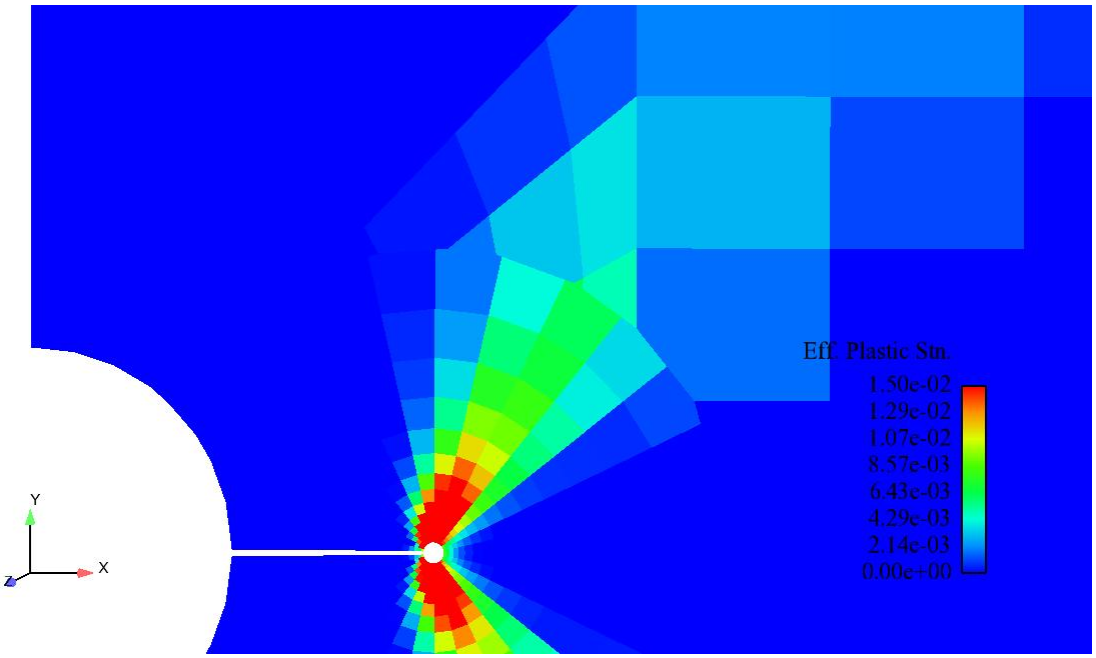

Figure 3.36 Effective plastic strain of an isotropic material simulation in FEFRAC with ER = 0.05 mm where the radius and crack have length of 1.0 mm.

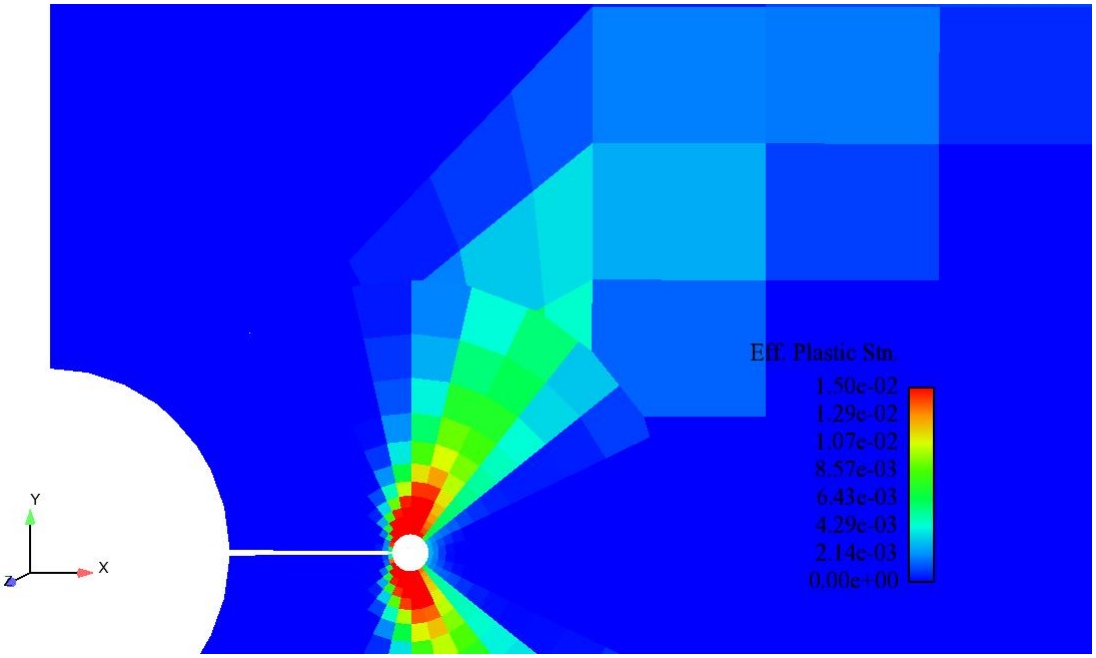

Figure 3.37 Effective plastic strain of an isotropic material simulation in FEFRAC with ER = 0.1 mm where the radius and crack have length of 1.0 mm.

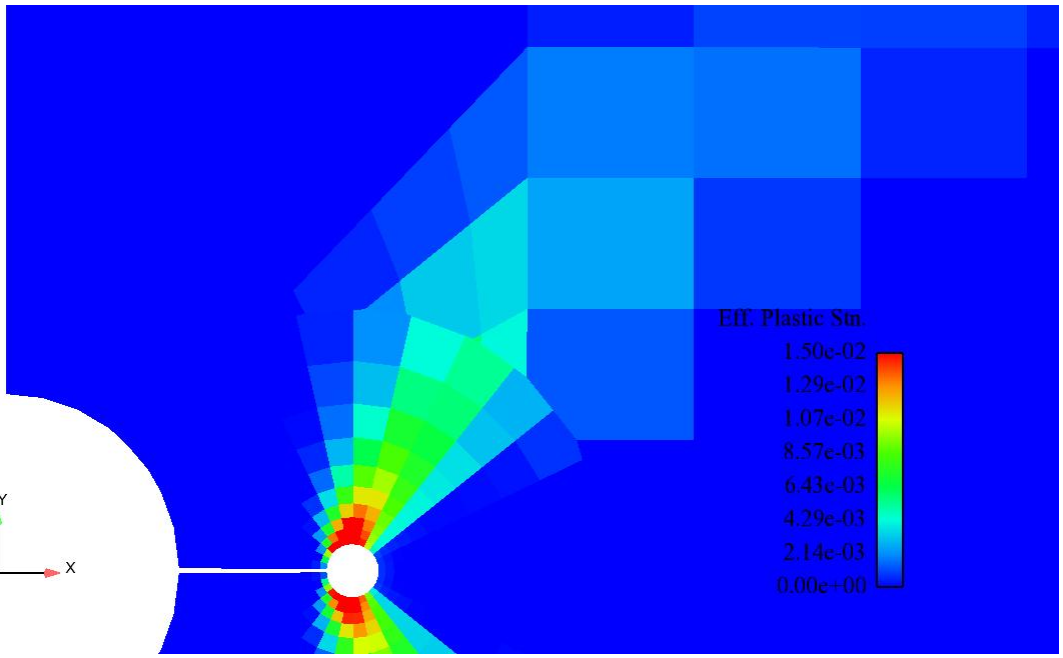

Figure 3.38 Effective plastic strain of an isotropic material simulation in FEFRAC with ER = 0.15 mm where the radius and crack have length of 1.0 mm.

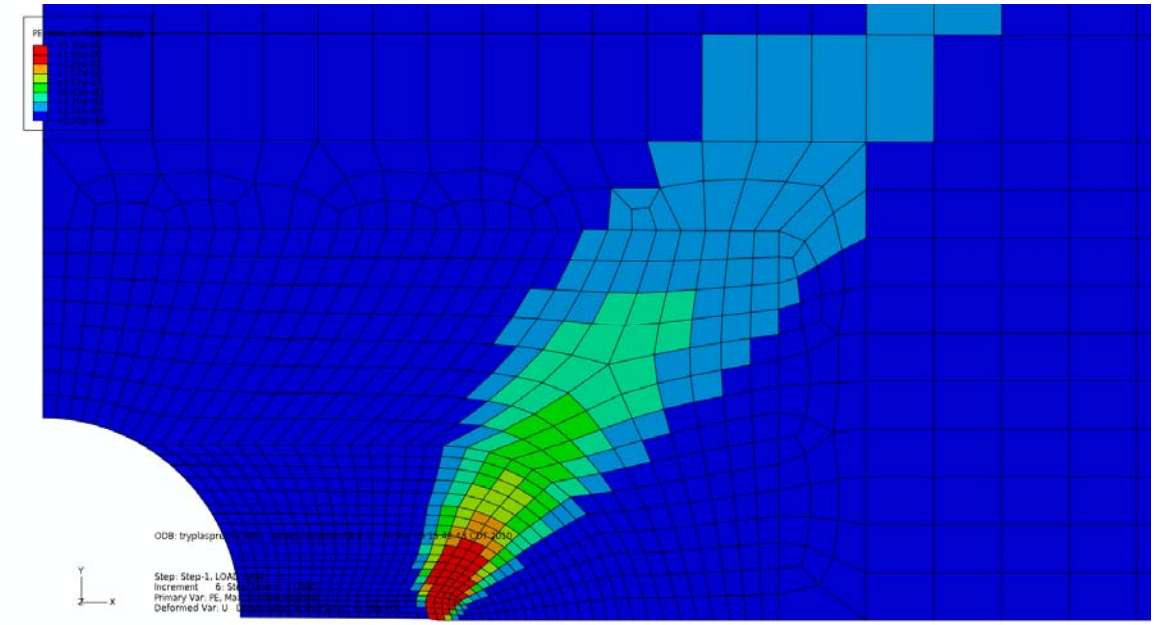

Figure 3.39 Effective plastic strain of an isotropic material simulation in Abaqus where the radius and crack have length of 1.0 mm.

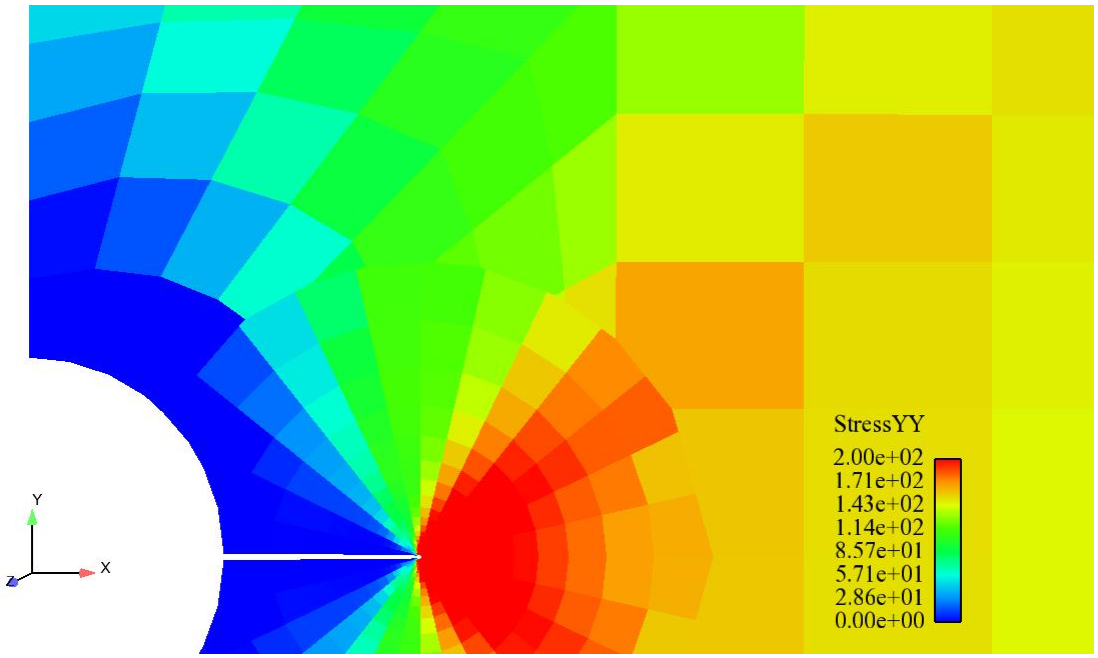

Figure 3.40 Axial stress field of an isotropic material simulation in FEFRAC with ER = 0.01 mm where the radius and crack have length of 1.0 mm.

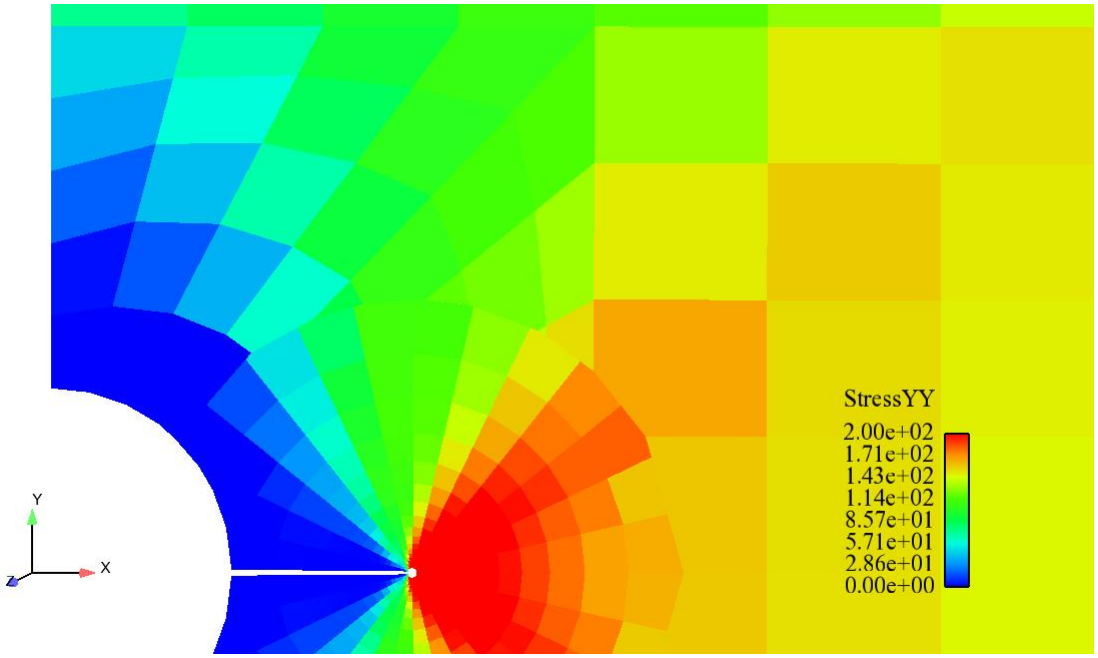

Figure 3.41 Axial stress field of an isotropic material simulation in FEFRAC with ER = 0.025 mm where the radius and crack have length of 1.0 mm.

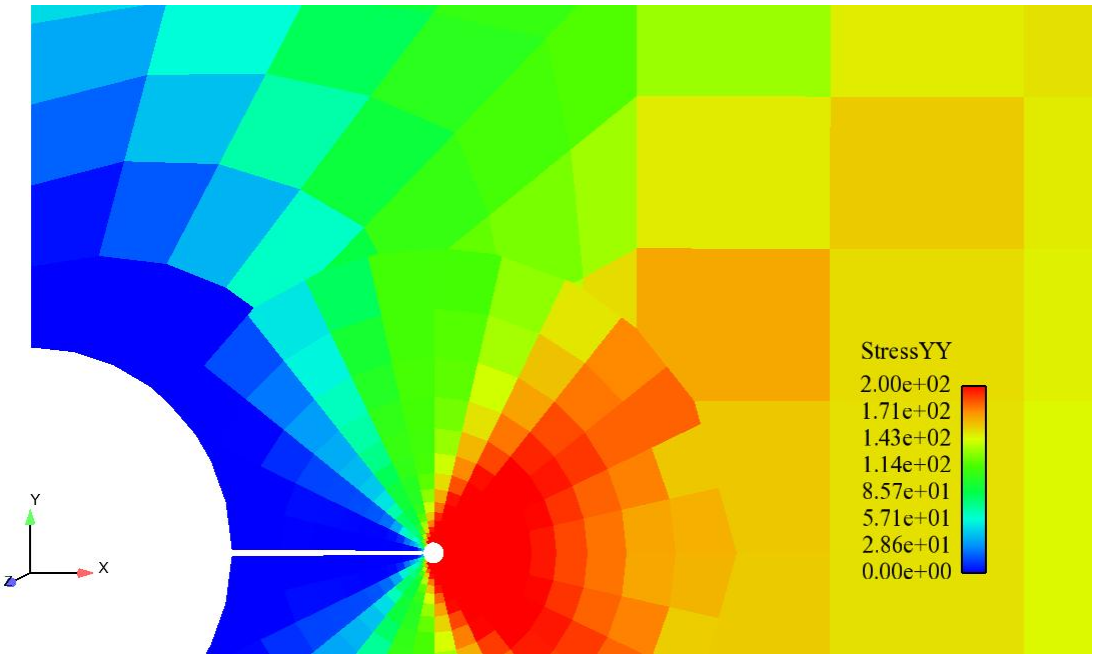

Figure 3.42 Axial stress field of an isotropic material simulation in FEFRAC with ER = 0.05 mm where the radius and crack have length of 1.0 mm.

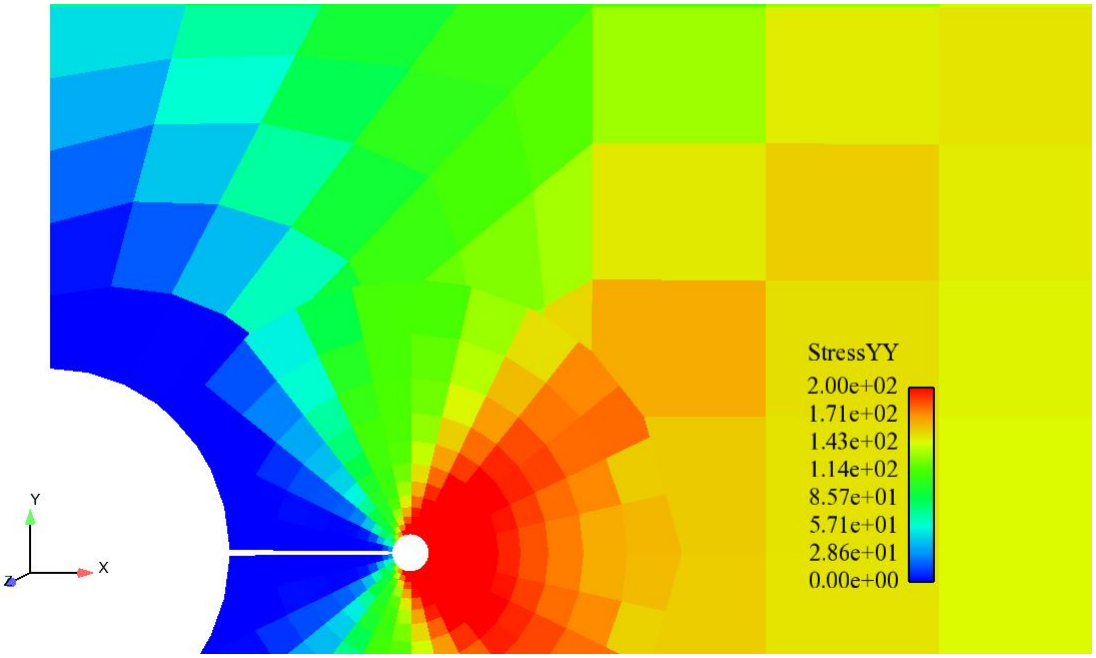

Figure 3.43 Axial stress field of an isotropic material simulation in FEFRAC with ER = 0.1 mm where the radius and crack have length of 1.0 mm.

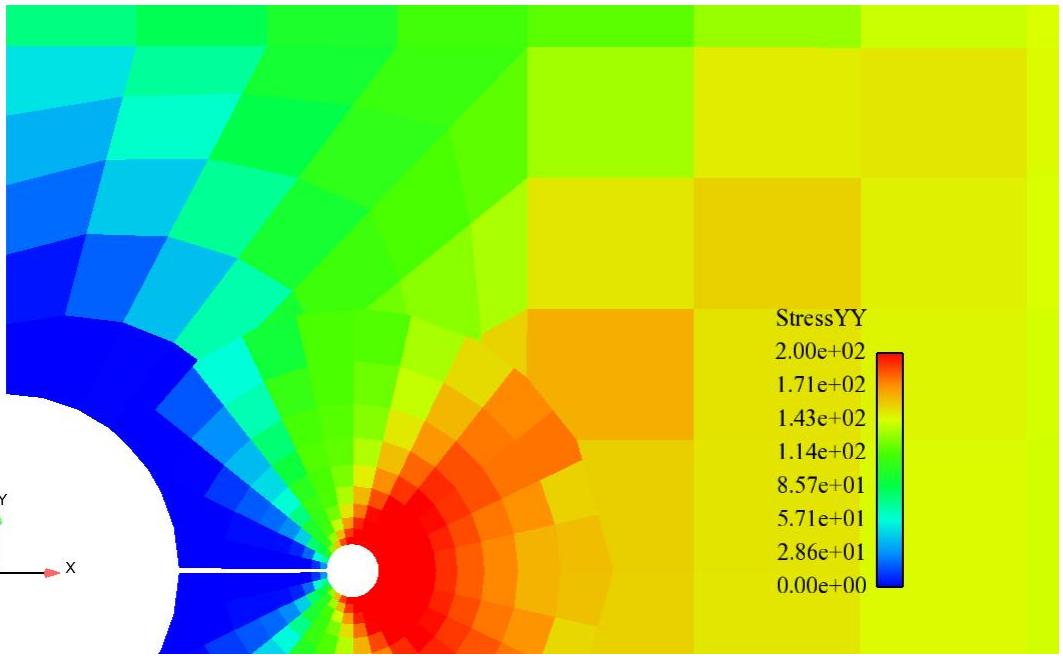

Figure 3.44 Axial stress field of an isotropic material simulation in FEFRAC with ER = 0.15 mm where the radius and crack have length of 1.0 mm.

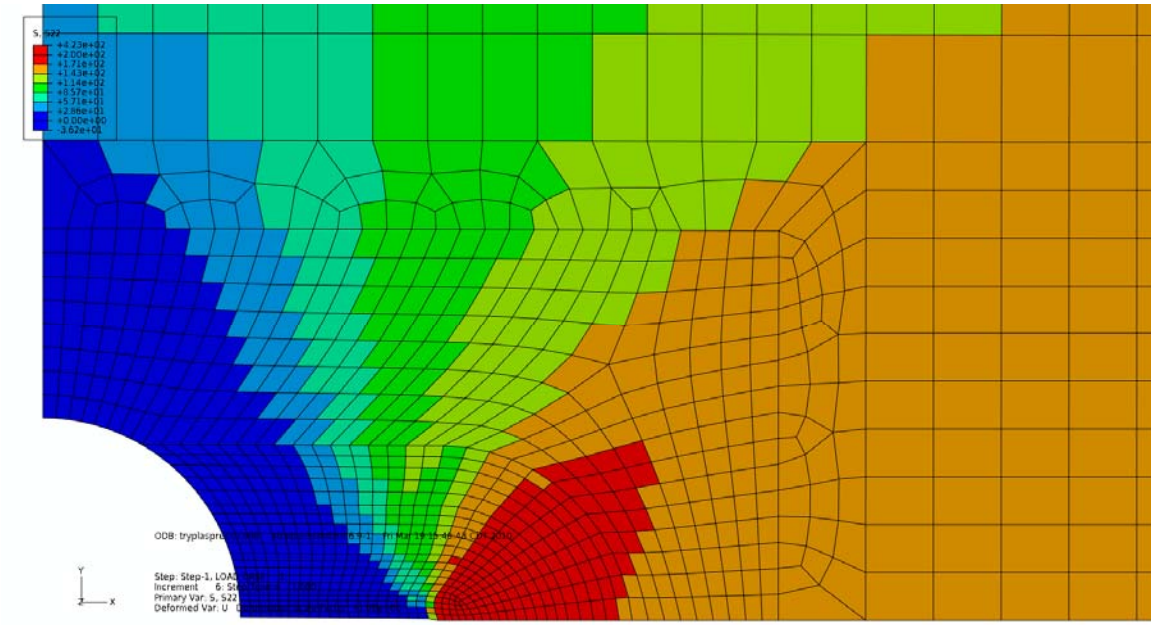

Figure 3.45 Axial stress field of an isotropic material simulation in Abaqus where the radius and crack have length of 1.0 mm.

Concluding Remarks

This chapter reviewed the efforts put into improving the visualization capabilities necessary for more complex material models and allowing a more detailed analysis of the material response. This chapter has addressed the exclusion region's appropriateness in modeling fracture occurring in ductile materials. An error analysis was performed on both isotropic linear elastic and isotropic linear hardening material models and it can be concluded that the approximate displacement field did not affect the far-field stress values or the crack-surface displacements. The existing crack surface displacement equations for symmetric cracks emanating from a hole in an infinite plate were seen to diverge from the finite element displacement results where the crack intersected the hole. Further investigation and improvement of this equation are presented in the next chapter.

CHAPTER IV

CRACK-SURFACE DISPLACEMENTS FOR CRACKS EMANATING FROM A CIRCULAR HOLE UNDER VARIOUS LOADING CONDITIONS

Abstract

The purpose of this section is to calculate and develop equations for crack-surface displacements for two-symmetric cracks emanating from a circular hole in an infinite plate for use in strip-yield crack-closure models. In particular, the displacements were determined under two loading conditions: (1) remote applied stress and (2) uniform stress applied to a segment of the crack surface (partially-loaded crack). The displacements were calculated by an integral-equation method based on accurate stress-intensity factor equations for concentrated forces applied to the crack surfaces and those for remote applied stress or for a partially-loaded crack surface. A boundary-element code was also used to calculate crack-surface displacements for some selected cases. Comparisons made with crack-surface displacement equations previously developed for the same crack configuration and loading showed significant differences near the location where the crack intersected the hole surface, but the previous equations were fairly accurate near the crack-tip location. Herein an improved crack-surface displacement equation was developed for the case of remote applied stress. For the partially-loaded crack case, only numerical comparisons are made between the previous equations and numerical integration. A rapid algorithm, based on the integral-equation method, was developed to

calculate these displacements. Because cracks emanating from a hole are quite common in the aerospace industry, accurate displacement solutions are crucial for improving life-prediction methods based on the strip-yield crack-closure models.

Nomenclature

a	crack length from edge of hole to crack tip
b	distance from centerline to concentrated forces on crack surface
b_j	distance from centerline to partially-loaded crack surface (j = 1,2)
c	distance from centerline to crack-surface displacement location
d	crack length from centerline to crack tip
E	modulus of elasticity
E'	$E/(1- \eta^2)$
G	strain-energy release rate
K	stress-intensity factor
P	applied force system
Q	virtual force applied to crack surface
r	radius of circular hole
S	remote applied stress
v	crack-surface half-displacement
V	crack-surface total displacement (2v)
x,y	Cartesian coordinates
β_j	distance from centerline to partially-loaded crack surface minus hole radius (b_j – r)
γ	ratio of b/d
Δb	width of uniform stress section on partially-loaded crack
η	material constant: 0 for plane-stress and ν for plane-strain conditions
λ	ratio of r/d
ν	Poisson's ratio
σ	uniform stress applied to partially-loaded crack surface

Introduction

Strip-yield or modified Dugdale (1960) models have been extensively used to develop crack-growth and crack-closure models for middle-crack-tension (Dill and Saff, 1976; Budiansky and Hutchinson, 1978; Fuhring and Seeger, 1979; Newman Jr., 1981) and compact (Mall and Newman Jr., 1985) specimens. A model has also been developed

for two-symmetric cracks emanating from a circular hole (Newman Jr., 1983). Cracks emanating from a circular hole are an important problem in industrial applications. This crack configuration has been extensively studied to determine the stress-intensity-factor solutions for a variety of loading conditions (Tada et. al., 2000).

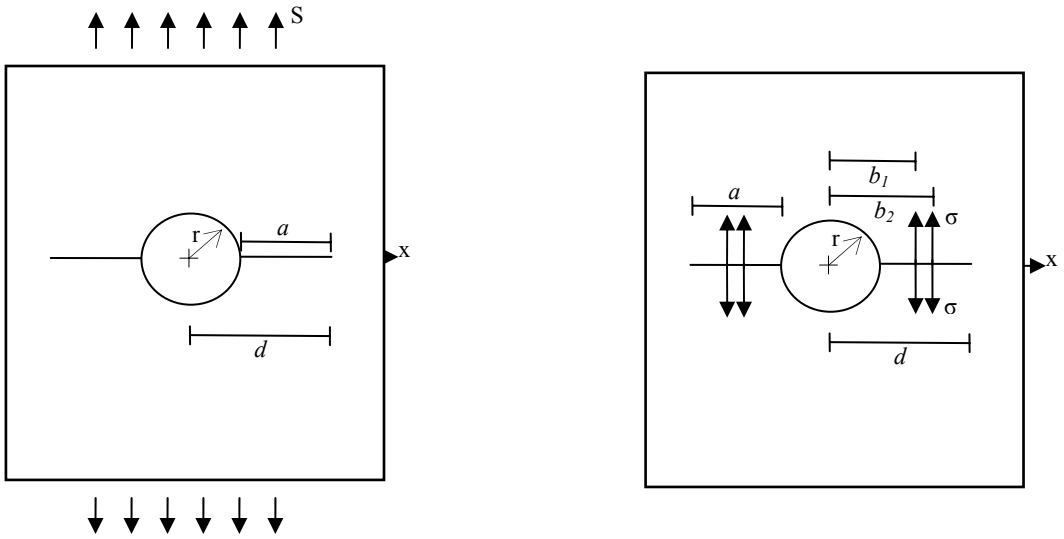

Figure 4.1 Two-symmetric cracks emanating from a circular hole under (a) remote applied stress and (b) uniform stress on crack-surface segment.

The Dugdale model is the superposition of two elastic problems. These two elastic crack problems are shown in Figure 4.1, but only stress-intensity factors are required to determine the plastic-zone length, ρ, with the uniform stress, σ, acting over the plastic-zone region being set to the flow stress (σ_o) of the material. The plastic-zone length is determined by matching the stress-intensity factors (K) for the two cases shown in Figure 4.1 using Dugdale's finite-stress condition ($K_S + K_\sigma = 0$). However, the crack-closure models also require the crack-surface displacements. Tada et. al. presents an

integral-equation method to determine crack-surface displacements for any crack configuration subjected to a desired loading condition using the Green's function for the same crack configuration subjected to concentrated forces. Shivakumar and Forman (1980) and Newman (1983) have determined the Green's function for two-symmetric cracks emanating from a circular hole in an infinite plate, as shown in Figure 4.2.

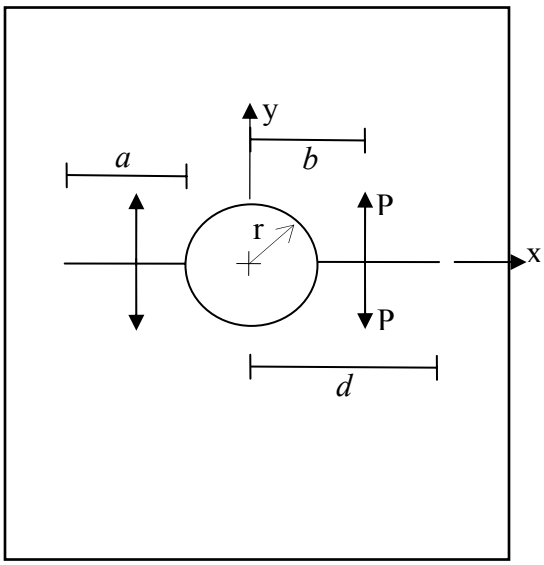

Figure 4.2 Two-symmetric cracks emanating from a circular hole under pair of concentrated forces.

Recently, there has been an interest in validating or improving the crack-surface displacements equations previously developed for two-symmetric cracks emanating from a circular hole in an infinite plate, as shown in Figure 4.1. Stress-intensity factors and crack-surface displacements are vital to the development of an accurate fatigue life prediction code based on strip-yield models. Inaccurate displacements could lead to inadequate life predictions. The motivation for this section is to investigate the accuracy of the existing displacement equations, and develop improved equations and/or rapid

integration schemes. The section is organized as follows: analysis procedures, stress-intensity factors for necessary crack configuration and loading, crack-surface displacement calculations and results, and concluding remarks.

Analysis Procedures

Analytical Crack-Surface Displacements

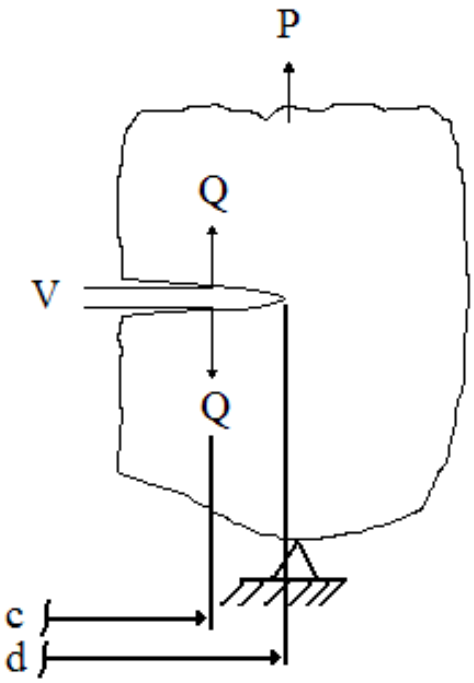

Figure 4.3 Crack in arbitrary-shaped plate subjected to an applied force system, P, and virtual forces, Q, acting on crack surfaces (Tada et. al., 2000).

The method of calculating crack-surface displacements analytically is discussed in this section. A brief review follows Appendix B in Tada et. al. (2000). Given the crack configuration in Figure 4.3 for illustrative purposes, the crack-surface

displacements are calculated. The crack configuration is only Mode I to further simplify the calculation. The strain-energy release rate, G, is expressed as

$$G = \left.\frac{\partial U_T}{\partial A}\right|_{\text{Forces Constant}} \tag{4.1}$$

with U_T representing the total strain energy and ∂A, the change in crack area. The relationship between G and stress-intensity factor is

$$G = G_I,\ E'G_I = K_I^{\,2} \text{ where } K_I = K_{IP} + K_{IQ} \tag{4.2}$$

and E' is the elastic constant dependant on either plane-stress or plane-strain conditions. K_{IP} is the stress-intensity factor for the desired loading, while K_{IQ} represents the stress-intensity factor for the virtual forces, Q, applied at the point where a displacement is desired. Combining these equations with Castigliano's theorem, simplifying and letting the force Q go to zero yields

$$V_Q = V_{Q\,\text{No Crack}} + \frac{2}{E'}\int_0^d K_{IP}\frac{\partial K_{IQ}}{\partial Q}\,dA\,. \tag{4.3}$$

The displacements are trivial when there is no crack, i.e. zero, and

$$\frac{\partial K_{IQ}}{\partial Q} = 0 \quad \text{for } a \in [0, c] \tag{4.4}$$

that results in the displacements being

$$V_Q = \frac{2}{E'}\int_c^d K_{IP}\frac{\partial K_{IQ}}{\partial Q}\,dA\,. \tag{4.5}$$

Numerical Integration

The numerical integration schemes that were applied are explained briefly in this section. Because the integrands in these crack problems are very complicated, various numerical integration schemes were used to evaluate the integrals since they could not be evaluated analytically. The goal is to find the best coefficients α_i and placement of x_i such that

$$\int_a^b f(x)dx \approx \sum_{i=0}^{N} \alpha_i f(x_i) \tag{4.6}$$

is as close as possible. There are many types of numerical integration methods available, but some lent themselves to being more applicable for the problems of interest. The interval integrated over is relatively large so none of the standard numerical integration methods would suffice. Thus, what is commonly called a composite numerical integration scheme was used. A composite scheme breaks the interval into subintervals and applies the numerical integration scheme to each individually. The results are then summed to find the final answer.

The numerical integration schemes work very well for smooth, bounded functions. But an integrand that exhibits a singularity causes obvious problems. While there are sure to exist more ways to deal with the singularity, the two most prevalent are discussed. The first and by far the simplest is to move a small distance, ε, away from the singularity point and use the function value there for the value at the singularity. The other method is to remove the singularity. One way to remove the singularity is by representing part of the integrand as a Taylor series expanded about the singularity point (Burden and Faires, 1997). The Taylor series method causes the integral to be

represented as a sum of two integrals, effectively eliminates the singularity, and provides fast convergence. The drawback is that inherent in the Taylor series calculation one must be capable of evaluating the derivative(s) of the integrand. Since the integrand for the displacements is very complex, this was not a viable method.

Nine methods of numerical integration were applied in this study. A large number was chosen to ensure that the converged solution was in fact a correct solution. Composite closed Newton-Cotes formulas used included trapezoidal, Simpson's rule, and Simpson's three-eighth's rule. A composite open Newton-Cotes formula, the mid-point rule, was also implemented.

The final method and the one relied on most heavily is a fourth degree Gauss-Legendre (G-L) based quadrature. The degree determines the number of points used to approximate the integral and the accuracy of the approximation. G-L quadrature chooses the points where it evaluates the function in an optimal manner. The points are determined by finding the roots of Legendre polynomials. The weights given to each evaluation are determined by

$$c_i = \int_{-1}^{1} \prod_{\substack{j=1 \\ j\neq i}}^{n} \frac{x - x_j}{x_i - x_j} dx \tag{4.7}$$

where n is the degree of the Legendre polynomial and x_i are the roots of the polynomial. This method is often chosen because of the property: for any polynomial, f(x), of degree less than 2n

$$\int_{-1}^{1} f(x)dx = \sum_{i=1}^{n} c_i f(x_i). \tag{4.8}$$

The weights and roots for the fourth order G-L quadrature approximations are given in Table 4.1. This method has proven to be the most accurate one implemented.

Table 4.1 Roots and weights for the Fourth order Gauss-Legendre quadrature method.

N	Root	Weight
4	.8611363116	.3478548451
	.3399810436	.6521451549
	-.3399810436	.6521451549
	-.8611363116	.3478548451

Convergence Test

Convergence when the exact solution is known is trivial. Since there is not an exact solution for most of the cases studied in this section, convergence is decided as follows. Assume the solution at the point x_i on the crack is needed. Denote the approximation of the value at x_i with k subdivisions as $f(x_i)_k$. The number of subdivisions is increased and the value is approximated again until

$$\left|f(x_i)_{k+1} - f(x_i)_k\right| < 1\times10^{-6}. \tag{4.9}$$

Convergence was determined independently for each method at each point. A number of subdivisions found to provide convergence for one method at a point are not assumed to provide convergence for the other integration schemes at that point. Nor is the number of subdivisions assumed to provide convergence at the next point even if it assured convergence with the same method at the previous point.

Stress-Intensity Factors

Remote Applied Stress

For two-symmetric cracks at a hole in a plate subjected to remote applied stress, Figure 4.1(a), the stress-intensity factor equation (Newman, 1983) was obtained by fitting results from Newman (1971) as

$$K_h^S = K_\infty^S F_h^S = S\sqrt{\pi d}\ F_h^S \tag{4.10}$$

where K_∞^S is for a crack in an infinite plate without a hole and F_h^S is the boundary-correction factor for the circular hole. The equation for F_h^S is

$$F_h^S = \sqrt{1-\frac{r}{d}}\ f_2 \tag{4.11}$$

where

$$f_2 = 1.0 + 0.358\lambda + 1.425\lambda^2 - 1.578\lambda^3 + 2.156\lambda^4 \tag{4.12}$$

with $\lambda = r/d$ for $0 \le \lambda \le 1$.

Concentrated Force

Using a boundary-collocation analysis performed by Newman, the stress-intensity factors for two cracks emanating from a circular hole subjected to a symmetric pair of concentrated forces in an infinite plate, as shown in Figure 4.2, were obtained. An equation was then developed to fit these results (Newman, 1983) and is

$$K_h^P = K_\infty^P F_h^P = \frac{2Pd}{\sqrt{\pi d\left(d^2 - b^2\right)}} F_h^P \tag{4.13}$$

where K_{∞}^{p} represents the stress-intensity factor for a crack in an infinite place without a hole and F_h^p is the boundary correction factor for the circular hole. The equation for F_h^p is

$$F_h^p = 1 + A_1\left(\frac{1-\gamma}{1-\lambda}\right) + A_2\left(\frac{1-\gamma}{1-\lambda}\right)^2 \tag{4.14}$$

$$A_1 = -0.02\lambda^2 + 0.558\lambda^4 \tag{4.15}$$

$$A_2 = 0.221\lambda^2 + 0.046\lambda^4 \tag{4.16}$$

where $\gamma = b/d$, $\lambda = r/d$ for $\lambda \le \gamma \le 1$ and $0 \le \lambda < 1$. Shivakumar and Forman (1980) also developed a Green's function for the same crack configuration using double-series polynomials with about 30 terms. Comparisons made between the two Green functions indicated that they were within about 1% for crack-length-to-hole-radius (a/r) ratios greater than 0.001 (nearly an edge crack) and within 0.1% for a/r > 0.2. For both loading conditions studied in this section, $\frac{\partial K_{IQ}}{\partial Q}$ in equation (4.5) is

$$\frac{\partial K_{IQ}}{\partial Q} = \frac{\partial K_h}{\partial Q} = \frac{2d}{\sqrt{\pi d\left(d^2 - b^2\right)}} F_h^P \quad . \tag{4.17}$$

Partially-Loaded Crack Surface

The stress-intensity-factor equation for two-symmetric cracks at a hole subjected to uniform stress on a segment of the crack surface, Figure 4.1(b), was derived using equation (4.13) as a Green's function while integrating from b_1 to b_2. The equation for the stress-intensity factor (Newman, 1983) is

$$K_h^{\sigma} = \frac{2\sigma}{\pi}\sqrt{\pi d}\, G(\gamma,\lambda) \tag{4.18}$$

$$G(\gamma,\lambda) = \left\{\left[1 + \frac{A_1}{1-\lambda} + \frac{3A_2}{2(1-\lambda)^2}\right]\sin^{-1}\gamma + \left[\frac{A_1}{1-\lambda} + \frac{(4-\gamma)A_2}{2(1-\lambda)^2}\right]\sqrt{1-\gamma^2}\right\}\Bigg|_{\gamma=\frac{b_1}{d}}^{\gamma=\frac{b_2}{d}}. \tag{4.19}$$

Rewriting K_h^{σ} so it is in a form similar to the K solutions in the previous problem, i.e. the solution for a partially-loaded crack in an infinite body times a correction factor that accounts for the effect of the hole,

$$K_h^{\sigma} = K_{\infty}^{\sigma} F_h = \frac{2\sigma}{\pi}\sqrt{\pi d}\left[\sin^{-1}\left(\frac{b_2}{d}\right) - \sin^{-1}\left(\frac{b_1}{d}\right)\right]F_h^{\sigma} \tag{4.20}$$

$$F_h^{\sigma} = \frac{G(\gamma,\lambda)}{\sin^{-1}\left(\frac{b_2}{d}\right) - \sin^{-1}\left(\frac{b_1}{d}\right)}. \tag{4.21}$$

Crack-Surface Displacements

The crack-surface displacement results were normalized to provide useful data to the research community. The method of normalization was to take the crack-surface half-displacement (v) and multiply by E'/(Sa) or E'/(σa). Verification and validation of the numerical implementation was done by studying the limiting cases as the crack-length-to-hole radius (a/r) approached zero (edge crack) and as the hole radius approached zero, i.e. a single crack in an infinite plate. For these limiting cases, accurate or exact solutions exist (Tada et. al, 2000).

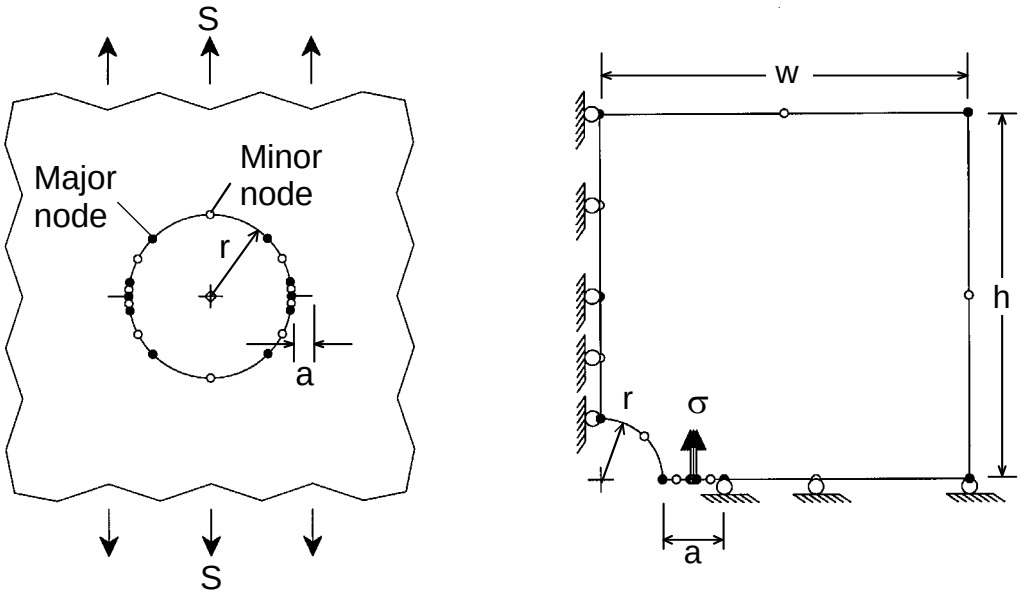

Figure 4.4 Models used in FADD2D boundary-element analyses with and without a crack for cracks emanating from a circular hole under (a) remote applied stress and (b) uniform stress on crack surface.

As a further verification, the FADD2D (Chang and Mear, 1996), boundary-element code, was used to calculate some of the crack-surface displacements to compare with the integral-equation method. Using FADD2D, two-symmetric cracks from a hole in an infinite plate under remote applied stress were analyzed to obtain the displacements at the crack-hole intersection location. A typical FADD2D model is shown in Figure 4.4(a). The solid symbols indicate major boundary nodes, while the open symbols show the mid-side (minor) nodes. Convergence studies were made to determine the appropriate number of boundary elements to obtain accurate stress-intensity factors and crack-surface displacements. The current FADD2D code does not calculate crack-surface displacements, but only gives boundary displacements, such as along the circular hole. But the code was also used to simulate a crack as a boundary with a circular hole in a very large plate to calculate crack-surface displacements for remote applied stress and

for partially-loaded crack cases. A typical model for the partially-loaded crack from a hole in a very large plate is shown in Figure 4.4(b). Note that in the actual models used, the width (w) and height (h) were 50 times the hole radius to eliminate any influence of the external boundary. Using this approach, however, the displacements near the crack tip are not as accurate, as expected.

Remote Applied Stress

The first case investigated was that of two-symmetric cracks emanating from a circular hole in an infinite plate subjected to a remote applied stress, as shown in Figure 4.1(a). Exact crack-surface displacements for a crack in an infinite plate were obtained using Westergaard stress functions (Tada et. al., 2000). The displacement equation was then modified to approximately account for the hole (Newman, 1983). The current equation to calculate displacement at location x is

$$v_h^S = \frac{2(1-\eta^2)S}{E}\sqrt{d^2 - x^2}\ F_h^S \qquad (4.22)$$

where F_h^S is defined by equation (4.11). This form was selected so that the crack-surface displacements near the crack tip would be as accurate as the stress-intensity factor solution.

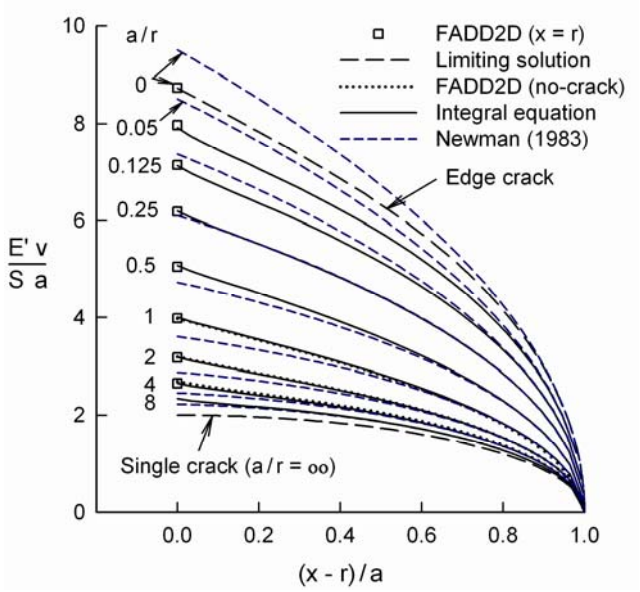

Figure 4.5 Normalized displacements for cracks emanating from a hole in an infinite plate subjected to remote applied stress for various a/r ratios for various methods and previous equation.

Using the methods described in the analytical displacements and numerical integration sections, the crack-surface displacements were calculated. These results are shown as solid curves in Figure 4.5. The normalized displacement is plotted against the normalized location along the crack surface, (x – r)/a. FADD2D results are also shown at x = r (edge of hole, square symbols) and along the crack surface (dotted curve) for a/r values of 1, 2 and 4. The limiting cases for an edge crack (a/r = 0) and for a single crack in an infinite plate (r = 0) are also shown for comparison. The integral-equation and FADD2D results agreed very well (within 1% away from the crack tip) for all cases considered. In addition, the numerical results were also compared with the existing displacement equation (eqn. 4.22). For a/r > 0.25, the existing equation underestimated the displacements, while for a/r < 0.25, the equation overestimated the displacements.

For all cases, the largest error occurred at the intersection of the hole and crack surface. The maximum error was about 10% for an a/r ratio of 1.

A new equation was then developed to fit the solutions from numerical integration. The new equation to calculate crack-surface displacement at location *x* is

$$\frac{E'v}{Sa} = 2\left[\left(\frac{d}{a}\right)^2 - \left(\frac{x}{a}\right)^2\right]^{0.5} F_h H \tag{4.23}$$

$$F_h = \left[1 - \left(\frac{r}{d}\right)\right]^{0.5} f_2 \tag{4.24}$$

$$H = 1.0 + A\xi + B\xi^m \tag{4.25}$$

$$\xi = \frac{d - x}{a} \tag{4.26}$$

$$m = 8.0 - \frac{5.0}{\left(1 + \left(\frac{a}{r}\right)\right)^{20}} \tag{4.27}$$

$$A = \frac{-0.14}{\left(1 + \frac{a}{r}\right)^4} + \frac{0.46\frac{a}{r}}{\left(1 + \frac{a}{r}\right)^{2.7}} \tag{4.28}$$

$$B = \frac{0.37}{\left(1 + \frac{a}{r}\right)^{0.85}} - \frac{0.36}{\left(0.5 + \frac{a}{r}\right)^{1.5}} + \frac{0.168}{\left(0.6 + \frac{a}{r}\right)^{2.8}}. \tag{4.29}$$

These equations agree within 1.2% of the numerical integral equation results and match the limiting cases very well, as shown in Figure 4.6.

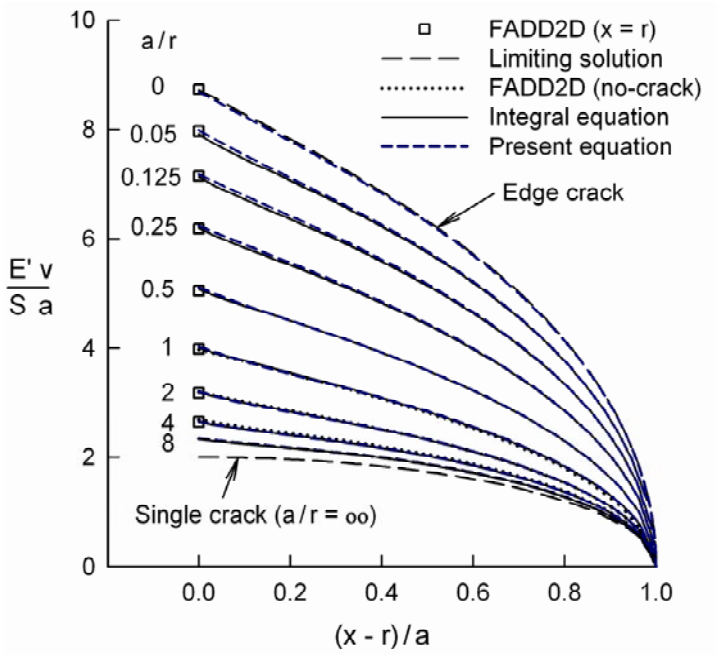

Figure 4.6 Normalized displacements for cracks emanating from a hole in an infinite plate subjected to remote applied stress for various a/r ratios for various methods and present equation.

Partially-Loaded Crack Surface

The second case studied was the partially-loaded crack emanating from a hole, as shown in Figure 4.1(b). The current approximate crack-surface displacement solution at location x is

$$V_h^{\sigma} = [V_{\infty}(x) + V_{\infty}(-x)]F_h^{\sigma} \tag{4.30}$$

$$V_{\infty}(x) = \frac{4(1-\eta^2)\sigma}{\pi E}\left[(b-x)\cosh^{-1}\left(\frac{d^2-bx}{d|b-x|}\right) + \sqrt{d^2-x^2}\sin^{-1}\left(\frac{b}{d}\right)\right]\Bigg|_{b=b_1}^{b=b_2}. \tag{4.31}$$

When the hole radius is zero, the configuration reduces to a partially-loaded crack in an infinite body, which has an exact solution (Tada et. al., 2000). Equation (4.30) converges to the exact solution as the hole radius tends to zero. The special case of *r = 0* was also

used to determine which numerical integration scheme would give the most accurate solution for the least amount of work. As expected, the Gauss-Legendre quadrature was the best performing scheme.

The goal is to numerically integrate equation (4.5) with the correct substitutions,

$$V_P = \frac{8(1-\eta^2)\sigma}{\pi E}\int_x^d \frac{aG(\gamma,\lambda)}{\sqrt{(a^2-x^2)}} F_h^P da \tag{4.32}$$

and compare the displacements with the current formula. Note that F_h^P is a function of $\gamma = b/d$, $\lambda = r/d$ for $\lambda \le \gamma \le 1$ and $0 \le \lambda < 1$. The integral in equation (4.32) has to be broken into two integrals to evaluate numerically: (1) region of applied stress and (2) region beyond the stress to the crack tip. Thus, the displacement was calculated as follows. The displacement of a point x such that $x \le b_1$ is calculated by

$$V_P = \frac{8(1-\eta^2)\sigma}{\pi E}\left[\int_{b_1}^{b_2} G(\gamma,\lambda)\Big|_{\gamma=\frac{b_1}{a}}^{\gamma=1} \frac{aF_h^P}{\sqrt{a^2-x^2}} da + \int_{b_2}^{d} G(\gamma,\lambda)\Big|_{\gamma=\frac{b_1}{a}}^{\gamma=\frac{b_2}{a}} \frac{aF_h^P}{\sqrt{a^2-x^2}} da\right]. \tag{4.33}$$

For a point within the applied stress region, i.e. $x \in [b_1, b_2]$, displacement is calculated by

$$V_P = \frac{8(1-\eta^2)\sigma}{\pi E}\left[\int_{x}^{b_2} G(\gamma,\lambda)\Big|_{\gamma=\frac{b_1}{a}}^{\gamma=1} \frac{aF_h^P}{\sqrt{a^2-x^2}} da + \int_{b_2}^{d} G(\gamma,\lambda)\Big|_{\gamma=\frac{b_1}{a}}^{\gamma=\frac{b_2}{a}} \frac{aF_h^P}{\sqrt{a^2-x^2}} da\right]. \tag{4.34}$$

Finally, for a point beyond the applied stress, $x \ge b_2$, the displacement equation becomes

$$V_P = \frac{8(1-\eta^2)\sigma}{\pi E}\left[\int_{b}^{d} G(\gamma,\lambda)\Big|_{\gamma=\frac{b_1}{a}}^{\gamma=\frac{b_2}{a}} \frac{aF_h^P}{\sqrt{a^2-x^2}} da\right]. \tag{4.35}$$

With the three equations for displacement along the whole length of the crack developed, simulations were conducted for various ratios of crack-length-to-hole-radius (a/r) ratios.

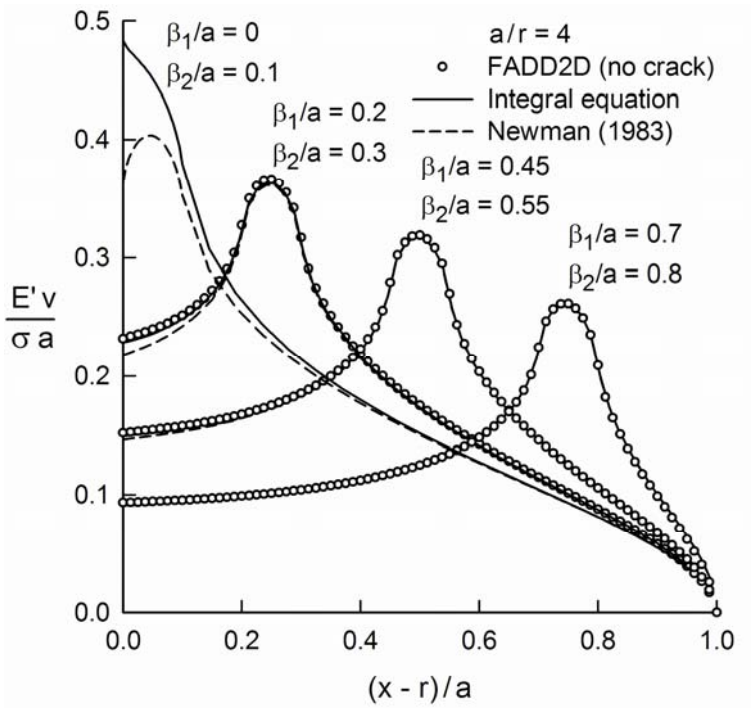

(a) a/r = 4

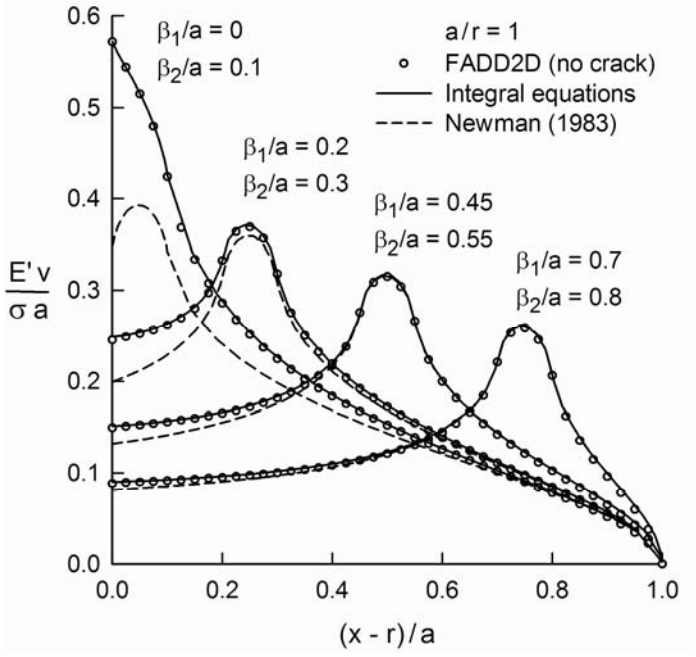

(b) a/r = 1

Figure 4.7 Normalized displacements for cracks emanating from a hole in an infinite plate subjected to uniform stress on various crack-surface segment locations for various a/r ratios.

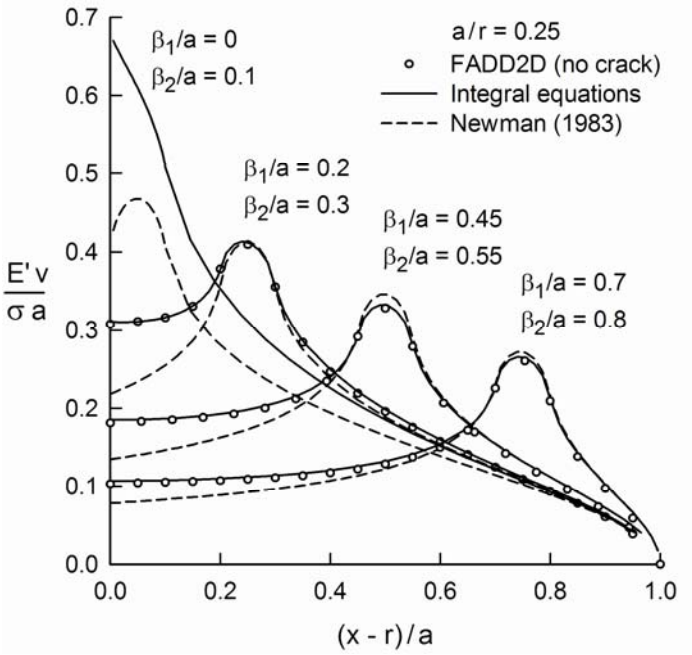

(c) a/r = 0.25

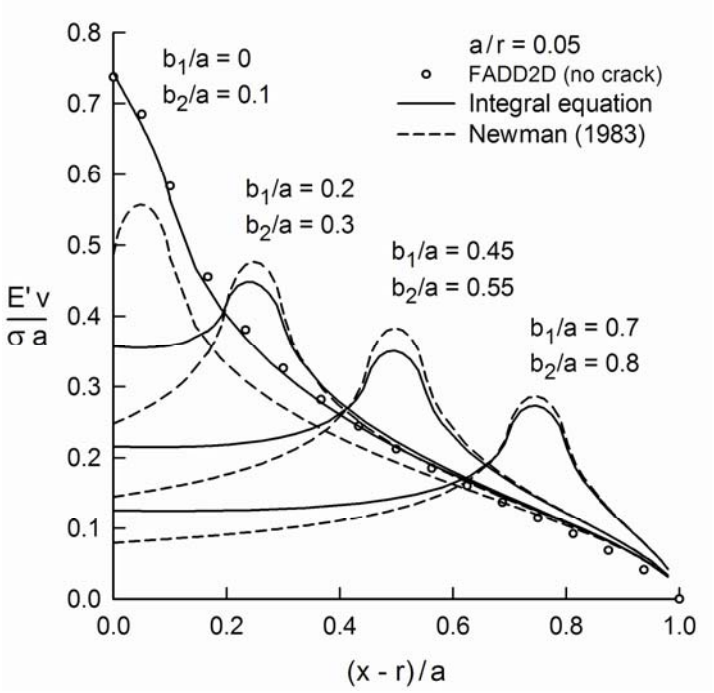

(d) a/r = 0.05

Figure 4.7 (continued)

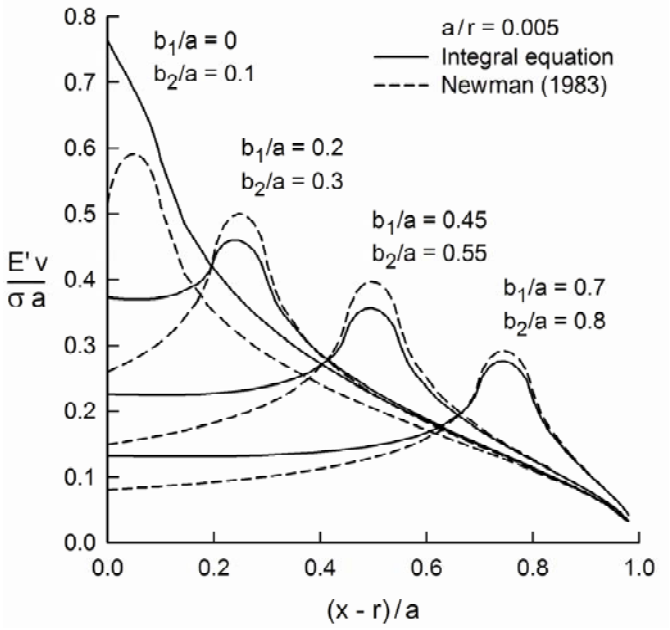

(e) a/r = 0.005

Figure 4.7 (continued)

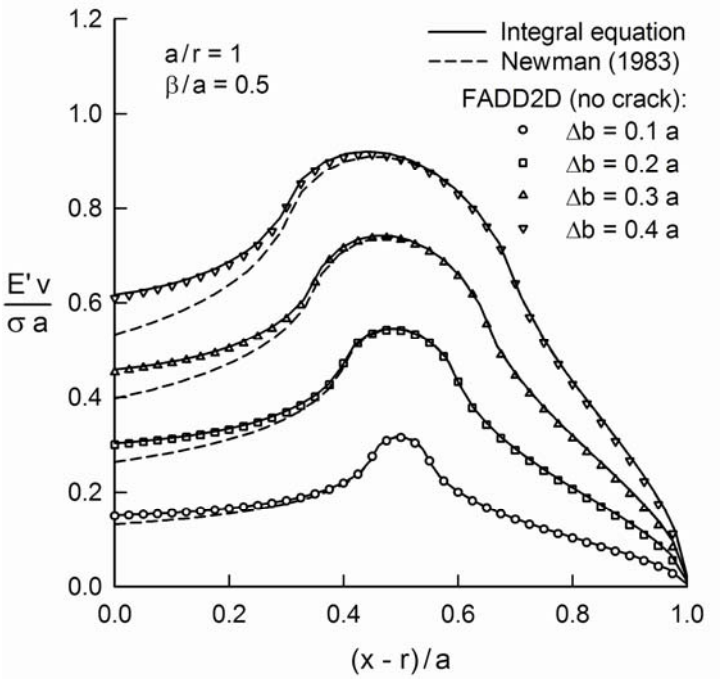

Figure 4.8 Normalized displacements for cracks emanating from a hole in an infinite plate subjected to uniform stress on various width crack-surface segments with β/a = 0.5 and a/r = 1.

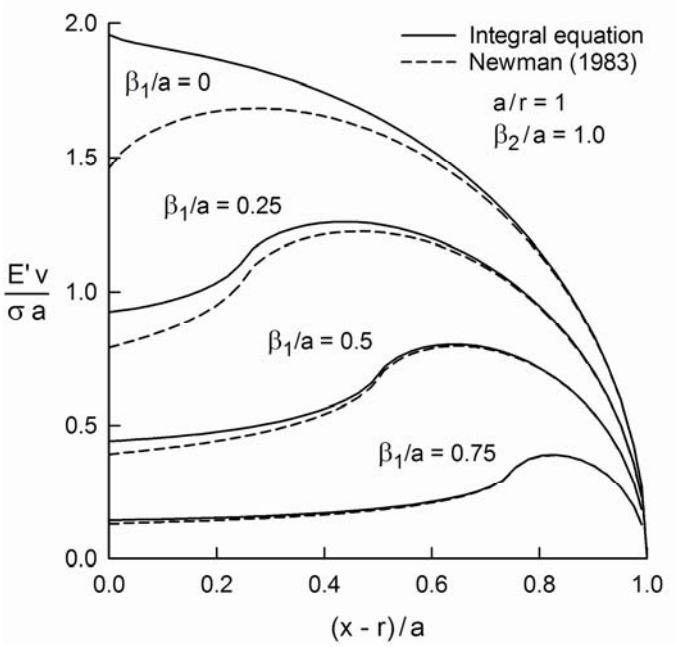

Figure 4.9 Normalized displacements for cracks emanating from a hole in an infinite plate subjected to uniform stress on various width crack-surface segments with $\beta_2/a = 1$.

Crack configurations were analyzed for a/r ratios of 8, 4, 2, 1, 0.5, 0.25, 0.125, 0.05 and 0.005 with loading centered at 0.05a, 0.25a, 0.5a and 0.75a with a uniform stress segment of width 0.1a. Some additional analyses were conducted by varying the width $(b_2 - b_1)$ of the uniform stress segment for a fixed a/r ratio, and by setting $(b_2 - r)/a = \beta_2/a = 1$ and varying the $(b_1 - r)/a$ (or β_1/a) ratios, like the loading used in the Dugdale model (1960). Some typical results are shown in Figures 4.7-4.9, which shows comparisons among the integral-equation method, FADD2D (no crack) results, and the Newman (1983) equations. These results show that the existing equations for crack-surface

displacements are severely lacking in some cases. As the a/r ratio becomes large, the existing equations fit the results reasonably well provided the loading is not near the hole. Once the a/r ratio is less than 2, the existing equations falter near the crack-hole intersection location. As the crack configuration approaches an edge crack, i.e. a/r → 0, the errors begin to increase rapidly, as shown in Figure 4.7(c)-4.7(e). Regardless of the a/r ratio, the displacement equations provide good results for location between the loading section and the crack tip. Efforts were made to develop a new equation for the partially-loaded crack without success. Thus, a rapid algorithm, based on the integral-equation method, was developed to calculate the crack-surface displacements for the partially-loaded crack.

Further studies are needed to assess how these errors in the crack-surface displacement equations will influence crack-opening load calculations in the strip-yield crack-closure model (Newman Jr., 1981; Mall and Newman Jr., 1985; Newman Jr., 1983). During crack-growth and crack-closure simulations for cracks emanating from a hole, crack-surface contact stresses near the crack tip are high (close to the yield stress of the material), where the existing equations were shown to be the most accurate. The magnitude of the contact stresses decays rapidly away from the crack-tip region. At high load ratios (R = minimum to maximum load), the crack surfaces do not contact near the hole-crack intersection region. Thus, the inaccurate crack-surface displacement equations are not used and would not have any influence on the calculated crack-opening loads. However, under compressive loading, the crack surfaces near the hole-crack intersection region would contact, but the contact stresses would be lower than those near the crack tip, so their influence on calculated crack-opening loads would be much lower.

But further studies are required to assess the influence of these findings on fatigue- and crack-growth life predictions made with the strip-yield models.

Concluding Remarks

Crack-surface displacements for two types of loading (remote applied stress or partially-loaded crack) on two-symmetric cracks emanating from a circular hole in an infinite plate were calculated from an integral-equation method. The displacements were calculated over a wide range in crack-length-to-hole-radius (a/r) ratios from 0.005 to 8. In addition, the limiting cases of an edge crack (a/r = 0) and a single crack in an infinite plate (r = 0) were also calculated. These results were compared with some previously developed equations for the same crack configuration and loading from the literature. The existing equations were found to be accurate for crack-length-to-hole-radius (a/r) ratios greater than 2, but significant errors occurred for a/r ratios less than 2. Regardless of the a/r ratio, the displacement equations provide good results near the crack tip.

For the remote applied stress case, the errors became larger as the displacement location approached the hole-crack intersection location. The maximum error was about 10% and occurred at an a/r ratio of 1. A new crack-surface displacement equation was developed and agreed within 1.2% of the numerical integration results over a wide range in a/r ratios from an edge crack (a/r = 0) to a single crack in an infinite plate (r = 0).

For the partially-loaded crack, the previous crack-surface displacement equations were found to be adequate for large cracks and for all points between the loaded section and the crack tip. But between the loaded section and the hole, the existing displacement equations exhibited large errors. As the a/r ratio tended to zero, the existing displacement

equation was no longer accurate, except near the crack-tip location. Thus, a rapid algorithm, based on the integral-equation method, was developed to calculate these displacements.

Because cracks emanating from a hole are quite common in the aerospace industry, accurate displacement solutions are crucial for improving life-prediction methods based on the strip-yield crack-closure models. But further studies are required to assess the influence of these findings on fatigue- and crack-growth life predictions made with strip-yield models.

CHAPTER V

DAMAGE BASED CRACK GROWTH

Introduction

As seen in the literature review of this dissertation, there are many well known methods that are used to predict fracture. Very few, however, incorporate physical measurable material parameters and introduce the physics/material properties in the failure prediction method. The purpose of this chapter is to review the methods which tie damage evolution to crack growth, point out their drawbacks, to show that while the studies mentioned work well for bulk materials with idealized defects, they can not adequately capture the physical events in a material containing defects occurring in front of a crack, and to introduce two alternative methods.

The first type of these methods is the cohesive zone model (Dugdale, 1960). The cohesive zone's limitation is the crack path must be known a priori. The cohesive zone approach exhibits mesh dependence because the cohesive zone interface elements are placed between conventional finite elements. Inserting interface elements along every boundary between finite elements is the closest one can come to achieving mesh independence, but this can cause the material to be artificially compliant and still restricts growth along element boundaries.

The CTOD and CTOA methods (Wells, 1961; Irwin, 1961) are considered physically motivated because they are measurable parameters. They can be used in

determining when a crack will advance in a simulation, but it is not clear how the direction of advance is determined from these methods. They have been proven to be constants provided the crack-length-to-thickness ratio and the uncracked-ligament-to-thickness ratio is greater than or equal to 4 (Newman et. al., 2003) and successfully used in the aerospace industry.

The introduction and development of damage mechanics is attributed to Kachanov (1958) and Rabotnov (1969). Chaboche (1988a; 1988b) suggests that one would expect a direct relationship between damage evolution in a material and crack growth as well as crack initiation. A direct link between damage evolution and crack growth alleviates the need for the introduction of a separation criterion. Damage evolution was proved to be an accurate predictor of crack initiation (Horstemeyer, 2001). Damage mechanics for ductile metals is broken down into the following damage mechanisms: void growth, nucleation, and coalescence. These mechanism roles in crack propagation are shown in Figure 5.1. Extensive studies have been done to determine relationships between microscopic voids and the material's bulk response (McClintock, 1968; Rice and Tracey, 1969). Efforts were also put into determining a material's response when the material had an effective void volume fraction (Davidson et. al., 1977; Cocks-Ashby, 1981; Gurson, 1977). These two models vary in that the Cocks-Ashby is driven by plastic strain and the Gurson model is affected by the hydrostatic stress.

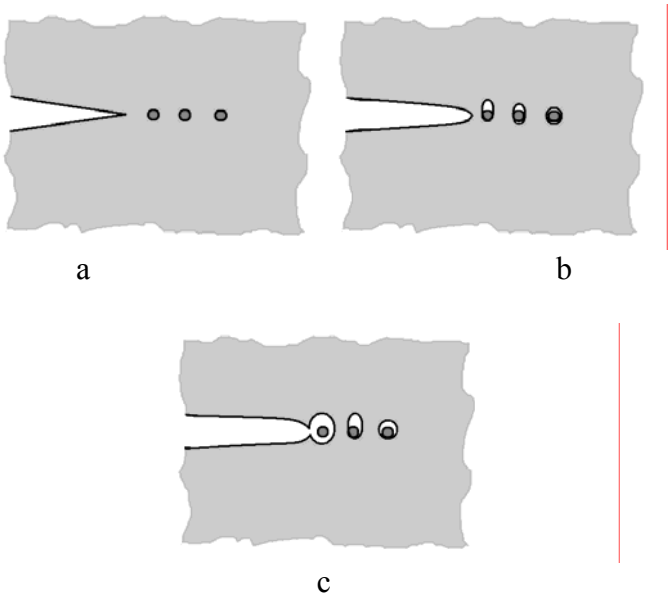

Figure 5.1 Crack growth in ductile metals. (a) Original state, (b) Voids nucleating from particles in front of the crack tip, and (c) voids growing and coalescing into the crack tip (Anderson ,2005).

Xia and Shih (1995) used a combination of J_2 plasticity with the Gurson model to predict a fracture path based on the void volume fraction parameter. Xia and Shih used the term "computational cells" to describe the insertion of the elements in front of the crack tip. They take advantage of the symmetry of a cracked body and use node release methodology along the symmetry line once it is determined the crack should grow. They state that no limit is placed on crack advance except that the crack must grow along the symmetry line. The width of the computational cells is the increment of crack advance, and is related to a measurable material parameter. The computational cells' material response is a Gurson model while the remainder of the elements in the simulation follows a J_2 behavior. They note that the Gurson model is necessary because the dilatant plasticity is capable of describing the void growth. The addition of computational cells implies the crack path must still be known a priori.

The extended finite element method (X-FEM) (Belytschko and Black, 1999) has also been used for stable crack growth during fracture. X-FEM's use is confined to the realm of small-strains. The enrichment functions, as described in the literature review, are based on linear elastic fracture mechanics and cannot capture the response when significant plasticity occurs. It is not immediately clear how one would incorporate material properties into the extended finite element method.

J_2 plasticity based models (Rice and Tracey, 1969; Bammann et. al., 1996) have been widely used to predict the onset of failure by progression of the damage mechanisms previously mentioned. A parameter has yet to be found in these J_2 models that determines crack advance and direction. This chapter shows that plastic strain variable is not an optimal parameter and attempts to find the optimal parameter for damage accumulation in the presence of a crack and crack propagation

J_2 Plasticity

There are many J_2 plasticity based models that exist, but because they are all driven by the same thing, plastic strain, it is only necessary to consider one here. The internal state variable plasticity model developed by Bammann, Chiesa, and Johnson (Bammann, 1989; Bammann, et. al, 1996) and introduced in the literature review is a J_2 based model which incorporates a void volume fraction parameter. The parameter's evolution is the Cocks-Ashby equation (1981) for spherical voids in a material. The BCJ model has been implemented into an Abaqus user material (UMAT) subroutine which was used to verify the BCJ was implemented correctly into our code, FEFRAC. One element simulations shown in Figure 5.2 were run in both FEFRAC and Abaqus. The

stress-strain results for both simulations are shown in Figure 5.3. The stress-strain results show excellent agreement prior to bifurcation. After bifurcation the results are non-unique and dependent on the solver used in the program. The damage evolution for both simulations is shown in Figure 5.4 and again shows good agreement prior to bifurcation. Thus, it has been verified that the BCJ constitutive model is correctly implemented into our finite element fracture program.

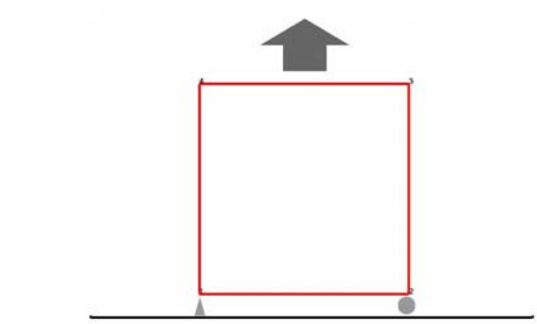

Figure 5.2 Loading and boundary conditions applied for the one element simulation.

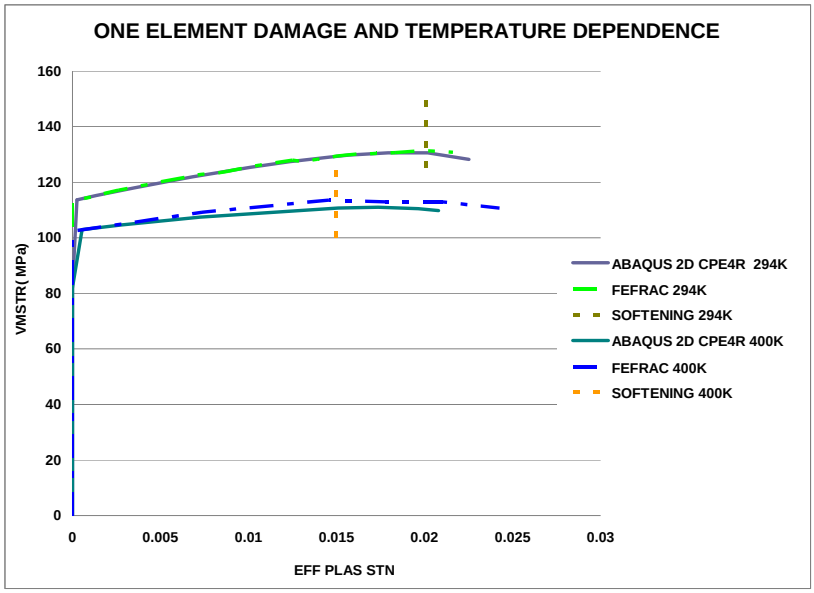

Figure 5.3 Von Mises stress versus effective plastic strain for a one element simulation.

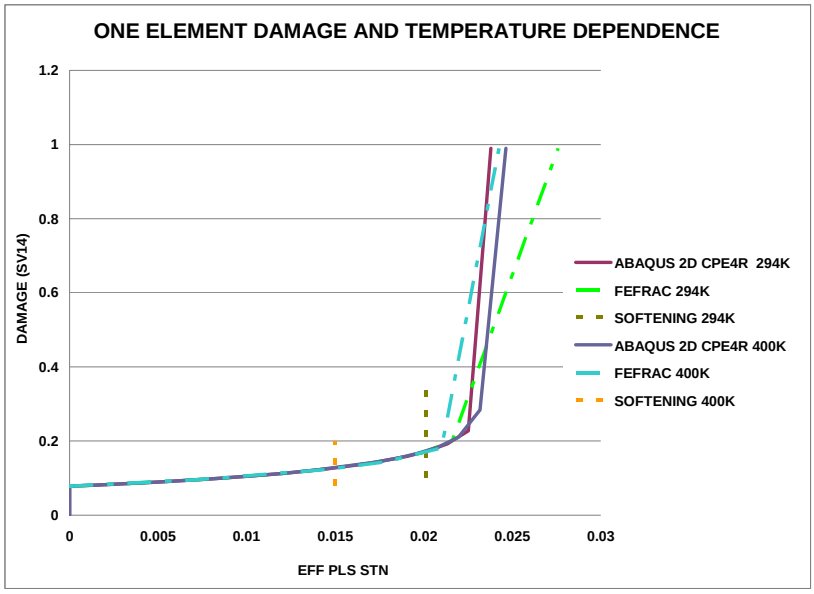

Figure 5.4 Damage versus effective plastic strain are shown for a one element simulation.

The BCJ constitutive model is used to represent the material response for the specimen and loading shown in Figure 5.5. The specimen is a standard compact specimen with a preexisting crack as shown along the centerline. The crack was advanced based on the calculated CTOA value. The results shown are using the exclusion region theory because the angular dependence of variables is easier to capture, and Chapter III showed that the results are in excellent agreement with other finite element programs.

The direction of crack advance was determined by the direction which maximizes the normal opening force along the exclusion region boundary. The initial damage field was chosen to be uniform. The damage field around the exclusion region midway through the simulation and at the end of the simulation is shown in Figure 5.6a and 5.6b, respectively. The damage values for the elements around the exclusion region boundary are plotted for each time step in Figure 5.8 using Figure 5.7 as a reference for direction.

The crack trajectory is known to grow straight ahead or π radians for the symmetric geometry and loading conditions. Figure 5.8 shows the maximum damage values are behind the crack tip and the damage is changing very little at the correct angle. Figure 5.6b shows the behavior of the damage field after the crack has advanced several times. The plastic strain field is known to be a double lobed shape centered on the crack tip. What has been seen and shown in Chapter III is that the maximum von Mises stress occurs on the back of the lobes, and this behavior causes the plastic strain's maximum to occur behind the crack tip.

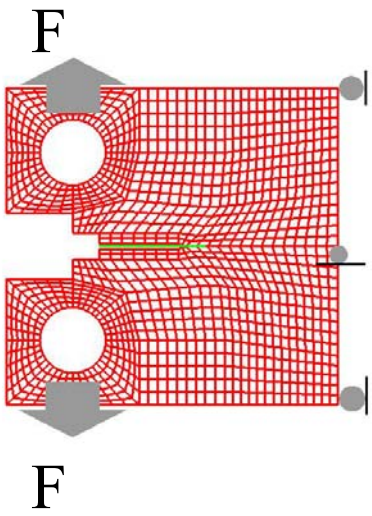

Figure 5.5 A schematic of the test case where the evolution of damage is studied.

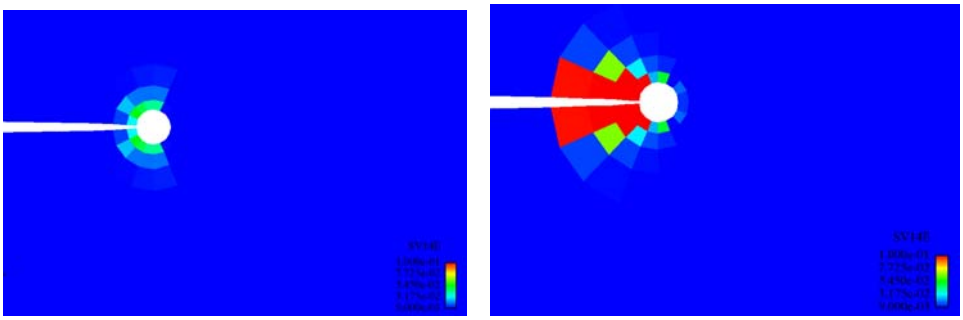

a b

Figure 5.6 With a damage scale from .009 to .1, here is (a) damage evolution midway through the simulation and (b) the final mapping of damage.

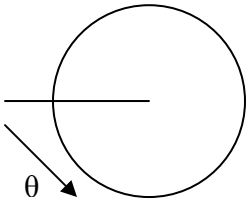

Figure 5.7 The damage and angle were obtained from the boundary of the exclusion region by revolving counter-clockwise beginning at the crack.

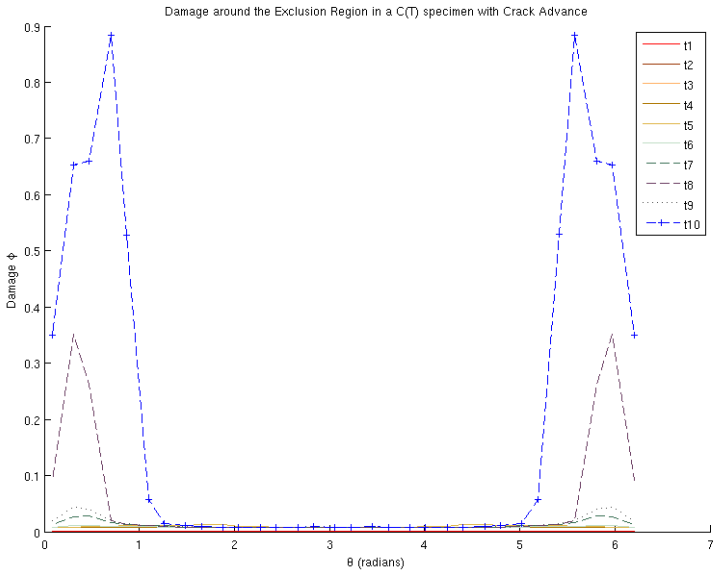

Figure 5.8 Damage as function of angle around the exclusion region at times t1-t10.

Consider the tension specimen with an edge crack where there is strictly mode I loading present and mixed-mode tension specimen shown in Figure 5.9. The material behavior was described by a linear isotropic hardening flow rule using J_2 plasticity with no damage present. Because it has been shown the plastic strain accumulates behind the crack tip and consequently the damage accumulates in the same place, the stress and strain fields were investigated to see if a component existed that predicted the advance direction. Simulations were performed for a stationary crack, and the fields were retrieved after approximately three percent of effective plastic strain had accumulated. The values of the fields were retrieved from the elements on the boundary of the exclusion region. Normal and tangential values of stress and strain refer to the angle with respect to the crack tip.

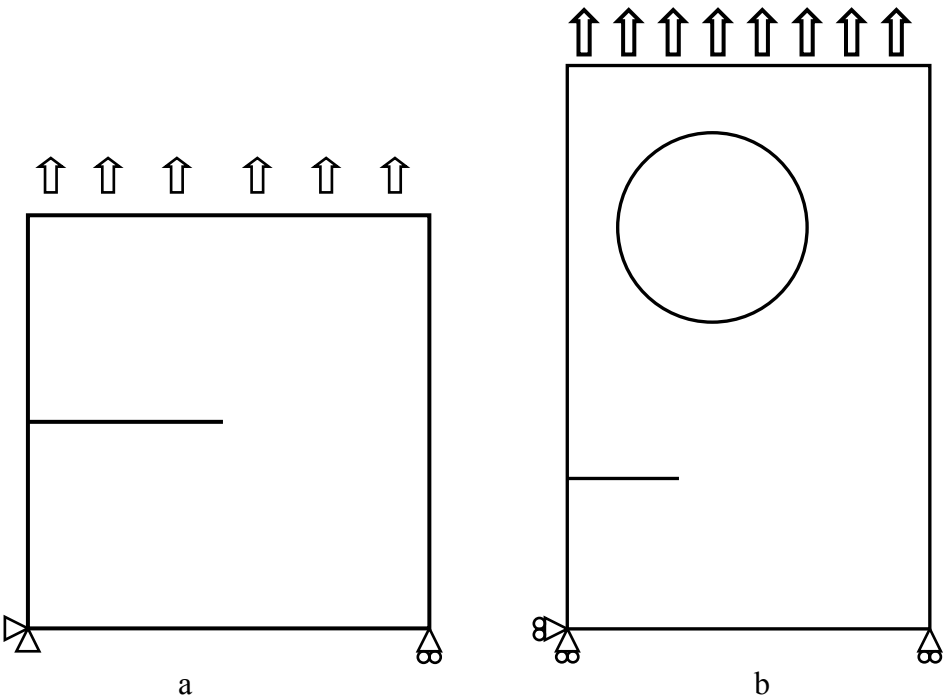

Figure 5.9 (a) Geometry and loading scenario for mode-I simulations. (b) Geometry and loading for mixed-mode simulations.

Mode-I Specimen

The results for the mode-I specimen are contained in Figures 5.10-5.14. The accepted direction for crack advance is represented in all figures by a dash-dot black line for reference. Figure 5.10 shows measures of stress as well as common factors used to describe the behavior of a material. The important thing to note from Figure 5.10 is that only one field, tangential stress, reached its maximum value at the correct angle. The stress fields in Figure 5.10 were additionally analyzed to determine if a meaningful ratio of them existed that reached a maximum value at the correct angle. The stress ratios are in Figure 5.11, and it can be seen that the ratio of the minimum and maximum principal stresses as well as the ratio of tangential stress and the von Mises stress have desirable behavior. Figure 5.12 presents the standard measures of strain from the elements surrounding the exclusion region. Figure 5.12 also contains the values of dilatation and incremental dilatation where dilatation is the trace of the strain tensor. Because a great range exists in the values, a closer look in the region of interest is shown in Figure 5.13. It can be seen that in Figure 5.13 only one measure of strain, tangential strain, has a maximum value in the correct direction. Only one ratio of the strain fields, the absolute value of the maximum and minimum principal values of strain, was found to have a maximum in the correct direction and is shown in Figure 5.14.

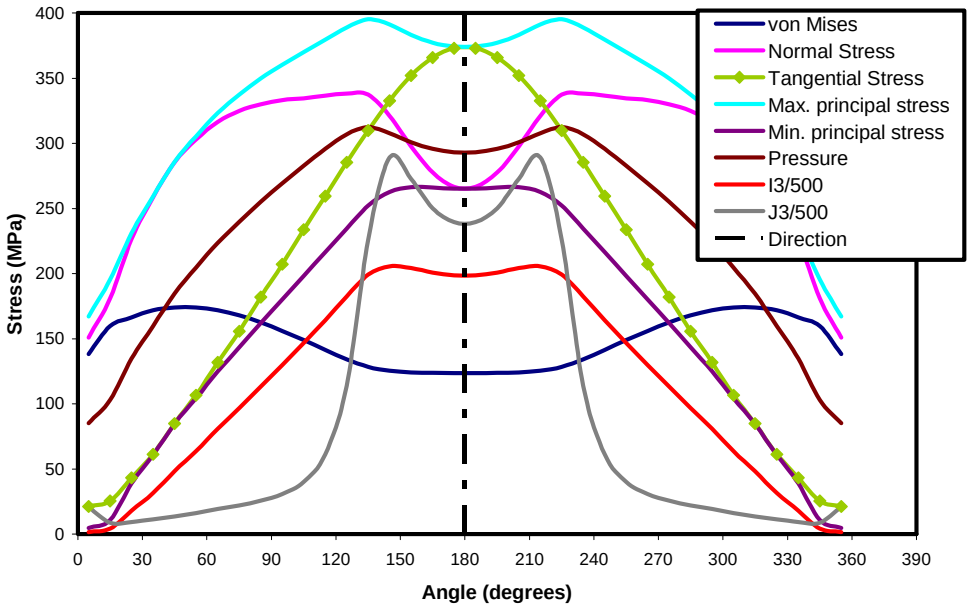

Figure 5.10 Stress fields compared with the known crack advance direction for a mode-I loading edge crack specimen using a J_2 plasticity model.

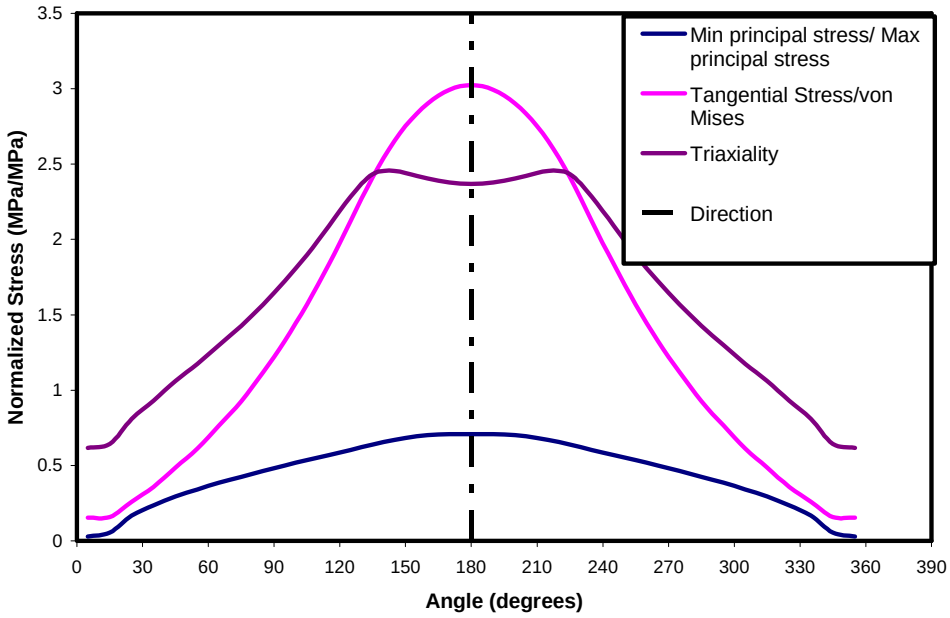

Figure 5.11 Various stress ratios compared with the known crack advance direction for a mode-I loading edge crack specimen using a J_2 plasticity model.

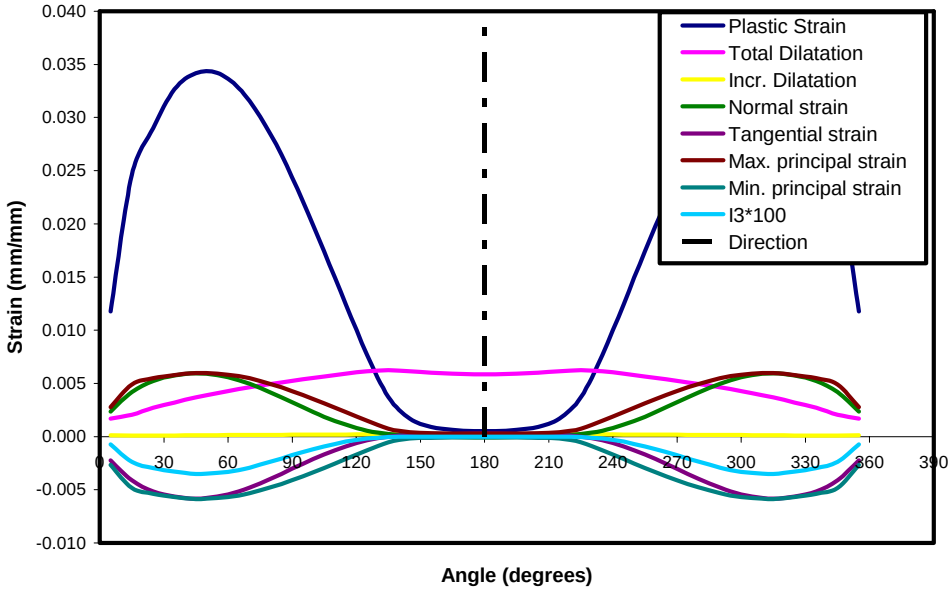

Figure 5.12 Strain fields compared with the known crack advance direction for a mode-I loading edge crack specimen using a J_2 plasticity model.

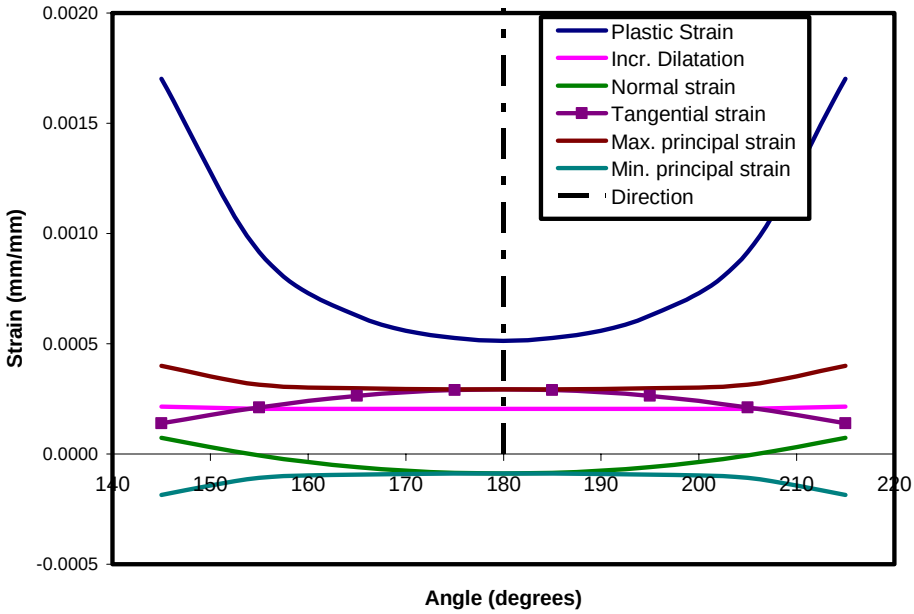

Figure 5.13 A closer view of strain fields compared with the known crack advance direction for a mode-I loading edge crack specimen using a J_2 plasticity model.

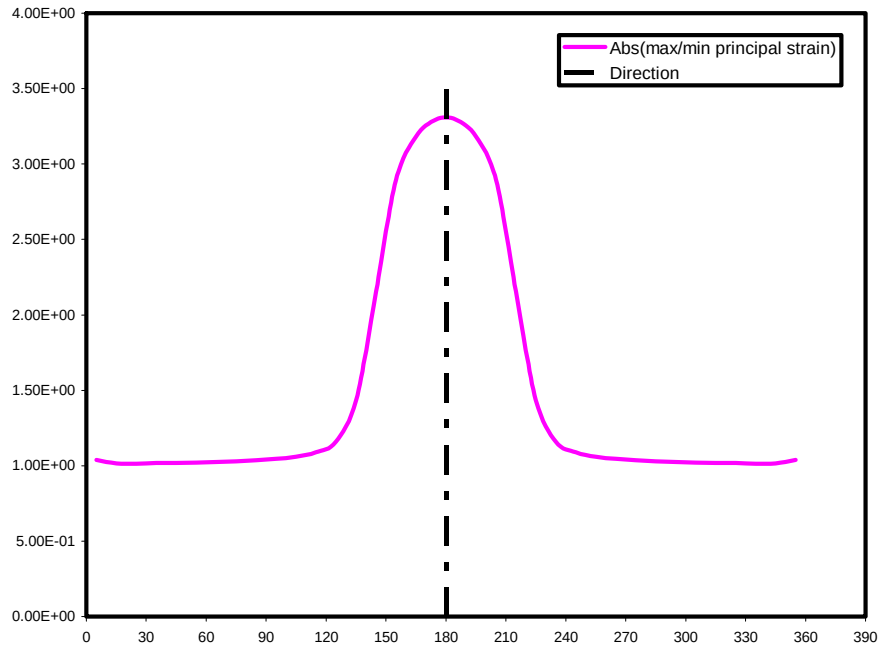

Figure 5.14 The ratio of the maximum principal strain to the minimum principal strain compared with the known crack advance direction for a mode-I loading edge crack specimen using a J_2 plasticity model.

Mixed-mode Specimen

The results for the mixed-mode specimen are contained in Figures 5.15-5.19. The accepted direction for crack advance is represented in all figures by a dash-dot black line for reference. There is an absence in the literature of monotonic fracture experiments with mixed-mode loading conditions. Due to this absence an experimental crack path could not be found for a simple geometry. The method used to determine the "true" direction of crack advance for this comparison is the direction of advance that maximized the normal opening stress around the crack tip region. Figure 5.15 shows measures of stress as well as common factors used to describe the behavior of a material. Similar to the mode-I results, Figure 5.15 shows that only one field, the tangential stress, reached its maximum value at the correct angle. The tangential stress field's behavior gives some

credence to the "true" direction calculation. Again the stress fields were analyzed to determine if a meaningful ratio of them existed that reached a maximum value at the correct angle. The stress ratios are in Figure 5.16, and it can be seen that none of the ratios that worked for mode-I loading could predict the angle of advance. Figure 5.17 presents the standard measures of strain from the elements surrounding the exclusion region with Figure 5.18 giving a closer look in the region of interest. As in Figure 5.16, Figure 5.18 reveals that none of the measures of strain have a maximum value in the correct direction. Figure 5.19 also shows the ratio of the maximum and minimum principal values does not align with the correct direction.

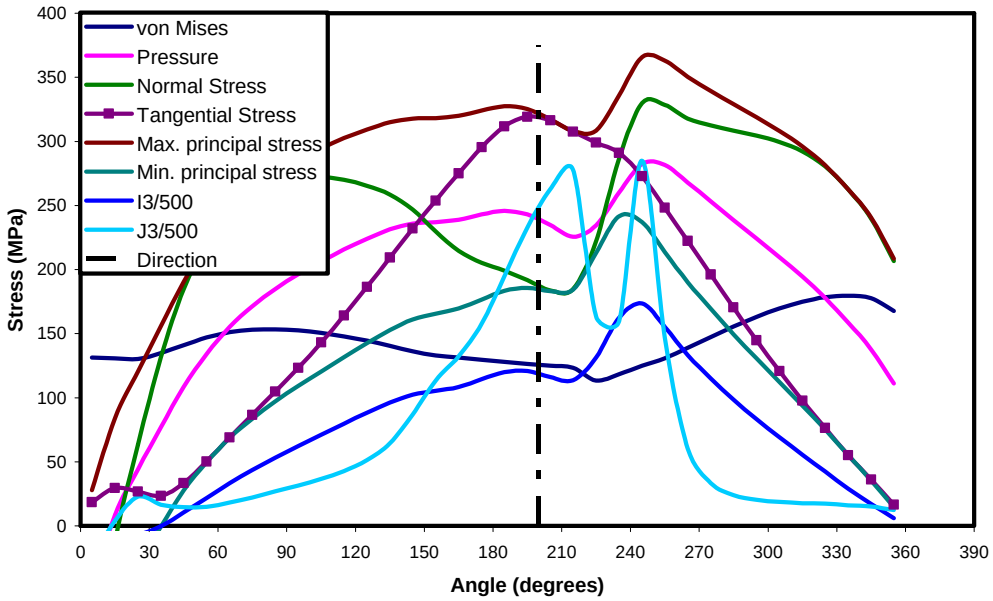

Figure 5.15 Stress fields compared with the known crack advance direction for a mixed-mode loading edge crack specimen using a J_2 plasticity model.

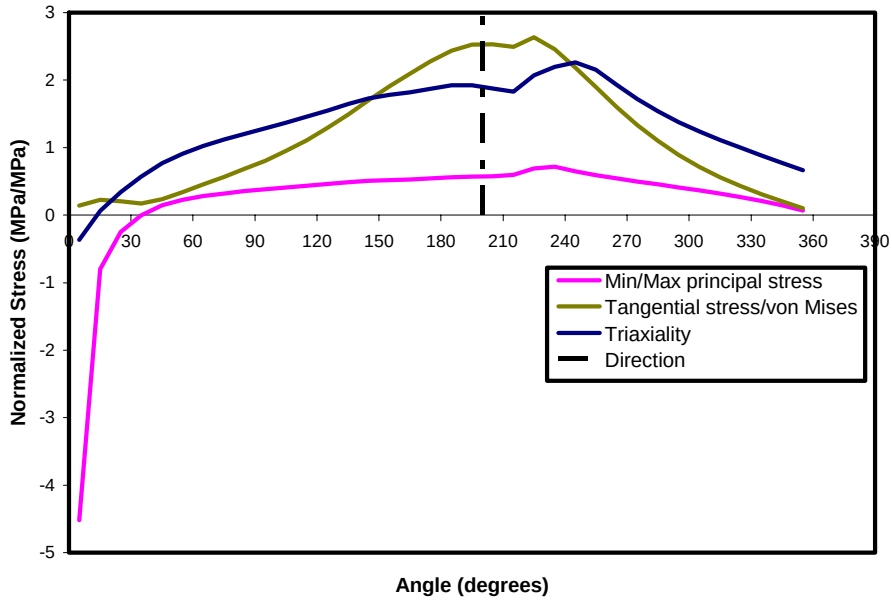

Figure 5.16 Various stress ratios compared with the known crack advance direction for a mixed-mode loading edge crack specimen using a J_2 plasticity model.

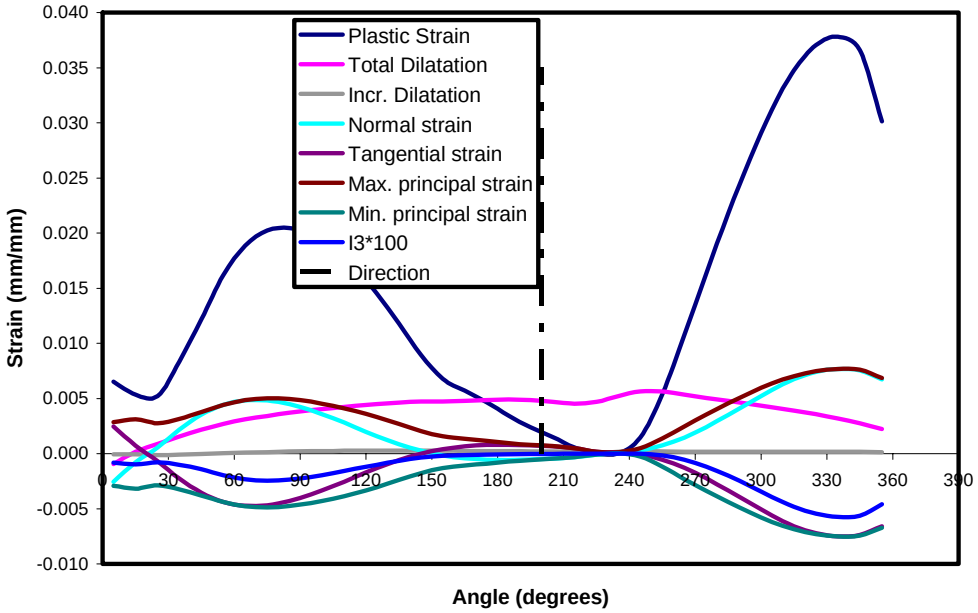

Figure 5.17 Strain fields compared with the known crack advance direction for a mixed-mode loading edge crack specimen using a J_2 plasticity model.

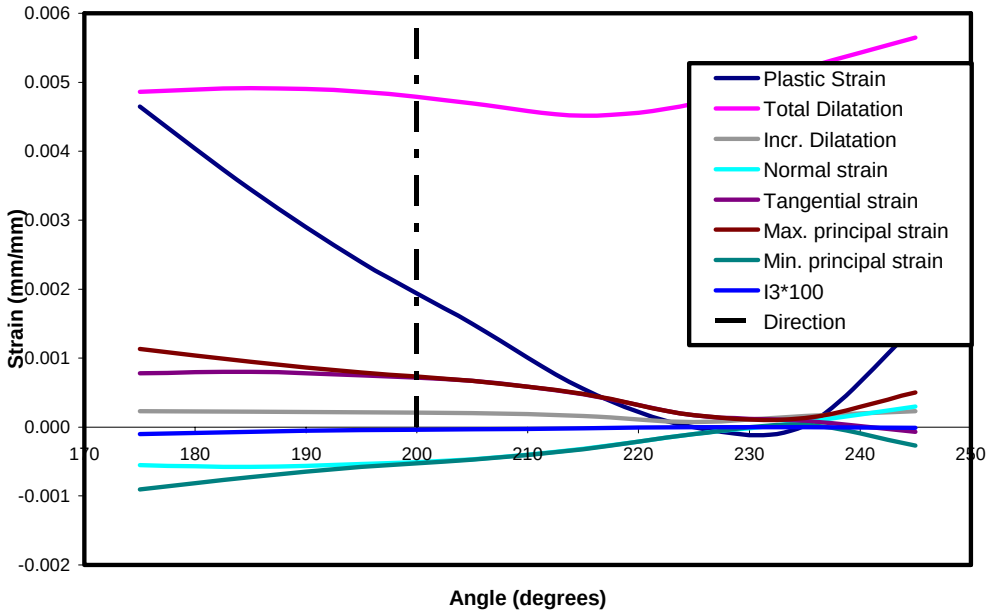

Figure 5.18 A closer view of strain fields compared with the known crack advance direction for a mixed-mode loading edge crack specimen using a J_2 plasticity model.

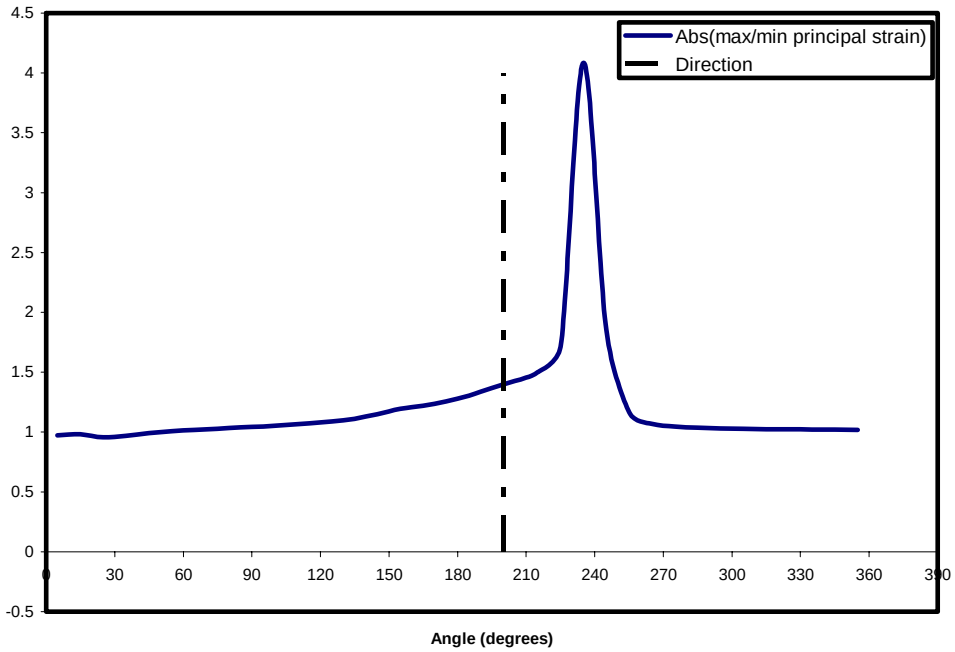

Figure 5.19 The ratio of the maximum principal strain to the minimum principal strain compared with the known crack advance direction for a mixed-mode loading edge crack specimen using a J_2 plasticity model.

It has been shown that the only parameter that exists in simulating ductile fracture is the tangential stress to predict the correct direction of crack advance for mode-I loading and mixed-mode loading of a non-blunting crack tip within the context of J_2 plasticity. The next section presents a two parameter method that uses damage to predict fracture.

Two Parameter Crack Advance

An intermediate step is to use the damage to determine when the crack will grow and define another parameter that is used to find the direction of advance. The linear elastic concepts maximum hoop stress, minimum strain energy density, and maximum energy release rate, are all possibilities for this parameter. Pirondi and Dalle Donne (2001) performed mixed mode experiments and concluded that cracks propagate in the direction of maximum tangential stress or the maximum shear strain depending on the mode of loading. Mediavilla et. al. (2006a) proposed a criterion based on these results which is a weighted relationship between maximum hoop stress, $\tau_{\theta\theta}(\theta)$, and maximum tangential stress, $\tau_{r\theta}(\theta)$,

$$\tau_m(\theta) = \max\left\{\left\langle(1-\alpha)\tau_{\theta\theta}(\theta)\right\rangle, \alpha\left|\tau_{r\theta}(\theta)\right|\right\},\ 0 \le \alpha \le 1. \tag{5.1}$$

The weight, α, is determined from experiments that indicate the transition from shear to tension crack growth. Mediavilla et. al. (2006b) averaged the angles where the maximum damage occurs to get a direction. Averaging the angles gave excellent results predicting direction for symmetric geometries, symmetric loading conditions, and a uniform initial damage field. Mediavilla et. al. (2006b) were able to predict a reasonable crack path from the maximum damage value location for shear only loading conditions, and note

that their method would not work in a state of tension where void growth contributes to crack advance.

Calculating the critical value of damage in the vicinity of the crack tip is somewhat nontrivial. One problem in local fracture simulations it is possible to have a narrow band of damage and the location of the band is mesh dependent. If the damage is uncoupled from the material strength, the localization of damage can be prevented. In the uncoupled approach, the damage does not affect the material until it reaches the critical value that causes crack advance. The maximum value of damage occurring in multiple places makes it nontrivial to determine the value of damage to use for crack advance. One method is to take a small area in the vicinity of the crack tip and use the average value for the region as the critical damage value. Mediavilla et. al. (2006a; 2006b) used a semi-circle in front of the crack tip that extended through at least three elements for their critical area. The method used for the purposes of this research is to average the values in the circular exclusion region. These methods are considered nonlocal approaches to the damage value.

The equations that are commonly used to model damage mechanisms that cause fracture need to be investigated for their suitability of predicting fracture in front of an existing macro-crack. Hom and McMeeking (1989) investigated the effect of a crack on void growth for small scale yielding. They explicitly modeled a void and a crack varying the distance between the two. They found that the void growth rate is double that of Rice and Tracey (1969) when the void is in front of a crack tip. Their result also showed that the voids cause the high hydrostatic stress field in front of the crack tip to

emanate further away. This provides further evidence that the existing damage equations are not giving realistic results when a crack tip is in the geometry.

Mode-I and mixed-mode simulations were run to show that the damage based crack advance works with the exclusion region theory. The mode-I and mixed-mode geometry and loading are shown in Figure 5.9a and 5.9b, respectively. The material response was modeled with J_2 plasticity based linear isotropic hardening. The initial damage field was chosen to be uniformly assigned a value of 0.01. The separation criterion used for these simulations is

$$\Phi = \frac{\overline{F_n}}{\pi r^2}\int_{ER}\phi da\,,\ \overline{F_n} = \frac{\langle F_n \rangle}{\sup\{F_n\}},\ \ F_n = \int_{\psi}^{\pi}\mathbf{t}(\theta)\cdot\hat{\mathbf{m}}rd\theta \tag{5.2}$$

where **m**= (-sin (ψ), cos (ψ)) is the unit vector tangent to the proposed direction of advance, r is the exclusion region radius, and ϕ is the damage value at the integration point. F_n is the normal opening force acting on the boundary of the exclusion region with respect to the direction of advance. The magnitude of the separation function is the average of the damage values in the exclusion region, while the direction of advance is taken from $\overline{F_n}$. It is necessary to use something other than damage for direction since the material model is not capable of capturing the true mechanisms which are occurring. The averaging technique is a nonlocal damage evaluation near the crack tip. The damage evolution equation used for the uniform damage simulations is from Goijaerts et. al. (2001)

$$\dot{\phi} = \frac{1}{C}\left\langle 1 + A\frac{\sigma_H}{\sigma_{vm}}\right\rangle\dot{\varepsilon}_p \tag{5.3}$$

where σ_H is the hydrostatic stress, σ_{vm} is the von Mises stress, C controls the onset of fracture, and A controls the effect the triaxiality has on the void volume fraction growth. The simulations were run with the damage affecting and not affecting the material. Regardless of the evolution equation they both gave similar results since the direction is not affected by the damage. The critical value of the separation function was assigned a value of 0.05.

Mode-I simulation results show that the crack does in fact grow as one would expect, straight ahead in Figure 5.20b. The damage evolved perpendicular to the known crack path as expected prior to crack growth, Figure 5.20a. Similarly for the mixed-mode simulation the damage prior to crack advance is accumulating where the kink will occur, Figure 5.21a, and not in the direction the crack will grow as shown in Figure 5.21b.

Using the damage for the advancement criterion and normal opening force for direction gives realistic results. The results show that this computational framework is capable of using damage evolution and accumulation to determine crack advance. Modifications to the traditional J_2 plasticity used in these simulations are presented next in an attempt to capture damage evolution in front of the crack tip.

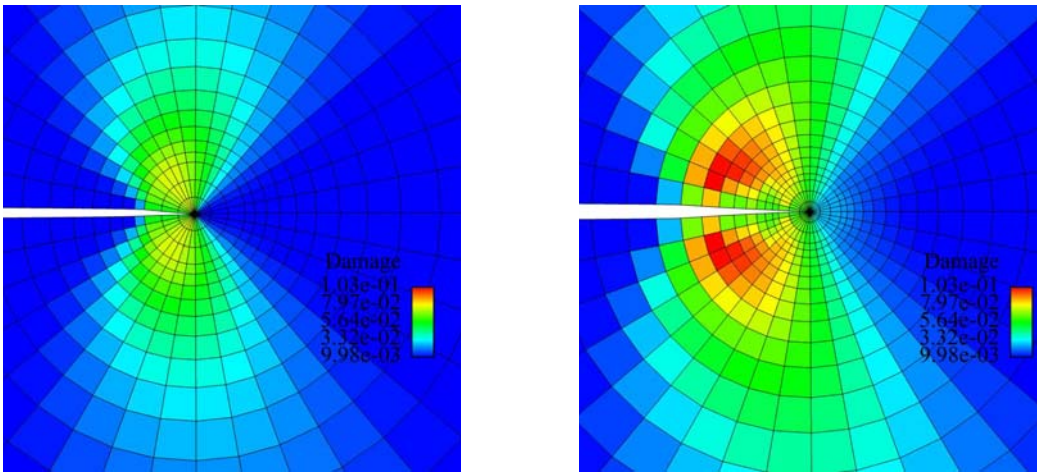

a b

Figure 5.20 (a) Mode-I damage field prior to crack advance. (b) Mode-I damage field after crack has advance.

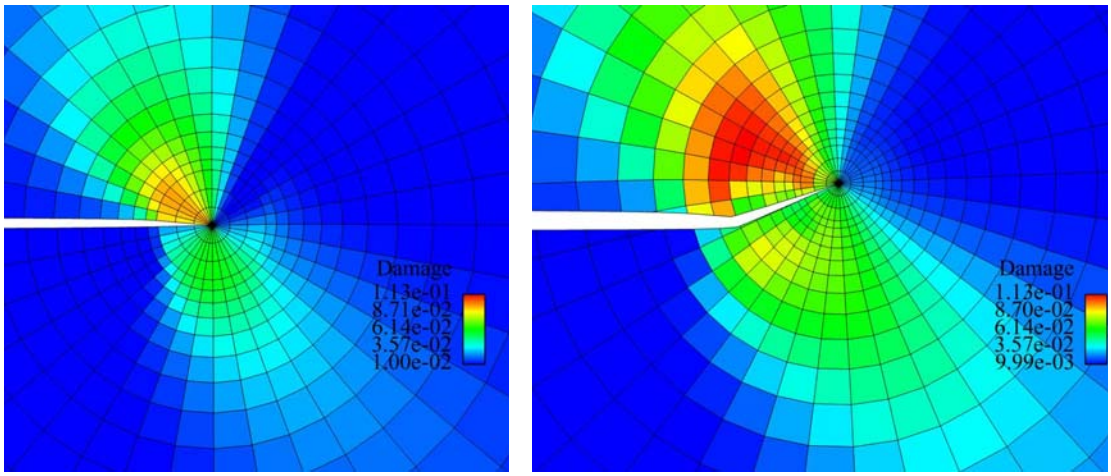

a b

Figure 5.21 (a) Mixed-mode damage field prior to crack advance. (b) Mixed-mode damage field after crack has advance.

Modified J_2 Plasticity

To motivate modifying J_2 plasticity, a unit cube was considered and subjected to a hydrostatic load as shown in Figure 5.22. According to J_2 based plasticity, the material will never yield because J_2 is deviatoric and no deviatoric component exists in this

loading scenario. Now consider a void subjected to the same loading scenario as shown in Figure 5.23. Figure 5.23 shows the resulting plastic strain when using the same material model. Thus, when an explicit void was subjected to a hydrostatic stress state, the material yielded as one would expect. But, if one were to represent the void implicitly as a void volume fraction parameter in a unit cube, the same plastic strain would never be realized. Referring to Figure 5.1, a crack in ductile materials with particles and oxides present would grow as the figure indicates. Therefore even though the plastic strain is occurring around the voids, it is not possible to achieve the same strain field unless the voids are explicitly modeled in the finite element simulation. Obviously that is impractical and would exhaust any computational resources as well as limit the size of simulated geometries.

While many J_2 based constitutive models exist that haven been proven to predict failure of large systems, it has been shown that they are not capable of capturing the evolution of damage in front of a crack. It has also been shown that there are situations where an explicit void representation results in accumulated plastic strain and with a smeared void representation there is no plastic strain. The area in front of a crack tip is considered to also be one of those regions. Experimental evidence supports that mode-I loading will make the crack tend to propagate straight ahead resulting from the nucleation and growth of voids preceding the crack tip. Because it is not computationally efficient to model all pre-existing voids, a smeared void volume fraction is the desired approach. The next two variants of J_2 plasticity are attempts to capture the damage evolution in front of the crack in as simple a manner as possible.

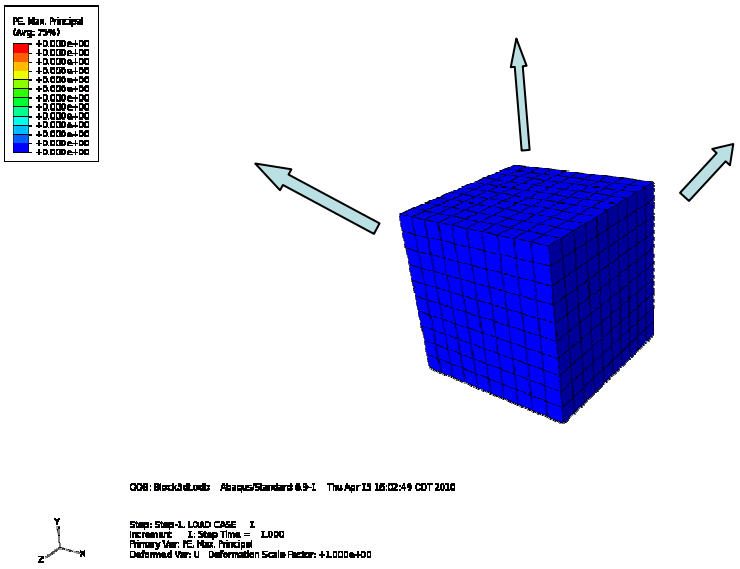

Figure 5.22 A unit cube being subjected to a hydrostatic load.

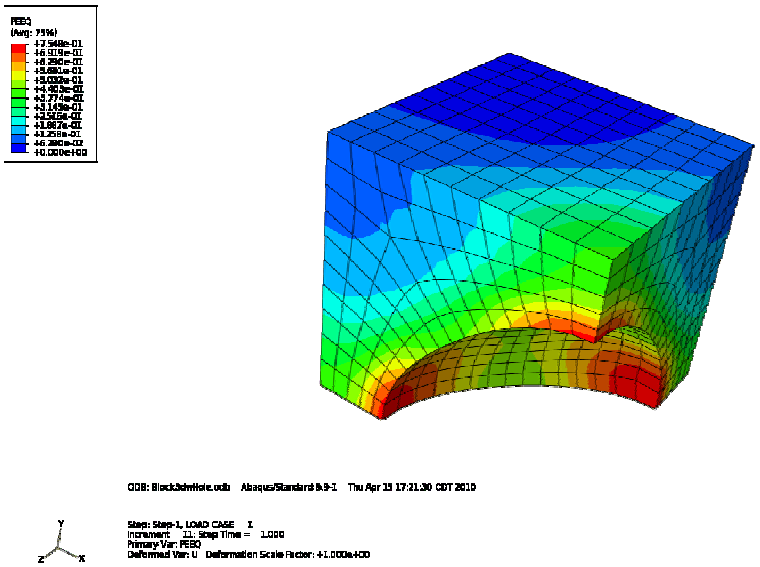

Figure 5.23 A spherical void subjected to a hydrostatic load.

Pressure Method I

It was shown that hydrostatic pressure applied to a void will cause void growth and plastic strain to occur. Noting the area preceding the crack tip has a high pressure value, the method of crack advance in ductile materials shown in Figure 5.1, and the lack of plastic strain indicated by J_2 plasticity in this region, a criterion for damage evolution related to the pressure field is postulated.

A yield condition for the hydrostatic stress was formulated as

$$f(\underline{\sigma}) \le \sigma_p^y + H_d \left\| \underline{\Delta\varepsilon}_d^p \right\| - H_p \left\| \underline{\Delta\varepsilon}_p^p \right\| \tag{5.4}$$

where at step N

$$f(\underline{\sigma}_N) = Tr(\underline{\sigma}_N) = Tr(\underline{\sigma}_N^{tr}) = Tr(\underline{\sigma}_{N-1}) + 3K \cdot Tr(\underline{\Delta\varepsilon}), \tag{5.5}$$

H is the slope of the hardening curve where subscripts d and p denote the deviatoric and volumetric response, and superscript p denotes plastic strain. The material is determined to yield once the pressure reaches a critical value, σ_p^y. There is no enforcement of consistency as in the J_2 plasticity theory. Instead, once the pressure reaches this critical value, the dilatation is determined to be purely plastic. The yield value must be affected by the deviatoric hardening and is the reason for the second term on the right had side of inequality (5.4). The critical value σ_p^y was set initially to a large value to prevent the yield from occurring where there is strong deviatoric response. If hardening were determined to occur in the von Mises flow rule, then the resulting plastic strain contribution elevates the value of the yield pressure making it more difficult to yield hydrostatically. Once yielding is determined to occur hydrostatically, the dilatation is used to reduce the hydrostatic yield making it easier for the material to yield in a

hydrostatic manner. Thus, there are two competing mechanisms that occur which result in focusing the hydrostatic yielding material in a high pressure area absent of deviatoric plastic strain. It is important to note the smaller the resulting hydrostatic yield, the more hydrostatic yielding is taking place. This is reverse of the deviatoric flow rule where the largest von Mises stress would indicate the most yielding.

The method above was implemented in the finite element fracture propagation program, FEFRAC. A mode-I edge crack simulation, Figure 5.9a, was performed. The formulation for the J_2 plasticity was not changed and as a result the stress and strain fields are the same as in Figures 5.10-5.15. The new hydrostatic yield and volumetric plastic strain values are shown in Figure 5.24 and Figure 5.25 for the elements surrounding the exclusion region. The hydrostatic yield is denoted in Figure 5.24 by HY and has the desired behavior of the minimum hydrostatic yield occurring at 180 degrees. The trace of plastic strain has a maximum at 135 and 225 degrees. If one were to insert a uniform damage field into the simulation and drive the damage by the volumetric strain, the largest damage value would be located at the maximum strain location. Figure 5.25 shows that the volumetric plastic strain would predict a direction of $\pm$ 45 degrees which is an improvement from the deviatoric plastic strain driven damage. Figure 5.26 shows a new stress ratio similar to triaxiality that uses the hydrostatic yield value instead of the pressure. Triaxiality has often been used as a growth term for voids. Once a material yields deviatorically the yield stress is equivalent to the value of the von Mises stress so the triaxiality could be thought of the ratio of pressure and the deviatoric yield. Now that a yield condition has been introduced for the hydrostatic component and the behavior of the condition is reverse of the von Mises value, a new ratio of the von Mises stress and

the hydrostatic yield is investigated and its behavior is compared to ratios that were in Figure 5.11. The new ratio has good agreement with the accepted direction of crack advance. The ratio is multiplied by a constant so it could be displayed against the other ratios, and the multiplication does not affect the behavior of the ratio.

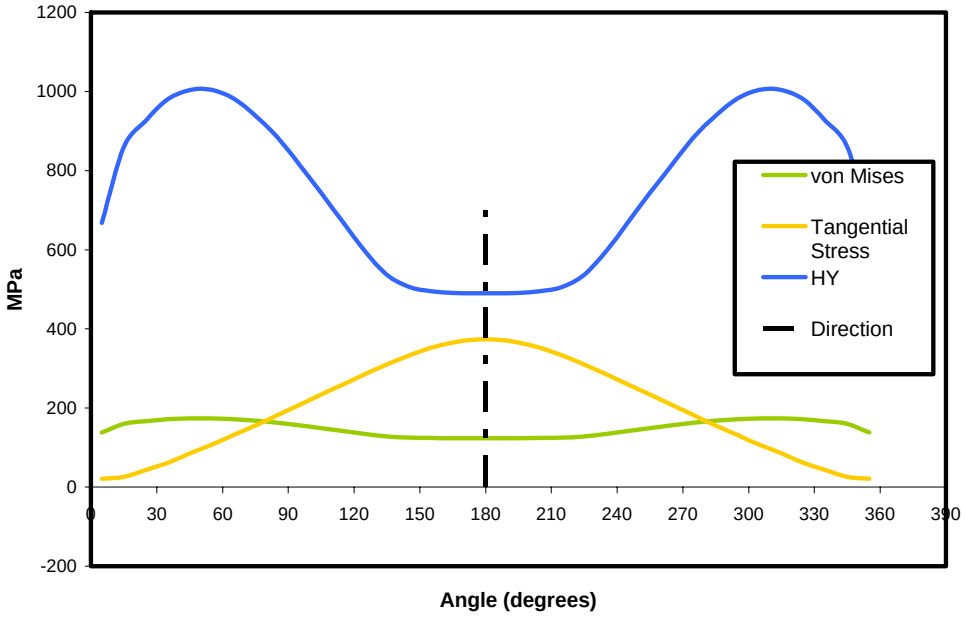

Figure 5.24 Stress fields compared with the known crack advance direction for a mode-I loading edge crack specimen using a J_2 plasticity model in addition to a hydrostatic yield condition.

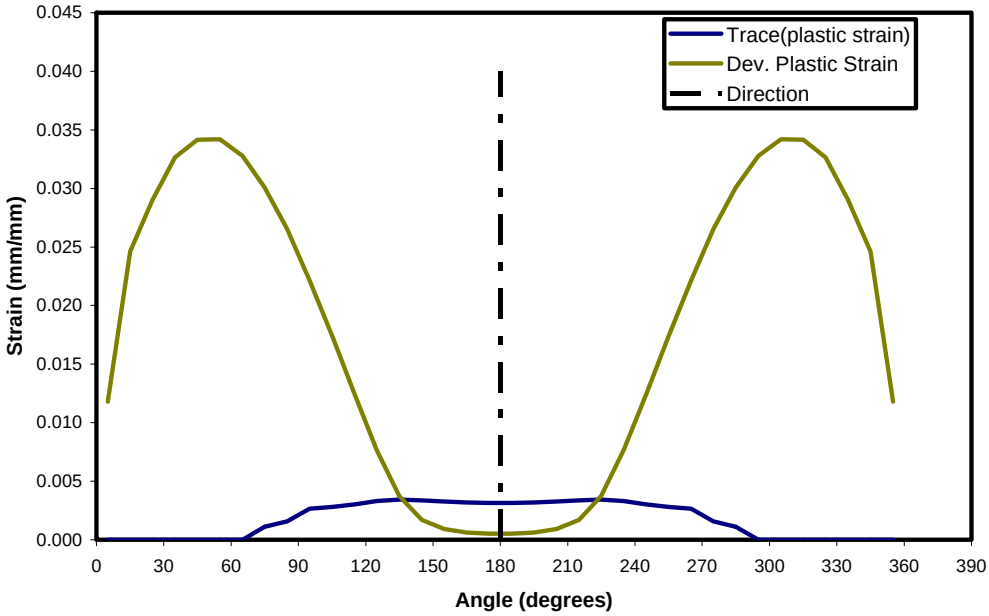

Figure 5.25 Strain fields compared with the known crack advance direction for a mode-I loading edge crack specimen using a J_2 plasticity model in addition to a hydrostatic yield condition.

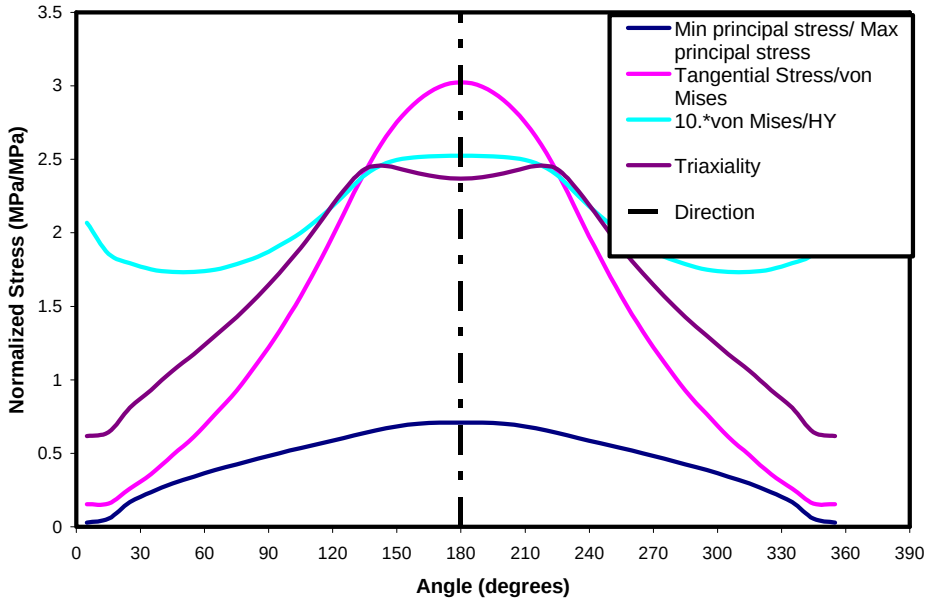

Figure 5.26 Various stress ratios compared with the known crack advance direction for a mode-I loading edge crack specimen using a J_2 plasticity model in addition to a hydrostatic yield condition.

The mixed-mode simulation, Figure 5.9b, was performed using the hydrostatic yield condition and the new fields are shown with preexisting fields for comparison in Figures 5.27-5.29. The hydrostatic yield denoted by HY in Figure 5.27 does not align with what is considered to be the correct direction like it did for the mode-I simulation. Figure 5.28 shows the magnitude of the deviatoric and volumetric plastic strain and that neither would indicate the desired direction. The maximum for the volumetric plastic strain is fifty degrees off and the minimum deviatoric plastic strain is twenty degrees off. Figure 5.29 shows several stress ratios and the behavior of the new ratio of the von Mises stress and the hydrostatic yield. The new ratio's maximum is approximately ten degrees away from the correct angle, and shows the most promise to be a good measure of damage evolution that could predict the correct crack advance direction.

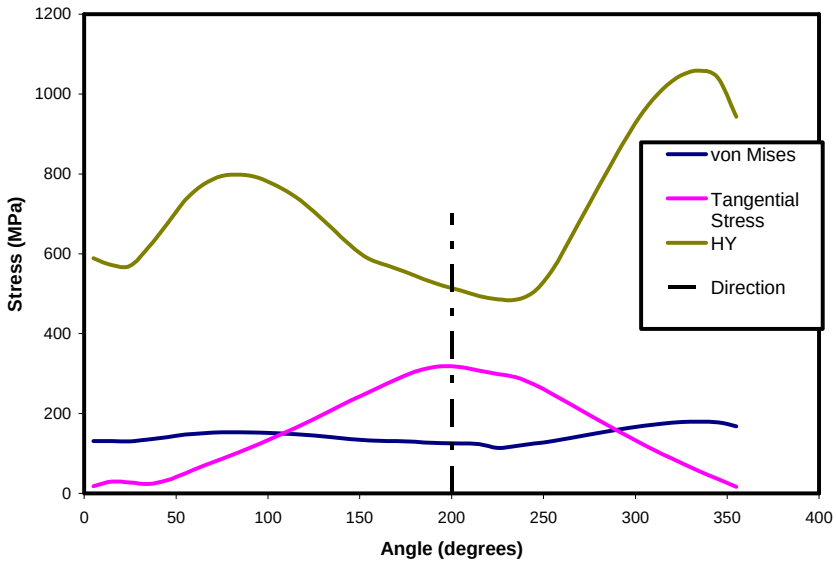

Figure 5.27 Stress fields compared with the known crack advance direction for a mixed-mode loading edge crack specimen using a J_2 plasticity model in addition to a hydrostatic yield condition.

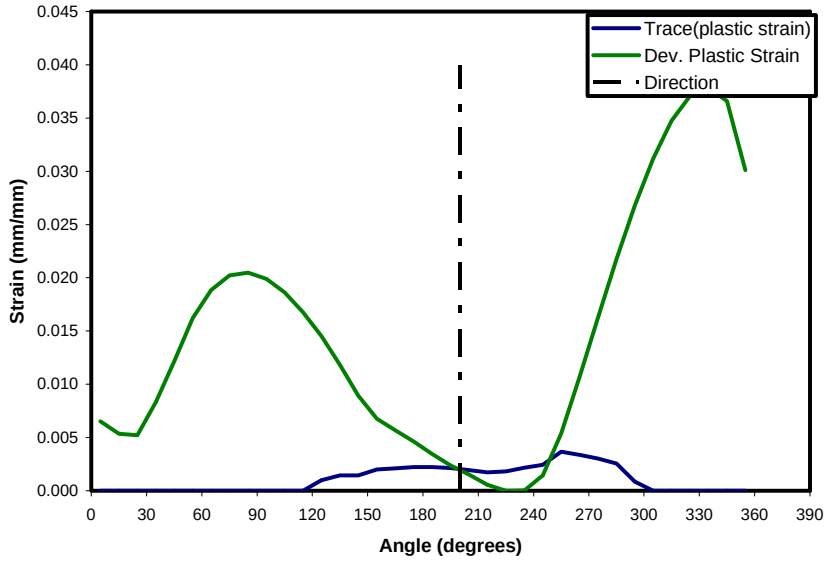

Figure 5.28 Strain fields compared with the known crack advance direction for a mixed-mode loading edge crack specimen using a J_2 plasticity model in addition to a hydrostatic yield condition.

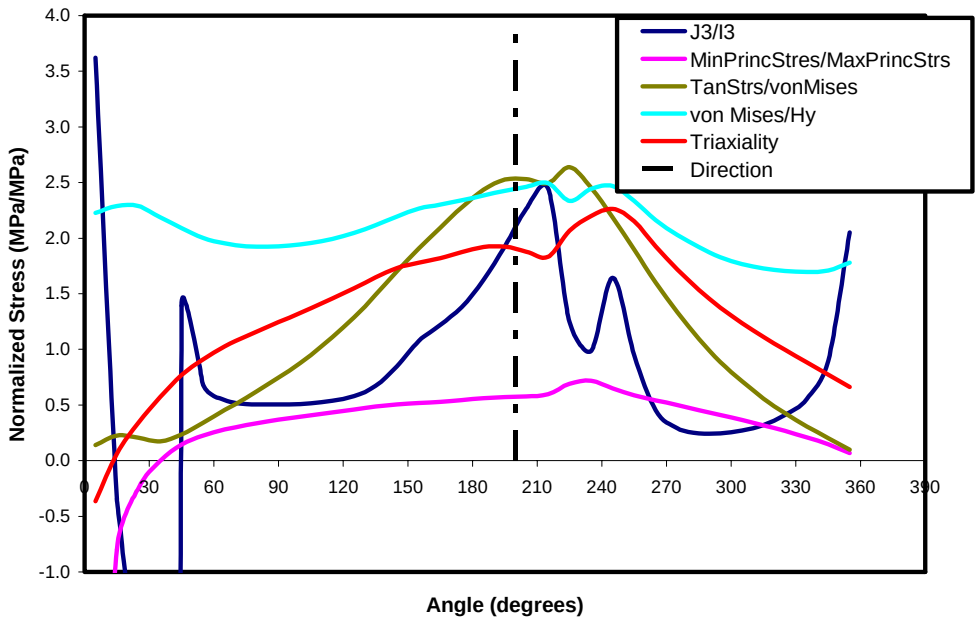

Figure 5.29 Various stress ratios compared with the known crack advance direction for a mixed-mode loading edge crack specimen using a J_2 plasticity model in addition to a hydrostatic yield condition.

The pressure yield condition introduced in this section creates two new parameters, a hydrostatic yield value and volumetric plastic strain. For mode-I simulations, it has been shown that both fields could lead to better predictive capabilities than J_2 plasticity damage evolution. For mixed-mode simulations, only the ratio of the von Mises stress and the hydrostatic yield value was found to closely represent the correct crack advance direction. The next section enforces the consistency condition and whether or not the consistency condition gives better predictive capabilities for crack advance direction.

Pressure Method II

The second method uses the hydrostatic yield condition from the first method but the consistency condition is enforced. The resulting volumetric plastic strain would be considered the damage variable and could also be thought of void growth in the material. The hydrostatic pressure is now in predictor-corrector form which implies that the relationship between the pressure and volumetric strain changes once the critical value of pressure is reached. The change in the pressure-volumetric relationship is motivated by Hom and McMeeking (1989) who analyzed crack-void interactions and analyzed the pressure field preceding a crack tip absent of a void and with the void in front of the crack tip. They found that the void actually caused the pressure to decrease between the void and the crack. Nemat-Nasser and Taya (1980) investigated void growth and concluded that the localized shear deformations that occur between voids would cause the macroscopic response to be plastically compressible. Based on these investigations it is a reasonable assumption in the absence of explicit damage representation to postulate the

material preceding the crack tip could become compressible and as a result affect the pressure-volumetric strain relationship.

The development of the modified pressure dependent yield is presented in full detail. As in the J_2 theory, the elastic predictor-corrector methodology is used. The elastic stress-strain relationship is assumed

$$\underline{\sigma}_{N+1} = \underline{\underline{C}} : \underline{\varepsilon}^{e}_{N+1} = 2G\underline{\varepsilon}^{e}_{N+1} + \lambda TR\left(\underline{\varepsilon}^{e}_{N+1}\right)\underline{I} \tag{5.6}$$

where $\underline{\underline{C}}$ is a fourth order tensor of elastic constants, G and λ are the shear modulus and Lame parameter, and the elastic strain tensor is represented by

$$\underline{\varepsilon}^{e}_{N+1} = \underline{\varepsilon}_{N} + \underline{\Delta\varepsilon}^{e} = \underline{\varepsilon}_{N} + \underline{\Delta\varepsilon}_{N+1} - \underline{\Delta\varepsilon}^{p}. \tag{5.7}$$

Substituting for the strain increment results in

$$\begin{aligned} \underline{\sigma}_{N+1} &= 2G\left(\underline{\varepsilon}_{N} + \underline{\Delta\varepsilon}_{N+1}\right) + \lambda TR\left(\underline{\varepsilon}_{N} + \underline{\Delta\varepsilon}_{N+1}\right)\underline{I} - 2G\underline{\Delta\varepsilon}^{p} - \lambda TR\left(\underline{\Delta\varepsilon}^{p}\right)\underline{I} \\ &= \underline{\sigma}_{N} + 2G\left(\underline{\Delta\varepsilon}_{N+1}\right) + \lambda TR\left(\underline{\Delta\varepsilon}_{N+1}\right)\underline{I} - 2G\underline{\Delta\varepsilon}^{p} - \lambda TR\left(\underline{\Delta\varepsilon}^{p}\right)\underline{I} \end{aligned} \tag{5.8}$$

The sum of the first three terms is the elastic predictor and is typically called a trial stress

$$\underline{\sigma}^{TR}_{N+1} = \underline{\sigma}_{N} + 2G\left(\underline{\Delta\varepsilon}_{N+1}\right) + \lambda TR\left(\underline{\Delta\varepsilon}_{N+1}\right)\underline{I} \tag{5.9}$$

while the last two terms are considered the plastic corrector. For normal J_2 flow theory the last term would not be present because the plastic strain is assumed to be strictly deviatoric and the trace of a deviatoric quantity is 0.0 .

Because it is assumed that the plastic strain has a volumetric component, the trace of the updated stress becomes

$$f\left(\underline{\sigma}_{N+1}\right) = Tr\left(\underline{\sigma}_{N+1}\right) = Tr\left(\underline{\sigma}^{tr}_{N+1}\right) - (2G + 3\lambda)Tr\left(\underline{\Delta\varepsilon}^{p}\right) = Tr\left(\underline{\sigma}^{tr}_{N+1}\right) - 3KTr\left(\underline{\Delta\varepsilon}^{p}\right) \tag{5.10}$$

where K is the bulk modulus of the material. The material is said to have yielded hydrostatically if

$$f(\underline{\sigma}) > \underline{\sigma}_p^y + H_d \left\| \underline{\Delta\varepsilon}_d^p \right\| - H_p \left\| \underline{\Delta\varepsilon}_p^p \right\| \tag{5.11}$$

and enforcing the consistency condition

$$f(\underline{\sigma}) - \left(\underline{\sigma}_p^y + H_d \left\| \underline{\Delta\varepsilon}_d^p \right\| - H_p \left\| \underline{\Delta\varepsilon}_p^p \right\| \right) = Tr\left(\underline{\sigma}_{N+1}^{tr} \right) - 3KTr\left(\underline{\Delta\varepsilon}^p \right) - \left(\underline{\sigma}_p^y + H_d \left\| \underline{\Delta\varepsilon}_d^p \right\| - H_p \left\| \underline{\Delta\varepsilon}_p^p \right\| \right) = 0 \tag{5.12}$$

resulted in

$$Tr\left(\Delta\varepsilon^p \right) = \frac{Tr\left(\underline{\sigma}_{N+1}^{tr} \right) - \left(\underline{\sigma}_p^y + H_d \left\| \underline{\Delta\varepsilon}_d^p \right\| \right)}{3K - H_p} \tag{5.13}$$

and

$$Tr\left(\underline{\sigma}_{N+1} \right) = \frac{3K\left(\underline{\sigma}_p^y + H_d \left\| \underline{\Delta\varepsilon}_d^p \right\| \right) - Tr\left(\underline{\sigma}_{N+1}^{tr} \right) H_p}{3K - H_p} . \tag{5.14}$$

The resulting tangent stiffness matrix is

$$\frac{\partial \sigma}{\partial \varepsilon} = \frac{-3G\sigma_d^y}{\left(1 + \frac{H_d}{3G} \right)} \cdot \underline{S}^{tr} \otimes \underline{S}^{tr} + F \cdot 2G \cdot \underline{\underline{I}}^{dev} + K\alpha \cdot \underline{I} \otimes \underline{I} \tag{5.15}$$

where

$$F = \begin{cases} 1.0 & \text{elastic} \\ \dfrac{H_d \overline{S}^{tr} + 3G\sigma_d^y}{\left(3G + H_d \right) \overline{S}^{tr}} & \text{deviatoric plastic} \end{cases} \tag{5.16}$$

and

$$\alpha = \begin{cases} 1.0 & \text{volumetrically elastic} \\ \dfrac{-H_p}{3K - H_p} & \text{volumetrically plastic} \end{cases} \tag{5.17}$$

The mode-I simulation in Figure 5.9a was used to determine the capability of the volumetric plastic strain as a measure of damage. The hydrostatic yield denoted by HY is

shown in Figure 5.30 and the plastic strain fields are shown in Figure 5.32. Because this method changes the trace of the stress, all of the stress fields will be different than the previous pressure method. Figure 5.30 shows the hydrostatic yield had a minimum and the tangential stress had a maximum at the correct angle. The stress ratios in Figure 5.31 show that the ratio of von Mises and hydrostatic yield was off by $\pm$45 degrees. The volumetric plastic strain's behavior is shown in Figure 5.32 and also was off by $\pm$45 degrees, but the behavior has better predictive capabilities than the deviatoric plastic strain. The tangential strain's maximum occurred at the correct angle of advance just as it has for all other mode-I simulations.

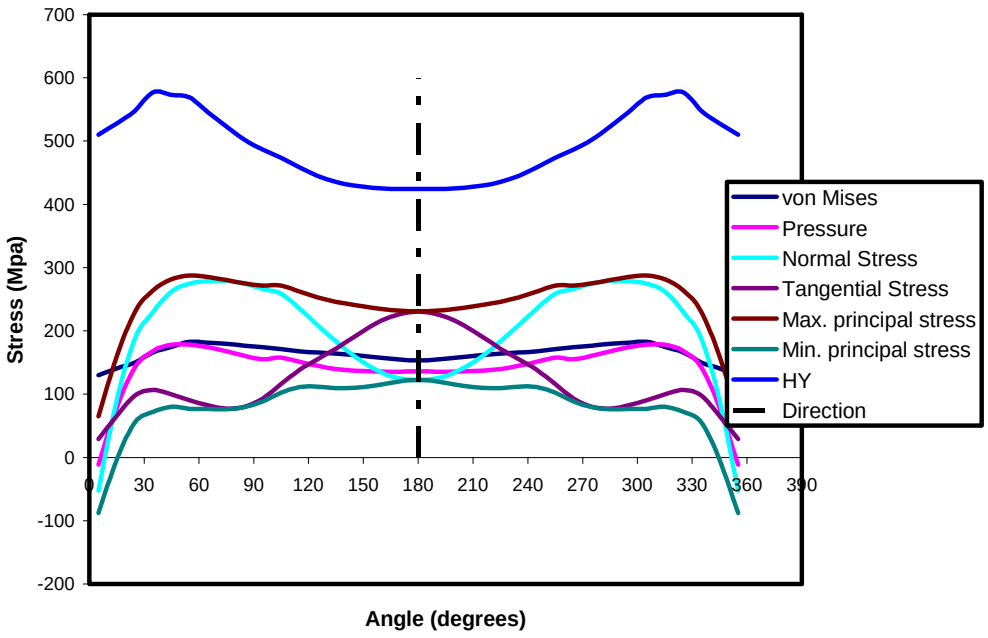

Figure 5.30 Stress fields compared with the known crack advance direction for a mode-I loading edge crack specimen using a J_2 plasticity model in addition to a hydrostatic yield condition with consistency condition enforced.

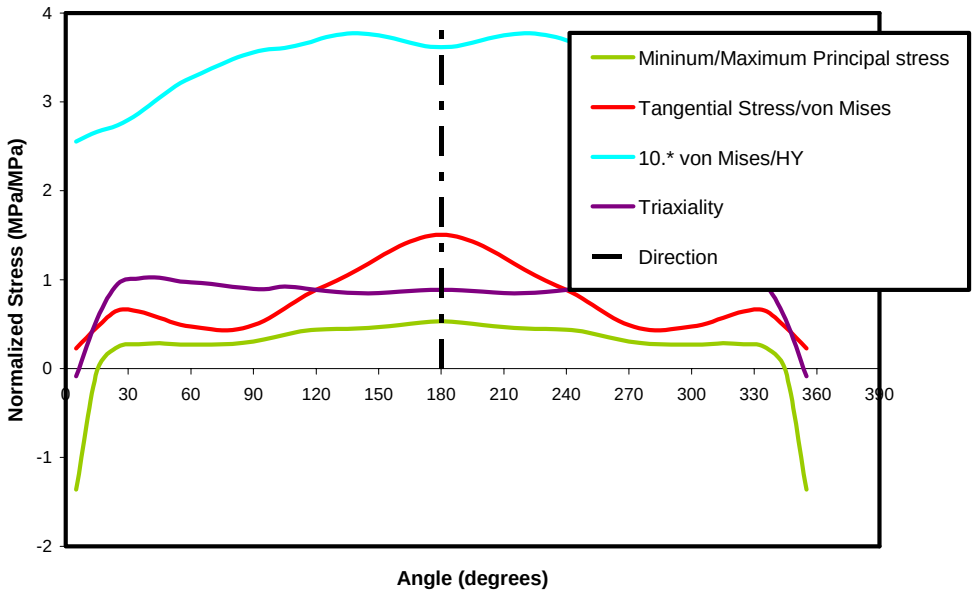

Figure 5.31 Various stress ratios compared with the known crack advance direction for a mode-I loading edge crack specimen using a J_2 plasticity model in addition to a hydrostatic yield condition with consistency condition enforced.

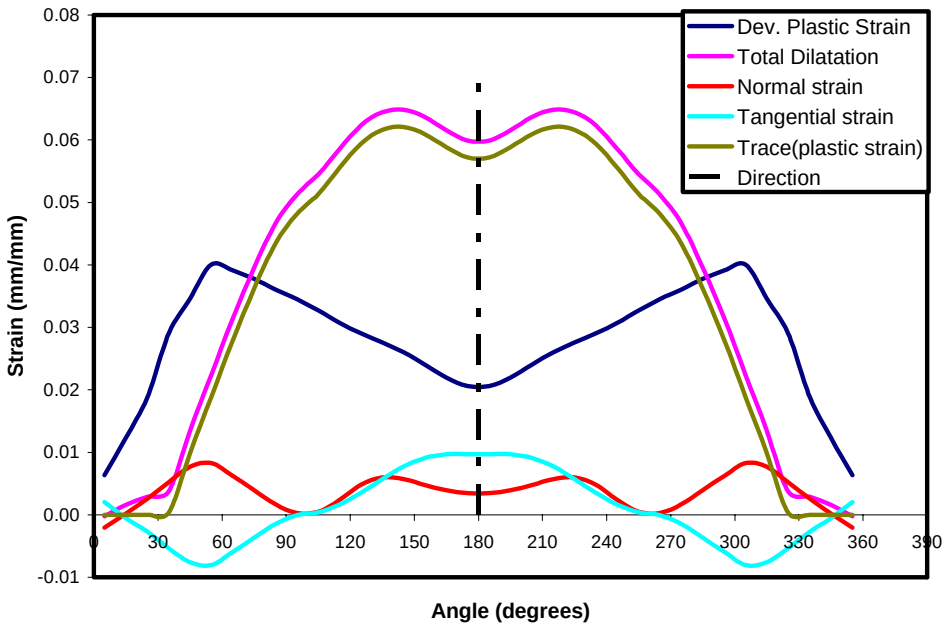

Figure 5.32 Strain fields compared with the known crack advance direction for a mode-I loading edge crack specimen using a J_2 plasticity model in addition to a hydrostatic yield condition with consistency condition enforced.

The mixed-mode simulations were again run with the modified pressure dependence material response to see if one of the parameters found to work for mode-I simulations would also indicate the correct direction for a mixed-mode case. The results are shown in Figures 5.33-5.35. The only stress field that gave the approximate direction is the tangential stress field as seen in Figure 5.33. The tangential strain field also attained a maximum value near the correct direction as indicated in Figure 5.34. The new ratio that worked well in the previous cases is a poor indicatior for direction of advance and is shown along with the rest of the stress ratios in Figure 5.35. The ratio of the tangential strain and von Mises stress did however give a good approximation for direction of advance.

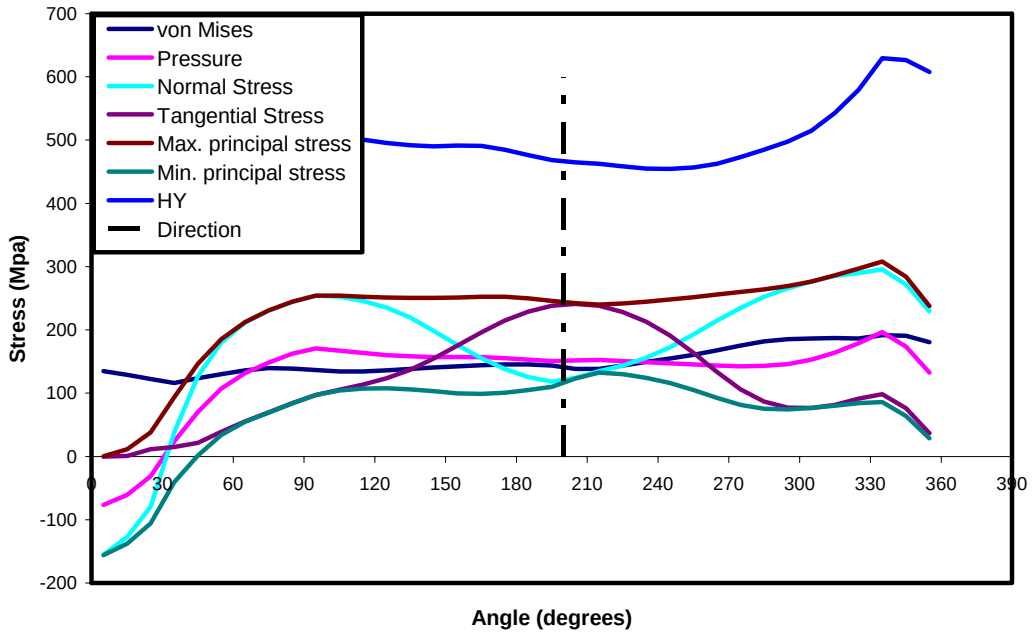

Figure 5.33 Stress fields compared with the known crack advance direction for a mixed-mode loading edge crack specimen using a J_2 plasticity model in addition to a hydrostatic yield condition with consistency condition enforced.

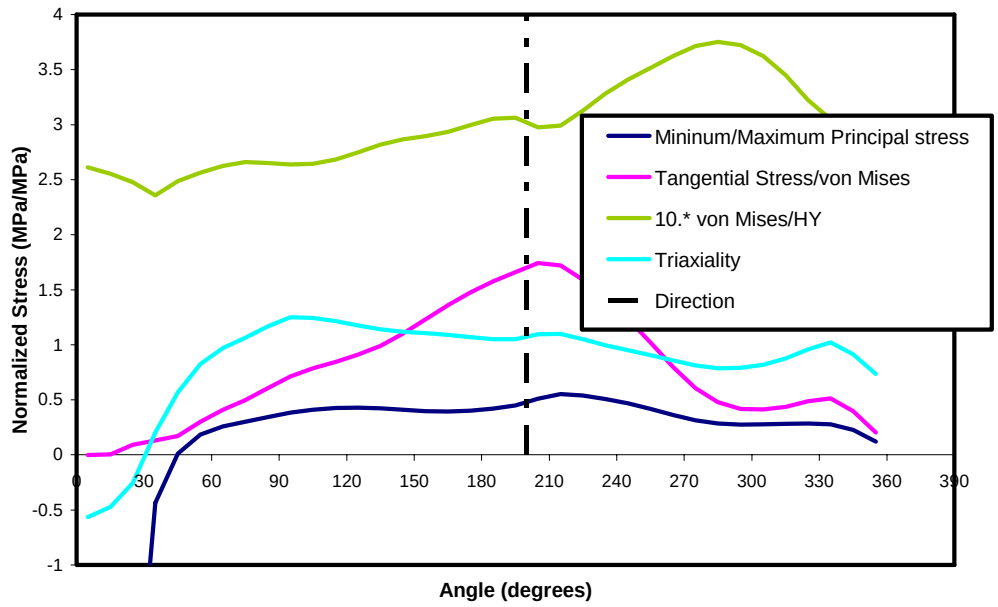

Figure 5.34 Various stress ratios compared with the known crack advance direction for a mixed-mode loading edge crack specimen using a J_2 plasticity model in addition to a hydrostatic yield condition with consistency condition enforced.

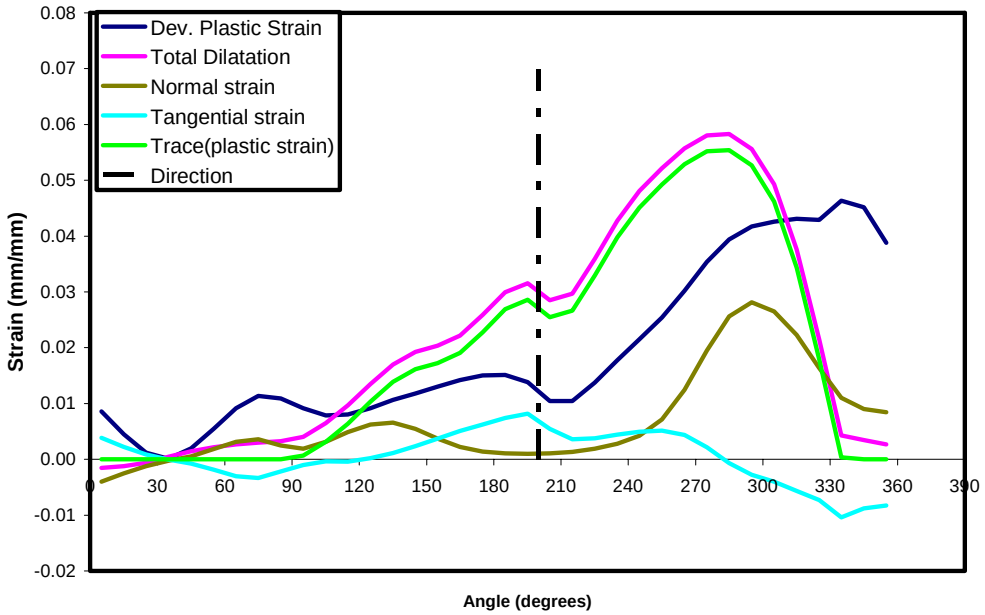

Figure 5.35 Strain fields compared with the known crack advance direction for a mixed-mode loading edge crack specimen using a J_2 plasticity model in addition to a hydrostatic yield condition with consistency condition enforced.

A pressure yield condition that enforced the consistency condition was used to determine if the resulting volumetric strain field could indicate a direction of advance. The volumetric strain from the yield condition in its present form was not able to capture the crack advance angle. The ratio of the von Mises and the hydrostatic yield value also did not show good predictive capabilities within this current context. A power law behavior will be implemented for the softening and hardening terms in the hydrostatic yield condition in hopes that a nonlinear response will allow the resulting volumetric strain to indicate the correct direction of advance.

Concluding remarks

It has been shown that J_2 plasticity alone is not capable of producing one parameter that can drive fracture in varied loading conditions for a non-blunting crack tip. An approach that uses two parameters, plastic strain and normal opening force, has been investigated for and proven to give realistic predictions for crack propagation in mode-I and mixed-mode loading conditions. J_2 plasticity was modified in two ways that incorporated pressure dependence into the yielding condition and investigated their applicability to predict fracture. The linear yield condition did show promise when the consistency condition was not enforced. The future work will incorporate power-law hardening behavior in the hydrostatic yield condition to allow for a highly nonlinear relationship between the yield and the volumetric strain. The yield conditions for the hydrostatic and deviatoric stress components will be coupled instead of decoupled as they are in this study.

CHAPTER VI

SUMMARY AND FUTURE WORK

Summary

A computational framework was presented that is capable of advancing cracks based on damage evolution occurring in ductile material. An error analysis was performed on the exclusion region theory's implementation, and it was shown that stress fields, strain fields, and crack-surface displacements agreed with analytical results for linear elastic material behavior. The elastic-plastic results compared well with a commercial finite element programs results. The exclusion region theory was used to investigate the angular dependence of the stress and strain fields in J_2 plasticity fracture simulations. It was found that only the tangential stress field was capable of predicting the crack advance direction for both a mode-I and a mixed-mode loading scenario. A two parameter damage based crack advance was implemented and showed that exclusion region theory can accommodate crack growth based on damage. Two variants of J_2 plasticity were postulated that incorporated pressure dependence in the constitutive response. Both variants were investigated to see if a single parameter exists that could predict the direction of crack advance based on damage.

Crack-surface displacements were investigated for symmetric cracks emanating from a hole in an infinite plate subjected to a remote uniform stress and a partially loaded crack face. These configurations were chosen because they are common in fatigue simulations for the aerospace industry. Numerical integration was performed and compared to the displacement equations in the literature. It was shown for the case of remote uniform stress, the existing displacement equation was very accurate near the crack tip and had its largest error of approximately ten percent where the crack intersected the hole. A new displacement equation was developed whose maximum error is now one percent. The partially loaded crack surface case revealed the existing displacement equations are accurate as one moves toward the crack tip from the loading position. But, the error increases rapidly between the loading and the crack's intersection with the hole.

Future Work

A variant of J_2 plasticity utilizing a pressure dependent yield condition will be further investigated in hopes of producing a variable that indicates proper crack advance direction and made to include a non-linear evolution for both the softening and hardening terms. It was noted in the last chapter an assumption had to be made for the crack advance direction in a mixed-mode loading scenario. No results could be found in the literature for a mixed-mode monotonic fracture experiment. Research could be conducted to present a standard suite of data to the community that could be used to determine if various ductile fracture methodologies can in fact work for both shear and tension experiments. The new crack surface displacement equation and the numerical

integration method for the partially loaded crack surface will be implemented into a fatigue life prediction program to investigate how the new, more accurate results affect life predictions.

REFERENCES

ABAQUS, Inc. 2008. Abaqus Theory Manual Version 6.8. Providence, Rhode Island, Dassault Systems.

Alciatore, D., and Miranda, R., "A winding number and point-in-polygon algorithm," Glaxo Virtual Anatomy project research report, Department of Mechanical Engineering, Colorado State University, January, 1995.

Anderson, T.L., 2005. *Fracture Mechanics: Fundamentals and Applications*, 3rd ed., CRC Press, Boca Raton, FL, pp. 219-234.

Babuska, I., Banerjee, U., Osborn, J. E., 2003. Survey of meshless and generalized finite element methods: A unified approach, Acta Numerica, Vol. 12, pp.1-126.

Babuska, I., Rheinboldt, W. C., 1978. Error estimates for adaptive finite element computations, SIAM Journal of Numerical Analysis, Vol. 15, pp.736- 754.

Bammann, D.J., 1984. An internal variable model of viscoplasticity, International Journal of Engineering Science, Vol. 22, No. 8-10, pp. 1041-1053.

Bammann, D.J., and Johnson, G.C., 1987. On the kinematics of finite-deformation plasticity, Acta Mechanica, Vol. 70, pp. 1-13.

Bammann, D.J., Aifantis, E.C., 1989. A damage model for ductile metals, Nuclear Engineering and Design, Vol. 116, pp. 355-362.

Bammann, D.J., 1990. Modeling temperature and strain rate dependent large deformations of metals Appl Mech Rev No. 5, Part 2, Eds. Krempl E and McDowell DL, Vol. 43, pp. S312-S319.

Bammann, D.J., Chiesa, M.L. Horstemeyer, M.F., Weingarten, L.I., 1993. Failure in ductile material using finite element methods, *Structural Crashworthiness and Failure* eds. N.Jones and T. Weirzbicki, Elsevier Applied Science, pp. 1-52

Bammann D.J., Chiesa M.L., Johnson G.C., 1996. Modeling large deformation and failure in manufacturing processes, App. Mech., eds, Tatsumi, Wannabe, Kambe. Elsevier Science, pp. 256-276.

Banks-Sills, L., Sherman, D., 1992. On the computation of stress intensity factors for three-dimensional geometries by means of the stiffness derivative and J-integral methods, International Journal of Fracture, Vol. 53 No.1, pp.1-20.

Barrenblatt, G.I., 1962. The mathematical theory of equilibrium cracks in brittle fracture, Advances in Applied Mechanics, Vol. 7, pp. 1743-1757.

Barsoum, R.S., 1976. On the use of isoparametric finite elements in linear fracture mechanics, International Journal for Numerical Methods in Engineering, Vol. 10, pp. 551-564.

Belytschko, T., and Black, T., 1999. Elastic crack growth in finite elements with minimal remeshing, International Journal for Numerical Methods in Engineering, Vol. 45, Number 5, pp. 601-620.

Belytschko, T., Krongauz,Y., Organ, D., Fleming, M., and Krysl, P., 1996. Meshless methods: An overview and recent developments, Computer Methods in Applied Mechanics and Engineering, Vol. 139, Number 1, pp. 3-47.

de Borst, R., Gutierrez, M. A., Wells, G. N., Remmers, J. J. C., and Askes, H., 2004. Cohesive-zone models, higher-order continuum theories and reliability methods for computational failure analysis, International Journal for Numerical Methods in Engineering, Vol. 60, pp. 289-315.

Budiansky, B. and Hutchinson, J. W., 1978. Analysis of Closure in Fatigue Crack Growth, Journal of Applied Mechanics, Vol. 45, pp. 267-276.

Burden, R. L. and Faires, J. D., 1997. Numerical Analysis, 6th ed, Brooks/Cole Publishing Company, Pacific Grove, California, Chapter 4, Section 9.

Chaboche, J.L., 1988a. Continuum damage mechanics: Part I-General concepts, Journal of Applied Mechanics, Vol. 55, pp. 59-64.

Chaboche, J.L., 1988b. Continuum damage mechanics: Part II-Damage growth, crack initiation, and crack growth, Journal of Applied Mechanics, Vol. 55, pp. 65-72.

Chan, S.K., Tuba, I.S., and Wilson, W.K., 1970. On the finite element method in linear elastic fracture mechanics, Engineering Fracture Mechanics, Vol. 2, pp. 1-17.

Chang, C. and Mear, M. E., 1996. A Boundary Element Method for Two-Dimensional Linear Elastic Fracture Analysis, International Journal of Fracture, Vol. 74, pp. 219-251.

Cocks, A.C.F., and Ashby, M.F., 1980. Intergranular fracture during power-law creep under multiaxial stresses, Metal Science, Vol. 14, pp. 395-402.

Cocks, A.C.F., 1989. Inelastic deformation of porous materials, Journal of the Mechanics and Physics of Solids, Vol. 37, No. 6, pp. 693-715.

Conway, J. Functions of One Complex Variable I. Second Edition. Springer-Verlag New York 1978.

Cotterell, B., and Rice, J.R., 1980. Slightly curved or kinked cracks, International Journal of Fracture, Vol. 16, pp. 155-169.

Daux, C., Moes, N., Dolbow, J., Sukumar, N., and Belytschko, T., 2000. Arbitrary cracks and holes with the extended finite element method, International Journal for Numerical Methods in Engineering, Vol. 48, No. 12, pp. 1741-1760.

Davison, L., Stevens, A.L., and Kipp, M.E., 1977. Theory of spall damage accumulation in ductile metals, Journal of the Mechanics and Physics of Solids, Vol. 25, pp. 11-28.

Dieter, George E., 1986. Mechanical Metallurgy, 3rd edition, McGraw-Hill, New York, pp.356-359.

Dill, H. D. and Saff, C. R., 1976. Spectrum Crack Growth Prediction Method based on Crack Surface Displacement and Contact Analyses, ASTM STP 595, pp. 306-319.

Dolbow, J. and Belytschko, T., 1998. An introduction to programming the meshless element free galerkin method, Archives of Computational Methods in Engineering, Vol. 5, Number 3, pp. 207-241.

Dowling, Norman E., 1993. Mechanical Behavior of Materials: Engineering Methods for Deformation, Fracture, and Fatigue, Prentice Hall, p. 309.

Dugdale, D. S., 1960.Yielding of Steel Sheets containing Slits, Journal of the Mechanics and Physics of Solids, Vol. 8, pp. 100-104.

Elices, M., Guinea, G. V., Gomez, J., and Planas, J., 2002. The cohesive zone model: advantages, limitations, and challenges, Engineering Fracture Mechanics, Vol. 69, pp. 137-163.

EnSight 8.2, 2009. CEI International. http://www.ensight.com/ensight.html

Erdogan, F., and Sih, G.C., 1963. On the crack extensions in plates under loading and transverse shear. Transactions of the ASME Series D, Journal of Basic Engineering, Vol. 85, pp. 519-527.

Falk, M.L., Needleman, A., and Rice, J.R., 2001. A critical evaluation of cohesive zone models of dynamic fracture, 5th European Mechanics of Materials Conference, March 5-9, Delft, The Netherlands.

Fish, J., 1992. The s-version of the finite element method, Computers and Structures, Vol. 43, pp.539-547.

Fleming, M., Chu, A., Moran, B., Belytschko, T., 1997. Enriched element-free Galerkin methods for crack tip fields, International Journal for Numerical Methods in Engineering, Vol. 40, pp. 1483-1504.

Fuhring, H. and Seeger, T., 1979. Dugdale Crack Closure Analysis of Fatigue Cracks under Constant Amplitude Loading, Engineering Fracture Mechanics, Vol. 11, pp. 99-122.

Garrison, W. M. Jr., Moody, N. R., 1987. Ductile fracture, J. of Physics and Chem. of Solids, Vol. 48, n 11, pp. 1035-1074.

Giner, E., Sukumar, N., Tarancón, J.E., and Fuenmayor, F.J., 2009. An Abaqus implementation of the extended finite element method, Engineering Fracture Mechanics, Vol. 76, No. 3, pp. 347–368.

Goijaerts, A.M., Govaert, L.E., and Baaijens, F.P.T., 2001. Evaluation of ductile fracture models for different metals in blanking. Journal of Material Processing Technology, Vol. 110, pp. 312-323.

Griffith, A.A., 1920. "The phenomena of rupture and flow in solids," Philosophical Transactions, Series A, Vol. 221, pp.163-198.

Gullett, P. M., Horstemeyer, M.F., Waters, A.M., and Frazier, K.F, 2005. Simulated void growth and failure in AM60B magnesium tension specimens, VIII International Conference on Computational Plasticity, COMPLAS VIII, Eds. E. Onate and D.R.J. Owen, CIMNE, Barcelona.

Gurson, A.L., 1977. Continuum theory of ductile rupture by void nucleation and growth: Part 1—yield criteria and flow rules for porous ductile media, Journal of Engineering Materials and Technology, Vol. 99, pp. 2-15.

Haber, R.B., and Koh, H.M.,1985. Explicit expressions for energy release rates using virtual crack extensions. International Journal of Numerical Methods in Engineering, Vol. 21, pp. 301-315.

Hahn G.T., and Rosenfield A.R., 1975. Metallurgical factors affecting fracture toughness of aluminum alloys. Metall. Trans. A, Vol. 6a, pp. 653-70.

Hellen, T.K., 1975. On the method of virtual crack extension. Computational Methods in Applied Mechanical Engineering, Vol. 12, pp. 353–364.

Henshell, R.D., and Shaw, K.G., 1975. Crack tip finite elements are unnecessary, International Journal of Numerical Methods in Engineering, Vol. 9, pp.495-507.

Hildebrand, G., 2009. Fracture analysis using an enriched meshless method, Meccanica, pp. 1-11.

Hom, C.L., and McMeeking, R.M., 1989. Three-dimensional void growth before a blunting crack tip, Journal of the Mechanics and Physics of Solids, Vol. 37, No. 3, pp. 395-415.

Horstemeyer. M.F., Gokhale, A.M., 1999. A void-crack nucleation model for ductile metals, Int. J. Solids and Structures, Vol. 36, pp. 5029-5055

Horstemeyer, M.F., Lathrop. J., Gokhale. A.M., Dighe, M., 2000. Modeling stress state dependent damage evolution in a cast Al-Si-Mg aluminum alloy Theor and Appl Fract Mech, Vol. 33, pp. 31-47.

Horstemeyer. M.F., 2001. From atoms to autos: a new design paradigm using microstructure-property modeling Part 1: Monotonic loading conditions, Sandia National Lab, 6.6-11.

Hutchinson, J.W., 1968. Singular behavior at the end of a tensile crack tip in a hardening material, Journal of the Mechanics and Physics of Solids, Vol. 16, pp.13-31.

Idelsohn, S., Onate, E., Calco, N., and Del Pin, F., 2002. Meshless finite element ideas, WCCMV FifthWorld Congress on Computational Mechanics, July 7-12, Vienna, Austria.

Inglis, C.E., 1913. Stresses in a plate due to the presence of crack sand sharp corners, Transactions of the Institute of Naval Architects, Vol. 55, pp. 219-241.

Irwin, G.R. 1948. Fracture Dynamics, Fracturing of Metals, ASM Intenational, Metals Park, OH, pp.147-166.

Irwin, G.R., 1957. Analysis of stresses and strains near the end of a crack traversing a plate, Journal of Applied Mechanics, Vol. 24, pp. 361-364.

Irwin, G.R., 1958. Fracture I, Handbuch der Physik VI, Flugge (Ed.), Springer, pp. 558-590.

Irwin, G.R., 1961. Plastic zone near a crack and fracture toughness, Sagamore Research Conference Proceedings, Vol. 4, pp. 63-78.

James, M.A., Newman, J.C., Jr., 2002. Three-dimensional analysis of crack-tip-opening angles and δ_5-resistance curves for 2024-T351 aluminum alloy, ASTM STP 1406, pp. 279-297.

Kachanov, L.M., 1958. Time of the rupture process under creep conditions, Isv. Akad. Nauk., SSR., Otd Tekh. Naul., Vol. 8, pp. 26-31.

Lee, N.S., and Bathe, K.J., 1994. Error indicators and adaptive remeshing in large deformation finite element analysis, Finite Elements in Analysis and Design, Vol. 16, pp. 99-139.

Li, F.Z., Shih, C.F., and Needleman, A., 1985. A comparison of methods for calculating energy release rates, Engineering Fracture Mechanics, Vol. 21, pp.405-421.

Li, Shaofan and Liu, Wing Kam, 2004. Meshfree Particle Methods, Springer.

Liu, G.R., 2002. Mesh Free Methods: Moving beyond the Finite Element Method, CRC Press.

Liu, W. K., Hao, S., Belytschko, T., Li, S., and Chang, C. T., 1999. Multiple scale meshfree methods for damage fracture and localization, Computational Materials Science, Vol. 16, pp. 197-205.

Liu, W. K., Hao, S., Chang, C. T., 2000. Computer implementation of damage models by finite element and meshfree methods, Computer methods in applied mechanics and engineering, Vol. 187, pp. 401-440.

Love, A.E.H. "A treatise on the mathematical theory of elasticity", Cambridge University Press, 1927.

Moes, N., Dolbow, J., and Belytschko, T., 1999. A finite element method for crack growth without remeshing, International Journal for Numerical Methods in Engineering, Vol. 46, No. 1, pp. 131-150.

Mall, S. and Newman, J. C., Jr., 1985. The Dugdale Model for Compact Specimen, ASTM STP 868, pp. 113-128.

Mediavilla, J., Peerlings, R.H.J., and Geers, M.G.D., 2006a. A robust and consist remeshing-transfer operator for ductile fracture simulations, Computers and Structures, Vol. 84, pp. 604-623.

Mediavilla, J., Peerlings, R.H.J., and Geers, M.G.D., 2006b. Discrete crack modeling of ductile fracture driven by non-local softening plasticity, International Journal for Numerical Methods in Engineering, Vol. 66, pp. 661-688.

McClintock, F.A., 1968. A criterion for ductile fracture by the growth of holes, Journal of Applied Mechanics, Vol. 35, pp. 363-371.

Nemat-Nasser, S., and Taya, M., 1980. Numerical studies of void growth in a necked bar, International Journal of Solids and Structures, Vol. 16, No. 6, pp. 483-494.

Newman, J. C., Jr., 1971. An improved method of collocation for the stress analysis of cracked plates with various shaped boundaries, NASA TN D-6376.

Newman, J. C., Jr., 1981. A crack closure model for predicting fatigue crack growth under aircraft spectrum loading, ASTM STP 748, pp. 53-84.

Newman, J. C., Jr., 1983. A nonlinear fracture mechanics approach to the growth of small cracks, AGARD Conference Proceedings No. 328, pp. 6.1-6.26.

Newman, J.C., Jr., 1984. An elastic-plastic finite element analysis of crack initiation, stable crack growth, and instability, ASTM STP 833, pp.93-117.

Newman, J.C., Jr., James, M.A., and Zerbst, U., 2003. A review of the CTOA/CTOD fracture criterion, Engineering Fracture Mechanics, Vol. 70, pp. 371-385.

Oden, J. T., Demkowicz, L. F., Rachowicz, W., and Westermann, T., 1989. Toward a universal h-p adaptive finite element strategy, part 2. a posteriori error estimation, Computer Methods In Applied Mechanics and Engineering, Vol. 77, pp.113-180.

Orowan, E., 1955. Energy of fracture, Welding Journal, Research Supplement, Vol. 34, Number 3, pp.157s-160s.

ParaView, Kitware, Inc., 2009. http://www.paraview.org.

Parks, D.M., 1974. A stiffness derivative finite element technique for determination of crack tip stress intensity factors, International Journal of Fracture, Vol. 10, pp. 487-502.

Pirondi, A., and Dalle Donne, C., 2001. Characterisation of ductile mixed-mode fracture with the crack-tip displacement vector, Engineering Fracture Mechanics, Vol. 68, pp. 1385-1402.

Rabotnov, Y.N., 1969. Creep problem in structural members, North-Holland.

Rao, B. N., and Rahman, S., 2000. An efficient meshless method for fracture analysis of Cracks, Computational Mechanics, Vol. 26, pp. 398-408.

Rashid, M. M., 1993. Incremental kinematics for finite element applications, International Journal for Numerical Methods in Engineering, Vol. 36, pp. 3937-3956.

Rashid, M. M., 1997a. A new theory for free-surface formation in solid continua, International Journal of Solids and Structures, Vol. 34, pp. 2303-2320.

Rashid, M. M., 1997b. A computational procedure for simulation of crack advance in arbitrary two-dimensional domains, Computational Mechanics, Vol. 20, pp. 133-138.

Rashid, M. M., 1998. The arbitrary local mesh replacement method: an alternative to remeshing for crack propagation analysis, Computer Methods in Applied Mechanics and Engineering, Vol. 154, pp. 133-150.

Rashid, M. M. and Roy, Ritwick, 1999. A new theoretical framework for inelastic fracture processes, Fatigue and Fracture Mechanics: Twenty-Ninth Volume, ASTM STP 1332, T.L. Panontin and S.D. Sheppard, Eds., American Society for Testing and Materials, West Conshohocken, PA.

Rashid, M. M. and Tvergaard, V., 2003. On the path of a crack near a graded interface under large scale yielding, International Journal of Solids and Structures, Vol. 40, pp. 2819-2831.

Rashid, M. M. and Tvergaard, V., 2008. Crack trajectory near a weld: Modeling and simulation, Engineering Fracture Mechanics, Vol. 75, pp. 560-570.

Rice, J.R. 1968. A path independent integral and the approximate analysis of strain concentration by notches and cracks, Journal of Applied Mechanis, Vol. 35, pp.379-386.

Rice, J.R., and Rosengren, G.F., 1968. Plane strain deformation near a crack tip in a power-law hardening material, Journal of the Mechanics and Physics of Solids, Vol. 16, pp.1-12.

Rice, J.R., and Tracey, D.M., 1969. On the ductile enlargement of voids in triaxial stress fields, Journal of the Mechanics and Physics of Solids, Vol. 17, pp. 201-217.

Rice, J.R., Drugan, W.J., and Sham, T.-L., 1980. Elastic-plastic analysis of growing cracks, ASTM STP 700, American Society for Testing and Materials, Philadelphia, PA, pp.189-221.

Rots, J.G., 1991. Smeared and discrete representations of localized fracture, International Journal of Fracture, Vol. 51, pp. 45-59.

Saint Venant, A.J.C.B., 1855, Memoire sur la Torsion des prismes, Mem. Divers Savants, Vol. 14, pp. 233-560.

Schellekens, JCJ, de Borst, R, 1992. On the numerical integration of interface elements, International Journal for Numerical Methods in Engineering, Vol. 36, pp. 43-66.

Shih, C.F., de Lorenzi, H.G., Andrews, W.R., 1979. Studies on crack initiation and stable crack growth, ASTM STP 668, American Society for Testing and Materials, Philadelphia, PA, pp.65-120.

Shivakumar, V. and Forman, R. G., 1980. Green's Function for a Crack Emanating from a Circular Hole in an Infinite Sheet, International Journal of Fracture, Vol. 16, pp. 305-316.

Sneddon, I.N., 1946. The distribution of stress in the neighbourhood of a crack in an elastic solid, Proceedings, Royal Society of London, Vol. A-187, pp. 229-260.

Sun, C.T., and Jin, Z.-H, 2006. A comparison of cohesive zone modeling and classical fracture mechanics based on near tip stress field, International Journal of Solids and Structures, Vol. 43, pp. 1047-1060.

Tada, H., Paris, P. C. and Irwin, G. R., 2000. The Stress Analysis of Cracks Handbook, Third Edition, American Society of Mechanical Engineers, New York, NY.

Tvergaard, V., 1982. On localization in ductile materials containing spherical voids, International Journal of Fracture, Vol. 18, pp. 237-252.

Tvergaard, V., 1990. Material failure by void growth to coalescence, Advances in Applied Mechanics, Vol. 27, pp. 83-151.

Tvergaard, V., and Needleman, A., 2001. The modified Gurson model, Handbook of Materials Behavior Models, Jean Lemaitre ed., pp.430-435.

Waters, A.M., Martz, H.E., Dolan, K.W., Horstemeyer, M.F., and Green, R.E., 2000. Three dimensional void analysis of AM60B magnesium alloy tensile bars using computed tomography imagery, Materials Evaluation, Vol. 58, pp. 1221-1227.

Wells, A.A., 1961. Unstable crack propagation in metals: cleavage and fast fracture, Proceedings of the Crack Propagation Symposium, Vol. 1, Paper 84, Cranfield, UK.

Westergaard, H.M., 1939. Bearing pressures and cracks, Journal of Applied Mechanics, Vol. 6, pp.49-53.

Williams, M.L., 1957. On the stress distribution at the base of a stationary crack, Journal of Applied Mechanics, Vol. 24, pp. 109-114.

Williamson, R.L., Wright, J.K., Steffler, E.D., and Cannon, R.M., 2003. Numerical analysis of surface cracks at regions of curvature in oxide scales, Materials Science and Engineering A, Vol. 342, pp. 109-119.

Xia, L., and Shih, C.F., 1995. Ductile crack growth-I. A numerical study using computational cells with microstructurally-based length scales. Journal of the Mechanics and Physics of Solids, Vol. 43, No. 2, pp. 233-259.

Xu, X.P., Needleman, A., 1994. Numerical simulations of fast crack growth in brittle solids, Journal of the Mechanics and Physics of Solids, Vol. 42, pp. 1397-1434.

Zeinkiewicz, O.C., Zhu, J.Z., 1987. A simple error estimator and adaptive procedure for practical engineering analysis, International Journal for Numerical Methods in Engineering, Vol. 24, pp. 337-357.